UNIVERSITY OF SOUTHAMPTON

FACULTY OF ENGINEERING AND THE ENVIRONMENT

Materials and Surface Engineering

Micromechanism Characterisation of Fatigue in Carbon Fibre Reinforced Polymers using Synchrotron X-ray Computed Tomography

by

Serafina Consuelo Garcea

Thesis submitted for the degree of Doctor of Philosophy

April 2015

Supervisors:

Professor S. Mark Spearing
Professor Ian Sinclair

Materials and Surface Engineering Group
Faculty of Engineering and the Environment

UNIVERSITY OF SOUTHAMPTON

ABSTRACT

FACULTY OF ENGINEERING AND THE ENVIRONMENT

Doctor of Philosophy

MICROMECHANISM CHARACTERISATION OF FATIGUE IN CARBON FIBRE REINFORCED POLYMERS USING SYNCHROTRON X-RAY COMPUTED TOMOGRAPHY

by Serafina Consuelo Garcea

The micromechanical characterisation of fatigue damage initiation and propagation has been assessed in carbon fibre reinforced polymer systems using synchrotron radiation computed tomography. Three material systems were used: a particle-toughened system, an untoughened system, and an intrinsically toughened system, all with a cross-ply layup. Fatigue damage initiation and propagation have been investigated by *in situ* fatigue tests and the results correlated with the local microstructure, highlighting the key mechanisms contributing to enhance damage resistance in the toughened systems. Particular attention was focused on the study and characterisation of 0˚ ply splits, which nucleate from the notch and propagate parallel to the loading direction. Damage does not initiate and propagate as a dominant crack, but in the form of multiple discontinuous crack segments separated by bridging ligaments. This micromechanism is common to all the material systems investigated, albeit with significant differences in the lengthscale. The untoughened system is characterised by the formation of small bridging ligaments at the fibre/matrix interface (on the order of a few micrometers) and exhibits a more uniform crack profile growth, as the damage progression degrades bridging, creating a more continuous crack. In contrast, in the toughened systems, particularly the particle-toughened system, the bridging ligaments detected are related to the presence of

resin rich regions and/or particles, resulting in larger ligaments (~50 μm) than the untoughened system. This has a direct influence on the crack front profile that is jagged, indicating a non-uniform crack growth across the ply thickness for the toughened systems. Damage has been quantified in terms of crack opening and crack shear displacement. The influence of the peak load, number of cycles, crack length, local microstructure and interaction of damage modes on the crack opening displacement has been investigated. The results showed different crack opening behaviour depending on the crack length: 0˚ ply splits within the notch region are dominated by the notch stress/strain field, whereas longer cracks exhibit a steady-state behaviour with a constant crack opening for the majority of the crack length. Crack growth rates were observed to be very similar between the three materials investigated. Fibre failure under fatigue loading was evaluated for different peak loads and numbers of cycles. Fibre breaks along the 0˚ ply splits and in the bulk composite have been detected and classified.

The comparison with equivalent quasi-static cases highlighted similarities in terms of damage initiation and propagation. However, fatigue loading is defined by a degradation of the bridging ligaments, and consequently less effectiveness of the toughened systems in fatigue than under tensile loading. A direct comparison with the quasi-static case, using the same material system and geometry, has shown that the number of fibre breaks is lower than that observed for the equivalent load peak in the fatigue cases. This confirms that the fibre breaks detected in the fatigue cases are not associated with the initial loading cycles (tensile), but are indeed caused by the cycling process.

This research provides insights into the fundamental micromechanisms of fatigue as well as guidance for improving material performance for damage resistance and damage tolerance using for the first time synchrotron radiation computed tomography to assess fatigue micromechanisms in carbon fibre reinforced polymers.

DECLARATION OF AUTHORSHIP

I, Serafina Consuelo Garcea, declare that this thesis and the work presented in it are my own and have been generated by me as the result of my own original research.

Micromechanism Characterisation of Fatigue in Carbon Fibre Reinforced Polymers using Synchrotron X-ray Computed Tomography

I confirm that:

- This work was done wholly or mainly while in candidature for a research degree at this University;
- Where any part of this thesis has previously been submitted for a degree or any other qualification at this University or any other institution, this has been clearly stated;
- Where I have consulted the published work of others, this is always clearly attributed;
- Where I have quoted from the work of others, the source is always given. With the exception of such quotations, this thesis is entirely my own work;
- I have acknowledged all main sources of help;
- Where the thesis is based on work done by myself jointly with others, I have made clear exactly what was done by others and what I have contributed myself;
- Parts of this work have been published as indicated in the list of publications section provided in this manuscript.

Signed:

Date:

Acknowledgements

The work contained in this thesis represents the result of the contributions from the Composites Group at University of Southampton. Immeasurable thanks must be given to my supervisors, Professor Mark Spearing and Professor Ian Sinclair, for their profound knowledge and experience of the field. Their guidance, assistance and support through these years of my PhD were invaluable.

Thanks to the μ-VIS at the University of Southampton for the computer analysis facilities and their assistance, particularly to Dr. Mark Mavrogordato for his effort with the setup of the *in situ* fatigue device, and his constant presence during the synchrotron sessions. I am grateful to the Swiss Light Synchrotron Radiation for access to TOMCAT-X02DA beamline, and to the assistance of Dr. Bernd Pinzer, Dr. Sarah Irvine, and Dr. Peter Modregger, throughout the different sessions.

I would like to acknowledge funding from AFOSR-EOARD, grant 113040, Programme Monitor: Lt. Col. Randall Pollak. Also funding from EPSRC, grant EP/H1506X/1. Composite materials were supplied via Airbus SAS and Teledyne Technologies Incorporated.

Last but not least a special thanks to all my friends, that with their smiles made my PhD life much more enjoyable. Thanks to my colleagues, Gregor, Dan, and Trevor for the good discussions and the time spent together between synchrotron sessions and conferences, in the 'Composites Word'.

Table of Contents

Chapter 1

Introduction

1.1 Background and motivation

Carbon fibre reinforced polymers (CFRPs) are well established as an important weight-reducing structural technology, particularly within the aerospace sector due to their high specific stiffness and strength [1,2]. Whilst CFRPs are widely identified as being very fatigue resistant, typically this advantage is not fully exploited in design. As such, understanding and predicting the durability of these materials is of great interest. Previous studies have focused on assessing fatigue damage mechanisms and the link to fatigue life using various experimental techniques [3-9]. However, reliable predictions based on physical observations remain key to improving CFRP structural design. Improving the fracture toughness of thermosetting resins has been the focus of numerous studies, which have explored a range of solutions such as the introduction of rubber particles [10-12], thermoplastic particles [13-15], or high stiffness filler particles [16,17]. Conversely, the introduction of such particles may result in a reduction in elastic modulus, tensile strength, stability at high temperature and glass transition temperature [18-20]. To date, several approaches of toughening have been developed to a sufficient level of maturity that they are employed in service for CFRPs for aerospace applications; however, the underpinning micromechanisms have not been widely investigated. Consequently, the effectiveness and optimization of specific toughening systems in terms of damage reduction and fracture toughness remains a relatively empirical process. Furthermore, there has been very little work to

understand the consequence of fatigue loading on the effectiveness of these toughening strategies.

Previous studies have been conducted on carbon fibre/epoxy laminated composites using X-ray computed tomography, demonstrating the power of this technique in assessing damage micromechanisms for small coupons subjected to quasi-static load [21-23], impact [24,25], and compression after impact [26]. The detail and the accuracy provided using a resolution on the order of 1 μm has been shown to be appropriate to capture both primary damage events (such as ply cracking), along with key local events such as decohesion of toughening particles or fibres, facilitating correlation with primary microstructural features such as the ply structure and the presence of resin-rich and fibre-rich regions [21,23].

The current work has the aim of delineating for the first time the micromechanisms of fatigue damage in carbon fibre-epoxy laminated composites using *in situ* and *ex situ* synchrotron radiation computed tomography (SRCT). The evaluation of damage and its interaction with toughening particles in this case is not limited to the surfaces (free surfaces, or *post mortem* failure surfaces), and is distinctively not affected by sectioning artefacts from cutting, polishing and so forth. The ability to explore three-dimensional volumes is of fundamental importance in multidirectional laminates that exhibit multiple damage mechanisms, as in this work. Performing *in situ* experiments is relevant to follow damage propagation, capturing the chronology of micro-mechanistic interactions. This project has four main objectives: first to conduct an investigation of the mechanisms that underpin fatigue behaviour across a range of composite systems employing different toughening strategies. At this stage two-and three-dimensional damage images reveal similarities and differences associated with toughened and untoughened systems. The second element is to evaluate the micromechanisms of fatigue damage initiation in a particle-toughening system, assessing the role of toughening particles at the early stage of fatigue life. The third element is the evaluation of fibre failure under fatigue loading in the particle-toughened system with a direct comparison with the tensile case for the same material system. The fourth element is represented by the quantification of damage in the particle-toughened system with the aim of informing subsequent modelling.

1.2 Thesis structure

This report contains a detailed description of the results presented in the two published journal papers together with two additional chapters of unpublished results (in preparation for publication in archival journals). The structure of the thesis is as follows: the first part of Chapter 2 describes the state of the art of fatigue in composites, focusing particularly on the toughening strategies followed to date; while the second part of the Chapter 2 provides an overview of the methodology used for synchrotron radiation computed tomography. Chapter 3 focuses on the material systems and computed tomography procedure used in this study. The methodologies implemented to perform the image analyses using the various software packages and the approaches used to quantify the crack opening and crack shear displacement are explained. Chapter 4 presents the micromechanical characterisation of the particle-toughened system with the aim of evaluating the dependence of damage initiation and propagation from the microstructure, mainly due to the presence of particles. The comparison with the quasi-static case for the same material system is provided. Chapter 5 shows the first use of *in situ* high-resolution computed tomography to assess fatigue micromechanisms in toughened and untoughened CFRP systems. The different behaviour of damage propagation and dependence on the microstructure and the consequent crack profile shape are described for the three material systems presented. An interesting observation is represented by the fibre fractures detected during *in situ* tests. This latter aspect is further investigated in Chapter 6, including a different range of peak loads and numbers of cycles for the particle-toughened system by *ex situ* experiments. Chapter 7 provides the quantification of crack opening and crack shear displacement for different loading conditions. The comparison with the results in the literature for an equivalent quasi-static case is reported. Chapter 8 contains the conclusions of this research, and highlights topics for future study based on the open questions associated with the present results obtained.

1.3 Significant contributions

This study has made the following original contributions to the field of composite damage:

- First use of synchrotron radiation computed tomography to investigate the micromechanisms of fatigue in fibre composite materials, identifying 3D crack behaviour down to ~300 nm resolutions.
- First comparison of micromechanisms of fatigue between toughened and untoughened systems.
- First identification of the role of bridging ligaments in generating damage resistance (toughness) investigated via quantitative mapping of local crack opening displacements.
- First identification of the effect of fatigue on failure of crack bridging ligaments.
- First quantification of the effect of fatigue on fibre failure, particularly identifying systematic differences between toughened and untoughened systems.
- First quantification of the influence of the peak loads, number of cycles, cracks length, and damage modes interaction on the crack opening and crack shear displacement.

1.4 List of publications

This work has been disseminated through the following publications and conference presentations.

1.4.1 Journal papers

- S.C. Garcea, M.N. Mavrogordato, A.E. Scott, I. Sinclair, S.M. Spearing, “Fatigue micromechanism characterisation in carbon fibre reinforced polymers using synchrotron radiation computed tomography”, *Composites Science and Technology*, Vol. 99, pp. 23-30, 2014.

- S.C. Garcea, I. Sinclair, S.M. Spearing, "*In situ* synchrotron tomographic evaluation of the effect of toughening strategies on fatigue micromechanisms in carbon fibre reinforced polymers", *Composites Science and Technology*, Vol. 109, pp.32-39, 2015.
- S.C. Garcea, I. Sinclair, S.M. Spearing, "Investigation of fatigue damage initiation in carbon fibre reinforced polymers using synchrotron radiation computed tomography". In preparation.
- S.C. Garcea, I. Sinclair, S.M. Spearing, "Fibre failure investigation on carbon fibre reinforced polymers during fatigue loading using synchrotron radiation computed tomography". In preparation.
- S.C. Garcea, I. Sinclair, S.M. Spearing, "The effect of load cycling on material degradation on carbon fibre reinforced polymers synchrotron radiation computed tomography". In preparation.

1.4.2 Conference papers

- S.C. Garcea, M.N. Mavrogordato, A.E. Scott, I. Sinclair, S.M. Spearing, "Synchrotron computed tomography of fatigue micromechanisms in CFRP", *Proceedings of 19th International Conference on Composite Materials*, Montreal, 2013.
- S.C. Garcea, I. Sinclair, S.M. Spearing, "Characterisation of fatigue micromechanisms in toughened carbon fiber-polymer composites using synchrotron radiation computed tomography", *Proceedings of the 16th European Conference on Composite Materials*, Seville, 2014.
- S.C. Garcea, I. Sinclair, S.M. Spearing, "Assessment of fatigue damage initiation and progression in CFRP using synchrotron radiation computed tomography", *Proceedings of the 6th International Conference on Fatigue of Composites*, Paris, 2015.

1.5 References

[1] D.Hull and T.W. Clyne, *An introduction to composite materials*, Second edition ed.,

Cambridge Solid State Science Series, Ed.: Cambridge University Press.

[2] Bryan Harris, Ed., *Fatigue in Composites*.: CRC Press, 2003.

[3] S.M. Spearing and P.W. Beaumont, "Fatigue damage mechanics of composite materials. I: Experimental measurement of damage and post-fatigue properties," *Composites Science and Technology*, vol. 44, pp. 159-168, 1992.

[4] C. Koimtzoglou, V. Kostopoulos, and C. Galiotis, "Micromechanics of reinforcement and damage initiation in carbon fibre/epoxy composites under fatigue loading," *Composites Part A: Applied Science and Manufacturing*, vol. 32, no. 3-4, pp. 457-471, 2001.

[5] J.R. Gregory and S.M. Spearing, "Constituent and composite quasi-static and fatigue fracture experiments," *Composites Part A: Applied Science and Manufacturing*, vol. 36, no. 5, pp. 665-674, 2005.

[6] O.J. Nixon-Pearson, S.R. Hallet, P.J. Withers, and J. Rouse, "Damage development in open-hole composite specimens in fatigue. Part 1: experimental investigation," *Composites Structures*, vol. 106, pp. 882-889, 2013.

[7] S.M. Spearing, P.W. Beaumont, and M.F. Ashby, "Fatigue damage mechanics of composite materials. II: a damage growth model," *Composites Science and Technology*, vol. 44, no. 2, pp. 169-177, 1992.

[8] O.J. Nixon-Pearson, S.R. Hallett, P.W. Harper, and L.F. Kawashita, "Damage development in open-hole composite speciemens in fatigue. Part 2: Numerical modelling," *Composite Structure*, vol. 106, pp. 890-898, 2013.

[9] Y.A. Dzenis, "Cycle-based analysis of damage and failure in advanced composite under fatigue 1. Experimental observation of damage development within loading cycles," *InternationalJournal of Fatigue*, vol. 25, no. 6, pp. 499-510, 2003.

[10] R.A. Pearson and A.F. Yee, "Influence of particle size distribution on toughening mechanisms in rubber-modified epoxies," *Journal of Materials Science*, vol. 26, pp. 3828-3844, 1991.

[11] L. Becu, A. Maazouz, H. Sautereau, and J.F. Gerard, "Fracture behavior of epoxy polymers modified with core-shell rubber particles," *Journal of Applied Polymer Science*, vol. 65, pp. 2419-2431, 1997.

[12] H.R. Azimi, R.A. Pearson, and R.W. Hertzberg, "Fatigue of rubber-modified epoxies: effect of particle size and volume fraction," *Journal of Materials Science*, vol. 31, pp. 3777-3789, 1996.

[13] R.A. Pearson and A.Y. Yee, "Toughening mechanisms in thermoplastic-modified epoxies: 1. Modification using poly (phenylene oxide)," *Polymer*, vol. 34, no. 17, pp. 3658-3670, 1993.

[14] J.H. Hodgkin, G.P. Simon, and R.J. Varley, "Thermoplastic toughening of epoxy resins: a critical review," vol. 9, pp. 3-10, 1998.

[15] A.J. Kinloch, M.L. Yuen, and S.D. Jekins, "Thermoplastic-toughened epoxy polymers," *Journal of Materials Science*, vol. 29, pp. 3781-3790, 1994.

[16] J. Spanoudakis and R.J. Young, "Crack propagation in a glass particle-filled epoxy resin, Part 1 Effect of particle volume fraction and size," *Journal of Materials Science*, vol. 19, pp. 473-486, 1984.

[17] J. Spanoudakis and R.J. Young, "Crack propagation in a glass particle-filled epoxy resin, Part 2 Effect of particle-matrix adhesion," *Journal of Materials Science*, vol. 19, pp. 487-496, 1984.

[18] A.C. Garg and Y-W Mai, "Failure mechanisms in toughened epoxy resins - a review," *Composites Science and Technology*, vol. 31, pp. 179-223, 1988.

[19] R.P. Singh, M. Zhang, and D. Chan, "Toughening of a brittle thermosetting polymer: effect of reinforcement particle size and volume fraction," *Journal of Materials Science*, vol. 37, pp. 781-788, 2002.

[20] B.U. Kang et al., "Effect of molecular weight between crosslink on the fracture behaviour of rubber-toughened epoxy adhesives," *Journal of Applied Polymer Science*, vol. 79, pp. 38-48, 2001.

[21] A.J. Moffat, P. Wright, J-Y. Buffiere, I. Sinclair, and S.M. Spearing, "Micromechanics of damage in 0 splits in a [90/0]s composite material using synchrotron radiation computed tomography," *Scripta Materialia*, vol. 59, pp. 1043-1046, 2008.

[22] P. Wright, A. Moffat, I. Sinclair, and S.M. Spearing, "High resolution tomographic imaging and modelling of notch tip damage in a laminated composite," *Composites Science and Technologies*, vol. 70, pp. 1444-1452, 2010.

[23] A.E. Scott, M. Mavrogordato, P. Wright, I. Sinclair, and S.M. Spearing, "In situ fibre fracture measurement in carbon-epoxy laminates using high resolution computed tomography," *Composites Science and Technologies*, vol. 71, pp. 1471-1477, 2011.

[24] D.J. Bull, L. Helfen, I. Sinclair, S.M. Spearing, and T. Baumbach, "A comparioson of multi-scale 3D X-ray tomographic inspection techniques for assessing carbon fibre composite impacy damage," *Composites Science and Technologies*, vol. 75, pp. 55-

61, 2013.

[25] D.J. Bull, S.M. Spearing, I. Sinclair, and L. Helfen, "Three-dimensional assessment of low velocity impact damage in particle toughened composite laminates using micro-focus X-ray computed tomography and synchrotron radiation laminography," *Composites: Part A*, vol. 52, pp. 62-69, 2013.

[26] D.J. Bull, S.M. Spearing, and I. Sinclair, "Quasi-static indentation and compression after impact damage growth monitoring using microfocus X-ray computed tomography," in *The 19th International Conference on Composite Materials*, Montreal, 2013.

Chapter 2

Literature review

This chapter describes the state of the art on fatigue in composites, toughening strategies, and connected micromechanisms providing the relevant work present in the literature. The second part of the chapter describes the physics of X-rays and the principle of computed tomography. The approach follows in this second part is deliberately non-mathematical, but mostly intuitive and qualitative.

2.1 Introduction

It is well known that unidirectional carbon fibre reinforced polymers have excellent fatigue resistance in the fibre direction. This derives from the fact that the fibres, which are essentially fatigue resistant, mainly carry the load. Therefore, unidirectional CFRP exhibit good properties in terms of axial fatigue resistance [1,2]. However, composites are widely used as laminates in engineering design, and damage is seen to initiate in corresponding real structures at low numbers of cycles. Damage modes and their interactions are affected by the nature of a composite (i.e. combinations of fibre/matrix, lay-up, geometry) and load condition. The experimental scatter of data, associated with the statistical nature and variable quality of commercial composites, complicates the analysis. In this context it is difficult to relate the damage accumulation to the residual properties of the material; predicting fatigue life.

The study of notched coupons has gained interest in the last decades [3-6]. The presence of the notch introduces additional variables in the study, such as the presence of stress concentration, the notch sensitivity [4], and the final quality of the cutting or drilling when the notch is created. Previous study conducted on fatigue (tension-tension) has shown that the presence of 0˚ ply split (directly connected to the presence of the notch) contributes to the redistribution of the stress concentration around the notch [4].

The scenario when fatigue loading is considered is complex, due to the coupled interaction of load level, load ratio, and number of cycles. A key feature towards the understanding of failure of composites under fatigue is to understand the underpinning mechanisms associated with a specific load condition, evaluating whether there is a dominant mechanism that leads to degradation or if the final degradation is associated with the interaction of all failure mechanisms.

2.2 Fatigue damage propagation

Following an analogous approach used for metals, fatigue damage growth has often been modelled by applying power laws to describe damage propagation [4,7-9] to predict fatigue failure. Many efforts have been made to understand how fatigue damage affects CFRP properties, such as stiffness and strength [9-12], but despite all the theories and models proposed, significant uncertainties remain. The most common approach followed has been to consider each mechanism of damage as independent, without take into account any interaction. The Paris law [13] has been proposed as a starting point by Spearing *et al*. to describe 0˚ ply split propagation in double-notch cross-ply carbon/epoxy specimens subjected to fatigue loading [14]. The Paris law, usually expressed in terms of the stress intensity factor range (Equation 2.1), was considered in terms of energy release rate and split growth rate (Equation 2.2).

$$\frac{da}{dN} = \lambda_1(\Delta K)^m \tag{2.1}$$

$$\frac{dl}{dN} = \lambda_2(\Delta G)^{m/2} \tag{2.2}$$

In equation 2.1 the term $\frac{da}{dN}$ represents the crack growth rate, ΔK is the stress intensity factor range, and λ_1 with m are empirical constants [14]. In equation 2.2 the term $\frac{dl}{dN}$ represents the 0˚ ply split growth rate, ΔG is the energy release rate range, and λ_2 with m are empirical constants. Authors proposed to normalise ΔG by the toughness G_c measured under monotonic loading. The equation proposed to describe damage growth under fatigue is reported in 2.3, where λ_3 and m are constants for a specific matrix/interface [14].

$$\frac{dl}{dN} = \lambda_3\left(\frac{\Delta G}{G_c}\right)^{m/2} \tag{2.3}$$

Equation 2.3 represented the starting point to obtain a damage propagation law for specific load cases. Predictions obtained were reported to correlate well with

experimental results. Important drawbacks associated with the application of equation 2.3 are that it is not able to predict the damage path, to take into account residual stress, and to consider the interaction with other damage modes. Singh and Greenhalgh [8] reported high scatters associated with the use of the Paris law to describe fatigue delamination growth in epoxy-matrix composites. The mode I delamination growth of carbon/epoxy was described by Gregory *et al.* [7] as a function of the peak strain energy release rate G_{Imax} :

$$\frac{da}{dN} = A(G_{Imax})^m \tag{2.4}$$

where *A* and *m* are fitted parameters. The scatter obtained in the propagation rates as a function of the maximum strain energy release rate, was attributed to the fibre bridging that occurred during crack propagation, which are not taken into account by the power law [7]. Authors evaluated the main drawback associated with the use of a fatigue crack growth power law in composites design, which corresponds to the likelihood to have large errors. In fact, even if typical values of *m* for metals are below 5, they detected values of *m* in the range of 9-17 [7]. Therefore, since *m* appears in the equation 2.4 as an exponent, a small uncertainty in the applied loads could reflect a high error in the prediction of the damage growth.

2.3 Damage modes

Previous studies have shown the main damage modes associated with different load conditions and composite layups [4,15]. Matrix damage, delamination and fibre breaks are the most common damage modes detected under quasi-static loading [16-18].

2.3.1 Matrix damage: transverse ply cracks

Intralaminar failure commonly represents the first form of damage detected when a CFRP laminate is subjected to static or fatigue loading [19-21]. This damage mode consists of cracks extending through the thickness of a given ply, parallel to the fibres

in the specific ply considered. When the ply is oriented perpendicular to the loading direction, intralaminar cracks are identified as transverse ply cracks, whilst when the ply is aligned in the loading direction, they may be identified as 0˚ ply splits. In the case of cross-ply laminates subject to tensile load the first damage to appear is transverse ply cracks [18-20]. Early studies conducted by Harrison and Bader [19] on CRFP identified debonding of the fibre/matrix interface as responsible for transverse ply cracks initiation. Nairn [22] found that when a fatigue loading is applied, load amplitude affects the initiation and propagation of transverse ply cracks. In particular, low cycle stress (or high cycle fatigue) favours microcracking at the specimen edges followed by a slow propagation along the ply width. On the contrary, under high cyclic stress (or low cycle fatigue) microcracks that initiate at low crack density propagate along the ply width 'instantaneously', whereas microcracks that initiate at high crack density are characterised by a slow crack propagation rate. Even if transverse ply cracks are not considered critical in terms of final fracture, they contribute to reduced the stiffness and the transverse strength of a laminate [23].

2.3.2 Matrix damage: 0˚ ply split

Intralaminar damage developed along the loading direction (also identifiable as 0˚ ply splits) has been attributed to the presence of local shear stress [24], or a combination of shear and transverse stresses [25]. Previous studies on notched cross-ply CFRPs conducted under quasi-static load [16] identified split initiation at the notch section, consistent with the local stress concentration. With an increase in the load and/or number of cycles, splits are seen to propagate along the loading direction in the 0˚ ply. Spearing *et al.* [4] highlighted the major effect associated with the 0˚ ply splits growth in reducing stress concentration in the 0˚ ply at the root of a notch with the increase of crack length.

2.3.3 Delamination

Interlaminar damage between plies of different orientation is widely recognised as a key aspect of laminate failure [6]. Wright *et al.* [17] report that delamination does not

occur for quasi-static loads level less than 70% of the fracture strength in particle toughened double notched cross-ply carbon/epoxy coupons. Further investigations conducted by Scott *et al.* [18] on the same material and layup using *in situ* incremental quasi-static load provided the evolution of damage propagation with the load, see Figure 2.1.

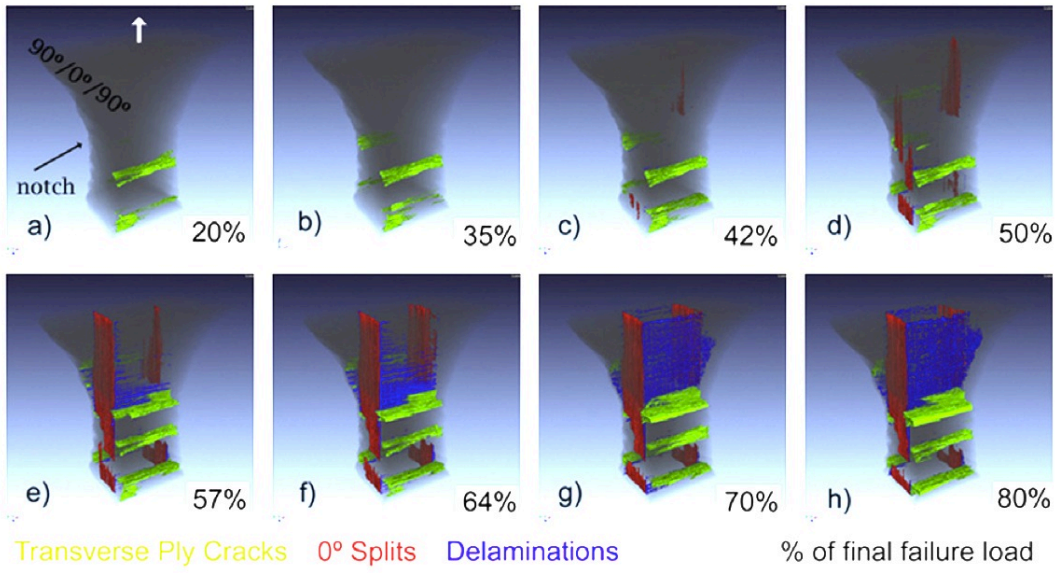

Figure 2. 1 - Damage progression under tensile loading from 20% to 80% of the final failure load [18].

The damage progression from 20% to 80% of the failure load is presented: the first damage detected was matrix microcracking perpendicular to the loading direction (transverse ply cracks), followed by the development of matrix microcracks along the loading direction (0˚ ply splits), with delamination then occurring for loads level above ~50% of final failure load. Recent studies conducted by Nixon-Pearson *et al.* [6] on an open-hole quasi-isotropic intrinsically toughened carbon/epoxy material highlighted that delamination does not occur for 40% of the static failure load and a number of cycles of 10^6. However, at higher peak loads they found that delamination reduces drastically the stiffness, and it was considered as the dominant mechanism on the failure process [6].

2.3.4 Fibre breaks

It is well known that fibre failure plays a fundamental role when a tensile load is applied, whilst it is widely considered that carbon fibres do not suffer degradation under cycled loads. Scott *et al.* [18] observed in a carbon/epoxy cross-ply coupon a cluster of 14 fibres breaks for a tensile load equal to 94% of the final failure load. However, this cluster did not appear on the previous load step (88% of the final failure load), showing that clusters of fibre breaks did not necessarily increase, but can occur directly as multiple breaks. The authors analysed the relations between fibre breaks and other damage, but a clear relation was not found between the locations of the transverse ply cracks and the fibre breaks within the 0˚ plies [18]. Conversely, Wright *et al*. [15] using an untoughened quasi-isotropic carbon/epoxy system observed a concentration of fibre breaks at the 45/0 interface, aligned with the split in the -45 ply.

2.4 Toughened composite systems

Highly cross-linked thermosetting epoxy polymers are used for CFRP applications where superior properties are required. In thermosetting polymers, the liquid resin is converted into a solid by cross-linking, which leads to the formation of a three-dimensional molecular network during curing. The resultant mechanical properties depend on the molecular units, on the length and density of the cross-links. The curing process plays an important role: the amount of crosslink created between molecules and the reactive groups affects the resin properties [26,27]. Lower crosslink density improves the toughness allowing greater strain before failure [28], whilst also reducing shrinkage during curing. On the contrary, a greater crosslink density results in an improved resistance to chemical attack, greater yield strengths, and higher glass transition temperatures [29]. In other words, an increase of cross-linking reduces molecular mobility, with a corresponding reduction in strain to failure, giving such thermosets systems essentially brittle behaviour with poor resistance to damage initiation and propagation [30].

Improving the fracture toughness of thermosetting resins has been the focus of several studies [31-35]. Important considerations to take into account are that the majority of

studies on toughening mechanisms have been performed with bulk resin, with corresponding behaviour in composites rarely being assessed. As such, toughening mechanisms detected for resin could be similar or quite different for composites, and consequently increases in toughness detected in resin may not find a correspondence in composite performance. Garg and Mai [27] in a comprehensive review on failure mechanisms in toughened epoxy-resin reported that the large increase in toughness found for bulk modified-rubber epoxies is poorly correlated with values observed when the resin is used as an adhesive or as the matrix in composite systems. They reported instances [27] where initiation fracture energies for unidirectional carbon-fibre reinforced composites using unmodified resin is similar to that for the bulk resin, however the response for composites with modified resin show only a modest increase of toughness compared with the enhancement obtained on bulk resin. Therefore, the improvement detected for toughened bulk resins, could not be directly translated to the composite systems when the same resin is used as the matrix. This has mainly been assumed to be due to the constraining action of the neighbouring plies [36].

2.5 Particle toughening approach

Methods used to improve toughness in thermosetting resins are frequently based on the insertion of particles of different composition and size. Strategies adopted are different, and for simplicity it is possible to divided them into three broad classes: rubber polymer particles, thermoplastic polymer particles and inorganic fillers (such as glass beads). This classification is not strictly rigorous, with some studies reporting hybrid approaches using two different types of particles [37,38]. The choice of the particle type and matrix affects the toughening response, but there are other parameters that influence the behaviour: particle size and content (in terms of volume percentage), particle distribution, and matrix/particle interfacial adhesion strength. Different combinations of the aforementioned parameters, together with diverse loading conditions, lead to various responses.

2.5.1 Effect of particle type

The use of rubber toughening particles has been shown to significantly increase fracture resistance in thermosetting resins, with corresponding degradation of elastic modulus, tensile strength, stiffness, creep resistance, stability at high temperature, and decreasing glass transition temperature [27,29,34,39]. Garg and Mai [27] reported an initial sharp decrease of elastic modulus, glass transition temperature and tensile strength corresponding to an increase of rubber particle volume fraction of 5%. However, these properties are then almost stable up to ~15% volume content. Due to their relative high modulus, high glass transition temperature and good ductility, thermoplastic particles are a clear, valid alternative to rubber particles [40]. The introduction of inorganic rigid particles for toughening has also been considered, including materials such as alumina, silica, glass beads and aluminium hydroxide [33,39]. This approach to toughening may reduce manufacturing cost and degree of shrinkage, increasing stiffness, strength, elastic modulus, and glass transition temperature [27,33,39]. However, the increase of fracture toughness is moderate, especially for low volume fractions [33].

2.5.2 Effect of particle volume fraction

In many studies conducted previously it is difficult to distinguish the contribution of individual material parameters to toughness modification, because in most cases it is not trivial to decouple the different effects that act simultaneously. He *et al*. [41] conducted studies using preformed rubber particles, with the aim to decouple the effects of rubber morphology (particle size and distribution) that are intrinsically present due to the polymerisation processes. Therefore, they maintained the particle size (average diameter of 0.5 μm) and particle distribution constant, whilst varying particle concentration. Their results showed that fracture toughness increased with the particle content up to a maximum/optimum value. Beyond this, a further increase of particle content led to a decrease in toughness. The fall in fracture energy associated with an increase of particle content is clearly not related to a change in morphology (it is relatively constant in this case). He *et al.* [41] associated this drop

with a point in increasing particle concentration where the remaining matrix volume available is not sufficient to generate toughening mechanisms such as yielding and plastic flow. Becu *et al*. [42] considered two types of core-shell rubber particle with different core composition (poly butyl-acrylate and poly butadiene-co-styrene), and evaluated the effect of the particles' content on the fracture toughness. Average size particles were 0.3 and 0.2 μm respectively. They found a progressive increase in fracture energy with the increase in rubber shell particles; however, they identified the maximum/optimum content for their experiments. Ling and Pearson [43] have further considered hybrid solutions using bisphenol-A based functional prepolymers (DGEBA) resin epoxy toughened with carboxyl-terminated butadiene-acrylonitrile (CTBN), which leads to rubber particles in the range of 2-3 μm, and silica nanoparticle of 20 nm and 80 nm respectively.

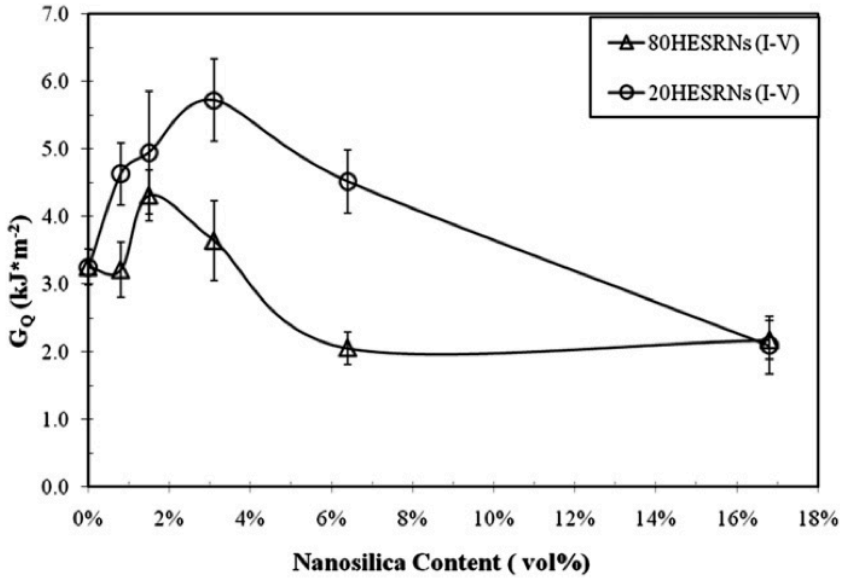

Figure 2. 2 – Effect of nanosilica particle content on fracture energy in a hybrid epoxy [43].

The volume content of nanoparticle affects the toughness, Figure 2.2, shows an optimum value of nanoparticle content for the two systems considered. The reason for the drop in fracture energy for higher nanoparticle content was reported to be the formation of agglomerations, favoured at higher volume fraction, and more sensitive for smaller particles.

2.5.3 Effect of particle size

Pearson and Yee [37] observed different toughening mechanisms when the particle size was varied. They considered DGEBA epoxy resin with various particle systems: particles with a variety of diameters (1-200 μm), and core-shell rubber with a predetermined diameter of 0.2 μm. Their results showed an increase in fracture toughness with a decrease in particle size, obtaining a maximum for the system with core-shell particles. For this latter case, the enhancement of fracture toughness was approximately five times than the system containing large particles (100 μm). Authors explained the particle size dependency in terms of the fracture 'process zone', where this is represented by the crack tip plastic zone [32]. Therefore, the particle size effect appears as a particle-plastic zone interaction. In particular, they argue that large particles (100 μm) result in being outside of the crack tip plastic zone but can still act as bridges and promote crack path deflection, providing a modest increment of toughness. Instead, smaller particles (1 μm or 0.2 μm) are in the crack tip plastic zone, undergoing cavitation process, which relieves load and facilitates shear-band formation [32].

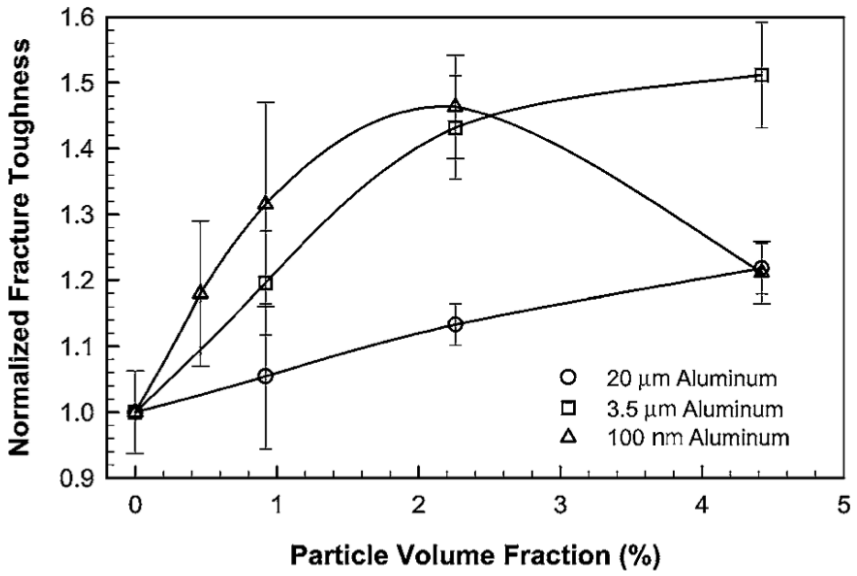

Figure 2. 3 – Fracture toughness as a function of particle volume content and aluminium particle size [39].

Singh *et al.* [39] have examined the effect of the size of aluminium particles in polyester. A range of sizes was reported, from micrometer to nanometer scales: 20 μm, 3.5 μm and 100 nm. They detected similar behaviour for all systems by fracture surface inspection. According to their results, the main toughening mechanism was identified as crack front trapping: the presence of particles prevented crack growth in the matrix. Particle size did not affect the activation of this mechanism. However, an increase in fracture toughness was detected with a decrease in particle size for a given value of particle volume fraction, see Figure 2.3. The opposite trend has been reported by other authors [44-46], where an increase of fracture toughness corresponds with an increase in particle size. Nanoparticle toughening of epoxy systems has been widely used recently. Studies have confirmed that adding nanoparticles to neat resin may indeed increase fracture toughness [47-49]. However, the effectiveness of nanoparticles compared to micro-meter-sized particles is not clear, as most studies report on the enhancement of toughness compared with the neat epoxy and not directly with an equivalent system with micrometer scale particles.

2.6 Toughening mechanisms

Different toughening mechanisms have been reported in the literature and they can potentially contribute to increasing fracture toughness by processes that involve energy dissipation. Most of the mechanisms identified were drawn from fractographic analyses (observing fracture surfaces using micrographs). One of the questions raised by Pearson and Yee [37] is regarding the misleading results obtained using fracture surfaces as representative of the events occurring. In this contest the use of computed tomography might overcome the introduction of artefacts, providing a 3D representation, and allowing the identification of toughening mechanisms in neat resins.

The main toughening mechanisms identified for epoxy resins are schematised in the Figure 2.4, as reported in a review by Garg and Mai [27]. They are: shear band formation near the rubber particles (1), fracture of rubber particle (2), stretching of

rubber particle (3), debonding of rubber particle (4), tearing of rubber particle (5), transparticle fracture (6), debonding of hard particles (7), crack deflection by hard particles (8), cavitated or voided rubber particle (9), crazing (10), plastic zone at crack tip (11), diffuse shear yielding (12), shear/band craze interaction (13), and pinning of the crack front. These mechanisms do not occur simultaneously and their activation depends of different factors that are explained briefly in the following sections. Their contribution to the enhancement in toughness in turn depends on the parameters already described in the previous sections, such as particle type, size, distribution, volume fraction, and matrix/particle interface.

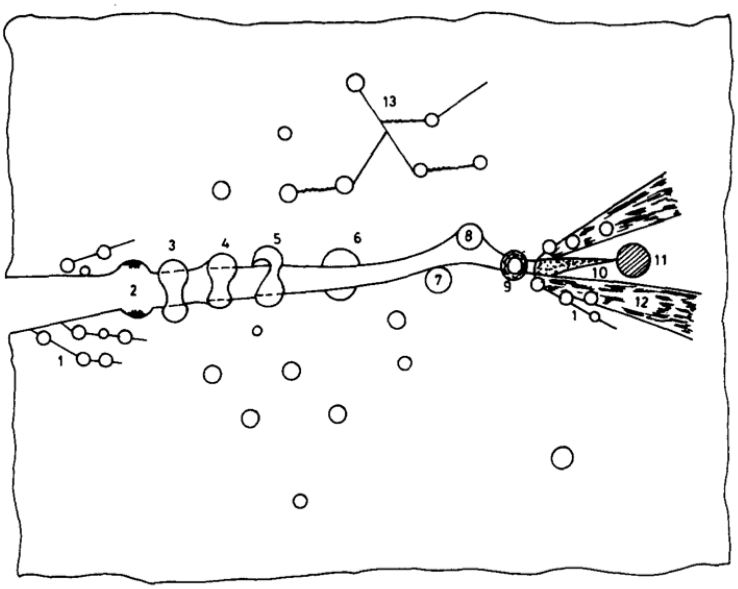

Figure 2. 4 – Toughening mechanisms for particles modified epoxies, reported by Garg and Mai [27].

When particles are interposed along the crack propagation plane they can be subjected to bridging, stretching and tearing, or debonding. In particular, bridging happens when a particle spans the two crack surfaces, applying a traction that reduces the local stress concentration at the crack tip [31]. Crack bridging is reported as a typical mechanism associated with stiff polymer particles [36]. The increase of toughness is associated with the elastic energy stored in the particle during bridging or stretching, which is dissipated in the moment that the particle fails [27]. Kunz-Douglass *et al*. [50] identified bridging as the main toughening mechanisms in rubber-modified epoxy. They attributed toughness enhancement only to the particle, which dissipate

energy during the tearing process. In other words, particles act as springs, bridging the matrix crack, and the elastic energy contained within the rubber particle is dissipated when these undergo tearing. The improvement to toughness consists of a reduction of stress intensity at the crack tip due to the action of the particles along the crack wake.
Crack pinning is another mechanism, in which the particles act as an obstacle to crack front propagation and this results in bowing of the crack front between the particles, see the schematic of Figure 2.5. The concept of crack pinning was proposed for the first time by Lange [44], who observed a change in length of the crack front, associated with the particle interaction. This process involves energy dissipation and contributes to increased toughness. In the literature it is mostly associated with hard particles [33,51], or cases where the difference between the toughness of the epoxy and particle is appreciable, such as the case of thermoplastic particles [31].

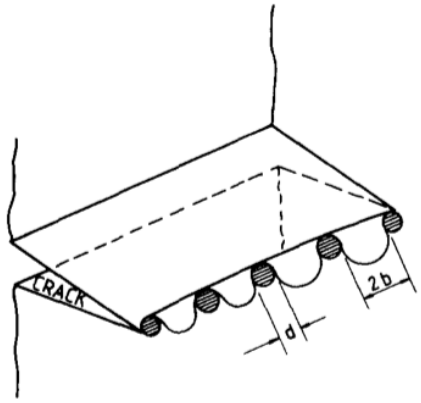

Figure 2. 5 – Crack pinning mechanism as reported by Lange [44].

Crack deflection is the mechanism by which the crack is deviated by one or more particles, resulting in an increase of fracture area, which causes an increase in energy absorption during crack propagation [31]. An indication of crack deflection is the roughness of the fracture surface, which increases if deflection processes occur. Bascom *et al.* [52] interpreted large holes formation as the result of particle and matrix deformation. In addition, particle nucleation is also responsible for local shear yielding of the matrix. Yee and Pearson [34] identified shear yielding as the major source of energy dissipation. The rubber particles dissipate the bulk strain energy by cavitation, followed by shear localization processes. Particles in first instance act as stress concentrators, enhancing shear localisation. Secondly, cavitation processes promote

shear deformation, which in turn produces blunting of the crack tip and consequently leads a reduction in the local stress concentration, and consequently of the crack propagation [53].

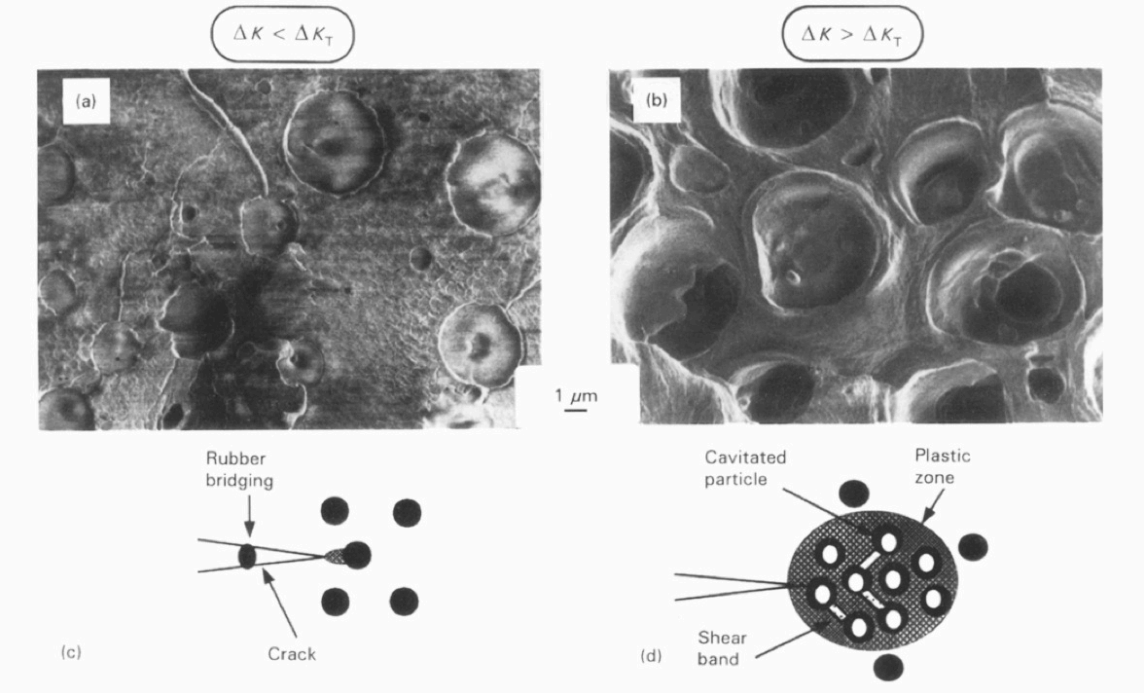

Figure 2. 6 – Scanning electron micrographs of fatigue fracture surface for lower (a) and higher (b) values of the transition point with corresponding schematization of the crack-tip/plastic-zone interaction (c) and (d), [32].

Azimi *et al*. evaluated the role of rubber particles in epoxy matrices under fatigue loading [32]. The results were referred to a transition point in the stress intensity factor range, ΔK_T, where ΔK is the stress intensity factor range defined as $\Delta K = k_{max}-k_{min}$. The transition occurs for a specific K level, which corresponds according with the authors to the condition where the plastic zone is the same of the particle size. Fracture surface analyses showed no evidence of plasticity for $\Delta K<\Delta K_T$, and they attributed this to the fact that the plastic zone size was less than the size of the rubber particles. The main mechanism detected in this zone was particle bridging, Figure 2.6 (a) and 2.6 (c). For $\Delta K>\Delta K_T$, where the plastic zone is larger than the particle size, cavitation and shear yielding have been identified, Figure 2.6 (b) and 2.6 (d).

The use of thermoplastic particles leads to different mechanisms, Pearson and Yee [31] using DGEBA resin with poly-phenylene oxide, reported multiple crack bifurcation as

main toughening effect, even if bridging was also detected. In this last case no shear bands and no evidence of plastic zone were found.

Different toughening mechanisms are reported for systems that use nanoparticles [48,49]. Johnsen *et al.* [49] did not detect any pinning and crack deflection mechanisms, employing well-dispersed silica nanoparticles with a size of 20 nm in DGEBA epoxy resin. They attributed the inability to activate these mechanisms, typical of rigid fillers, to the size of the particles, which were smaller than the crack opening displacement. Toughening mechanisms recognised for nanoparticle are voids that surrounded nanoparticles, particle debonding and subsequent plastic growth [49]. Liang and Pearson [43] observed that crack pinning could not be excluded in the case of nanoparticle agglomeration, which could provide a cluster-particle size larger than the crack opening displacement. However, the toughening effect associated with the cluster nanoparticle is less than that achieved with silica micro-size particles, due to the weak internal bonding between nanoparticle as they formed agglomerations [43].

Studies in the literature confirmed that pinning and bridging are typical mechanisms of rigid particles, whereas cavitation and shear band formation are characteristic of rubber particles. The main contribution in terms of toughness enhancement is due to pinning and plastic deformation (shear band formation) for these two types of particles respectively. Other processes that contribute to energy dissipation are present, such as bridging, debonding and crack deflection. However, according to the evaluation done by different authors already mentioned, these latter toughening mechanisms contribute to the toughness enhancement to a lesser extent.

2.7 State of art: toughened CFRP

The improvement of the resin in terms of toughness fracture can be an advantage when these types of matrix are employed in fibre composites. However, the effectiveness found for bulk resin could not be maintained when the epoxy is used as matrix in composite systems [36]. There are limited studies in the literature that investigate the behaviour of toughened polymer composites, and to date this is not enough to have a clear understanding of the toughening mechanisms and possibly

their contribution in terms of toughness improvement. Kim *et al.* [54] evaluated the transverse impact fracture of unidirectional carbon fibre across a range of temperature from -45 ˚C to 80 ˚C. DGEBA matrix and six different combinations of particle were used, which resulting in the following systems: unmodified epoxy, epoxy modified with rubber particles (CTBN), epoxy with Al_2O_3 fibre, epoxy with Al_2O_3 powder, rubber-modified epoxy Al_2O_3 particle, and rubber-modified epoxy Al_2O_3 powder. The volume fraction of fibre considered was low, V_f = 0.2. Results show that in the range of temperature considered the fracture toughness for composites with modified resin do not exhibit significant improvement with respect to the use of unmodified epoxy, but are characterised by similar values. Authors attributed this to the fact that toughening mechanisms in the transverse direction associated with unidirectional fibres are mainly related to fibre breaks and fibre/matrix interface, whereas matrix deformation contributes to a smaller extent to the total fracture toughness [54]. The main toughening mechanism identified was fibre pull-out for all systems.

Gao *et al*. [55] studied mode II delamination for unidirectional carbon/epoxy interleaved using thermoplastic particles. They investigated three different interleaved systems and one non-interleaved system. Their results showed that mode II interlaminar fracture toughness (G_{IIC}) of two interleaved systems considered is approximately double that of the corresponding non-interleaved system. The drop in the fracture toughness for the other interleaved system was associated with the chemical incompatibility between the matrix and the thermoplastic particles. Fracture surface observations were used to understand the toughening mechanisms involved. The non-interleaved case presented a smooth crack surface, which indicates a poor resistance to delamination propagation. In contrast, the interleaved system exhibited crack propagation within the interlayer following a non-straight path. The presence of crack-path deflection and failure of thermoplastic particles were identified as the main mechanisms that contribute to enhance fracture toughness absorbing energy [55]. Fracture surface observations for quasi-static indentation (QSI) showed large delamination for the case of non-interleaved system, whereas in the interleaved system the crack propagation was controlled by particles. The toughening mechanisms identified to be involved in the process of energy dissipation were: particles fractured by the crack and crack deflection along the interface [55]. Therefore, interleaved

systems exhibit greater damage resistance due to the toughening mechanisms activated by the presence of resin rich regions with thermoplastic inside. According to the authors' observations, the presence of the interlayer suppresses delamination and absorbs energy [55].

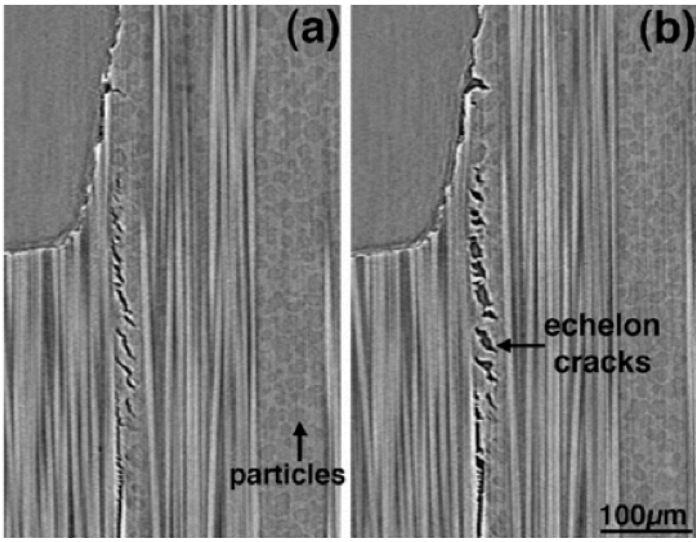

Figure 2. 7 - Damage 0˚ ply splits for the sample unloaded and loaded with at 50% UTS. Echelon cracks are due to the presence of rubber particles [16].

Moffat *et al.* [16] investigated the micromechanisms in notched toughened carbon/epoxy contained toughening particles using computed tomography. They observed echelons, micro-cracks oriented at 45˚ respect to the loading direction, in the range of 20 μm associated with toughening particles action that under quasi-static load was subjected to decohesion, as shown in Figure 2.7.

Damage quantification of 0˚ ply splits, using the crack opening displacement, highlighted that the presence of particles affects crack propagation: the crack front is not uniform and its development is clearly retarded in the resin rich regions, which contained the majority of toughening particles [16], Figure 2.8. The authors observed also debonding particles and bridging ligaments between the echelon cracks due to the action of the particles [16].

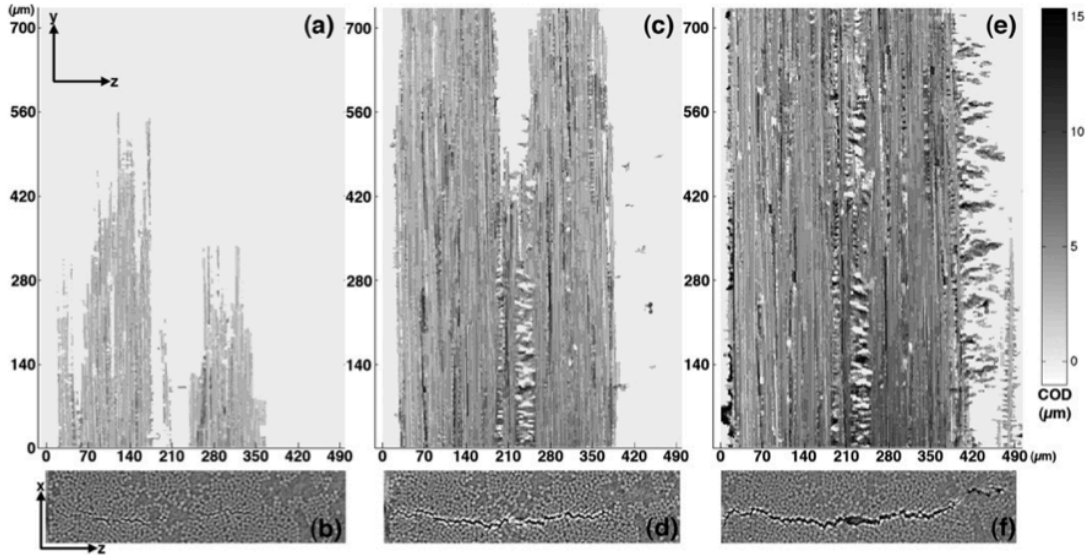

Figure 2. 8 – Crack opening displacement for 0˚ ply splits at 40% - 50% -60% UTS [16].

Bull *et al.* [56] assessed the damage resistance to low velocity impact of unidirectional and quasi-isotropic carbon/epoxy laminates containing thermoplastic particles via computed tomography. An untoughened system with same properties in terms of type of fibre used and fibre volume fraction was also considered for comparison. Impact damage was extracted and represented in 3D, Figure 2.9 [56]. Results showed that the presence of toughening particles constrain delamination [56]. It is clear that for the untoughened system the amount of delamination (indicated in blue) is consistently greater than for the toughened system, as reported in Figure 2.9, even though the level of energy used for the untoughened system was smaller. The presence of particles does not affect intralaminar cracks, illustrated in red in Figure 2.9. However, a more accurate comparison needs to be done considering the same energy level between the toughened and untoughened systems. The toughening mechanisms identified are crack deflection and bridging within the resin rich regions. However, the authors raised an interesting point on the cause of these two mechanisms, also observed for the untoughened system in the resin rich regions. The not well-understood behaviour on toughening mechanisms is represented by the fact whether they are directly related to the particles exclusively, to the resin rich regions or to an interaction of both [56]. Further investigations conducted by Bull *et al.* [57] were aimed to evaluate the toughening contributions to the enhancement of the observed damage resistance [56].

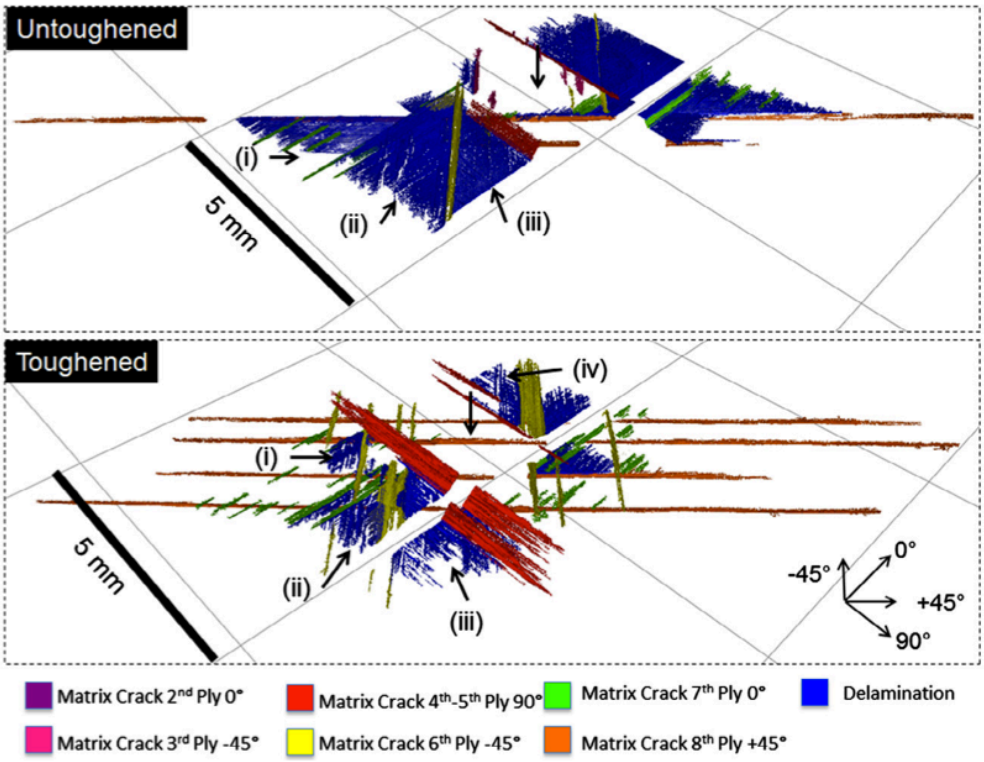

Figure 2. 9 – Impact damage segmentation for un-toughened system (0.6J), and toughened system (1.2J), [56].

The authors concluded that the main toughening mechanism is represented by the ligament formation, which were correlated with the observed increase in toughness [57]. A recent study conducted by Borstnar *et al.* [58] on crack growth under Mode I and II for toughened particle systems has shown that the particles in the resin rich regions deflect the crack path from the ply/interface back to the interlayer by particle debonding processes. The increase of toughness was associated with the mechanisms of crack deflection and bridging ligament formation [58].

2.8 Non-destructive investigation technique

Different non-destructive techniques have been employed historically to detect damage in composites: for example, ultrasonic C-scans to evaluate delamination [59-61], acoustic emission to monitor the formation and growth of damage [62-65], thermography and thermo-elastic stress analysis to correlate damage and surface

strains [66,67]. These methods have intrinsic limitations, such as the inability to provide direct information on type, size and orientation of damage, to resolve fine-scale failure events (*e.g.* fibre/matrix debonding and fibre breaks), and to provide a thorough, microscopic three-dimensional representation of damage. In this respect, computed tomography (CT) has become established as a powerful technique for contemporary material science studies, facilitating multiscale analysis (macro-, meso-, micro- and nano-scale) of material structure and damage detection [68-72]. CT has for example been used on fibre-reinforced polymers to evaluate the local volume fraction and the orientation of reinforcement [73], to assess voids and internal damage in glass/epoxy [74,75], and to investigate fibre fracture of quartz/epoxy bundles [76]. Previous studies conducted on CFRPs have demonstrated that high resolution CT allows the imaging of damage at the scale of individual broken fibres [15], and that a voxel resolution on the order of one micrometer is reasonable to detect and distinguish primary damage modes [18]. Damage of carbon/epoxy subjected to impact and quasi-static loading has been quantified using Synchrotron Radiation Computed Tomography (SRCT) imaging, evidencing multiscale interacting 3D failure processes [16,18,56]. The comparison between data achieved by the use of SRCT and micro-CT has shown that micro-CT represents a valid alternative, especially when wider field of views need to be captured [77,78].

2.9 Computed Tomography: background

An X-ray is an electromagnetic wave characterised by wavelengths in picometer to nanometer range, as shown in Figure 2.10. Conventionally, the unit to measure X-ray energy is the eV. Wavelengths in the range of 10 nm - 0.1 nm correspond to energy in the range of 124 eV - 12.4 keV, which are commonly identified as *soft X-rays*, while wavelengths in the range of 0.1 nm - 0.01 nm are correlated with energy from 12.4 keV to 124 keV, are known as *hard X-rays* [79]. Hard X-rays (higher energy) are able to penetrate denser materials. Synchrotron radiation uses electrons accelerated and deflected in a magnetic field to produce X-rays (also called synchrotron light). In an

equivalent way also other particles, such as proton could be used following the same principle to generate X-ray (i.e. acceleration of charge particles).

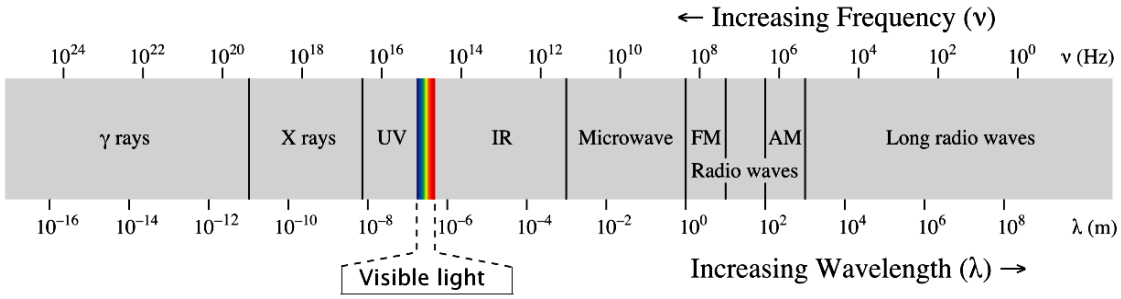

Figure 2. 10 – Electromagnetic spectrum [80].

In the energy range of hard X-ray, which represents the level of energy used to penetrate materials in this study, the main interaction between the X-ray photons and matter are: photoelectric effect, Compton effect and coherent scatter (or Rayleigh scatter). The type of interaction, and consequently the percentage of energy transferred from each type of interaction, depends mainly on the level of energy (*E*) used and on the atomic number (*Z*) [79]. In correspondence with the moderate energy used in this work (<20 keV), the percentage of energy transferred after the attenuation is associated only with the photoelectric effect for the low *Z* elements involved, while the Compton effect assume a fundamental role for much higher energy. The effect of the aforementioned interactions is represented by the X-ray photons absorbed when they pass through the object. Hence, the output is represented by an attenuated intensity, which is recorded by the detector. The easiest case that can be considered is an object represented as homogeneous and the radiation as monochromatic. The Beer-Lambert law gives [79,81] the intensity of the radiation obtained after the interaction with the object:

$$I = I_0 e^{-\mu L} \tag{2.5}$$

where I and I_0 are the transmitted and incident radiation respectively, μ is the linear attenuation coefficient of the material and L the thickness of the object. The attenuation coefficient is equal to the sum of the attenuation coefficients of the

photoelectric effect, Compton and coherent scattering interactions. As noted above, in the range of energy considered here, the attenuation coefficient is dominated by the photoelectric coefficient of attenuation. The attenuation is defined as the logarithm of the ratio of the incident intensity to the transmitted intensity [82], which in this specific case of homogeneous object and monochromatic radiation is:

$$P = \ln \frac{I_0}{I} = \mu L \tag{2.6}$$

and consequently the attenuation coefficient is given by:

$$\mu = \frac{1}{\mathrm{L}} \ln \frac{\mathrm{I_0}}{\mathrm{I}} \tag{2.7}$$

The equation 2.5 represents an ideal condition; in the real cases objects are not homogeneous. Therefore, whether the hypothesis of monochromatic radiation is still valid, the equation 2.5 for an inhomogeneous object becomes:

$$I = I_0 e^{-(\mu_1 l_1 + \mu_2 l_2 + \mu_3 l_3 ..)} = I_0 e^{-(\sum_{i=1}^{n} \mu_i l_i)} = I_0 e^{-\int_0^l \mu dl} \tag{2.8}$$

The attenuation is given by:

$$P = \ln \frac{I_0}{I} = \sum \mu_i \, l_i \tag{2.9}$$

where μ_i is unknown. The more generic case to consider is the presence of polychromatic radiation with an inhomogeneous object. The coefficient of linear attenuation is also function of the energy and the equation 2.5 should be modified as:

$$I = \int_0^{E_{max}} I_0(E) \, e^{-\int_0^L \mu(E) dl} \tag{2.10}$$

As mentioned, the linear attenuation coefficient μ in the range of incident energy considered is due to the photoelectric effect, and assumes the form:

$$\mu(x, y, z) = \mathrm{K}\rho\frac{Z^4}{E^3} \tag{2.11}$$

where *K* is a constant, *ρ* is the material density, *Z* the material atomic number and *E* the energy of the incident photons.

2.10 X-ray computed tomography: principle

The word tomography is derived from the Greek 'tomos' (section) and 'graphein' (to write), with the meaning to represent something by sections. Computed Tomography (CT) represents an evolution of traditional radiography where features appear superimposed due to the projection of all volume information into a two-dimensional imaging plane. The main limitation associated with radiography is the reduced visibility and shadowing with consequent difficulty of understanding the three dimensional arrangements of the components within the object under investigation [83]. This issue is overcome by the use of X-ray computed tomography (CT), which was initially developed for medical applications in the early 1970's [82]. After a few decades, the same principle was exploited to investigate other fields, such as materials science, biomedical science, archaeology, palaeontology; gaining considerable interest among the non-destructive methods community [68]. Consequently, the number of laboratory facilities (microfocus computed tomography) and high-scale facilities (synchrotron radiation computed tomography) that allow these analyses to be performed increased over the last few decades.

The principle of X-ray CT is quite simple and is based on the measurement of the attenuation of X-ray photons due to the interaction with matter for different angular positions, as already explained in the Section 2.9, and shown in the schematic provided in Figure 2.11. The object is placed on a rotating stage and a number of attenuation measurements are collected for different increment of rotations, called projections. In other word, a single projection represents the transmitted photons for the specific section (or X-ray path) of the object.

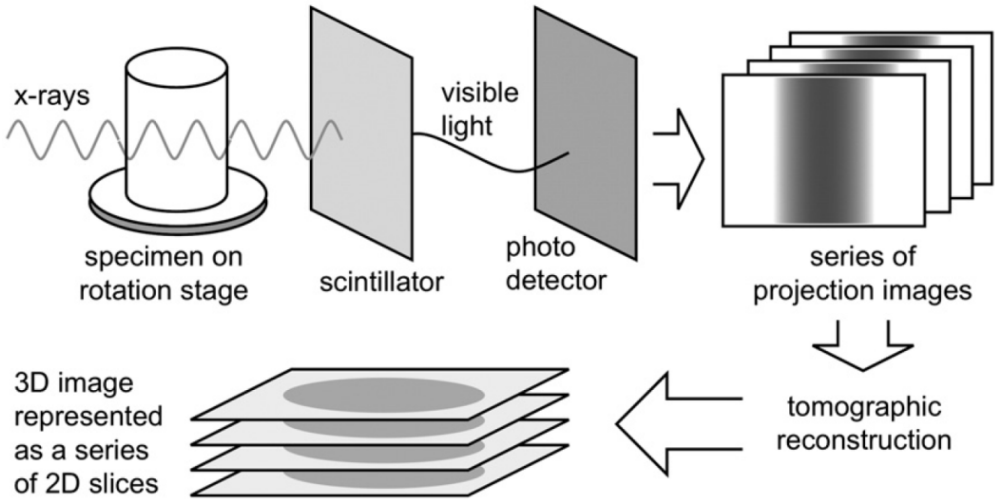

Figure 2. 11 - Schematisation of X-ray Computed Tomography acquisition and reconstruction to produce a 3D map of X-ray absorption in the volume [83].

The object is rotated thorough an angle of 180° when a synchrotron source is used due to the availability of a parallel beam, while laboratory microtomography, that employs a divergent cone beam, requires >180° for complete angular coverage of all areas (centre to edge). During the rotation, attenuation of the incident X-ray beam is measured for a finite number of angular increments, equal to the ratio between the number of projections and the total rotation required (180° or 360°). The optimum number of projections is linked to the width of detector in pixels, and depends on the reconstruction method: for back projection, ~1.5*n* is typical, where *n* is the number of pixels. Projections are effectively combined by reconstruction software: as overall beam attenuation along a path may be represented as a line integral of attenuation coefficients along that path, reconstruction is effectively an inverse-Radon transform. When sufficient projection data is available, filtered back projection is commonly identified as a rapid and robust reconstruction method (see Section 2.11).

The field of view achieved is proportional to the voxel resolution used. Therefore, high resolution involves a smaller field of view and vice versa. Contemporary detectors are typically ~2000 x ~2000 pixels. The field of view achievable by a fixed voxel resolution can be easily calculated multiplying the resolution chosen and the number of pixels of the detector.

2.11 Tomographic reconstruction

When a series of projections of the object are acquired, the next step is represented by the reconstruction of the distribution of the linear attenuation coefficient. Initially, algebraic reconstruction techniques (ART) were used, based on an initial guess of the attenuation distribution, iterated until the calculate projections corresponded with the measured projections [79,84]. The main drawback associated with this type of reconstruction is the computationally intensive processing, which does not allow the reconstruction to be obtained in a reasonable time, as required from modern CT equipment, which is able to acquire a single projection in a fraction of second (the exposure time). Filtered Back Projection Reconstruction (FBP) is faster and most of the software associated with commercial microfocus CT systems has this embedded within. An intuitive explanation of the filtered back projection approach is provided by Hsieh [79] and is shown schematically in Figure 2.12. In the example, taken into account an object represented by a single point, we assume that at the beginning we do not know anything about the object.

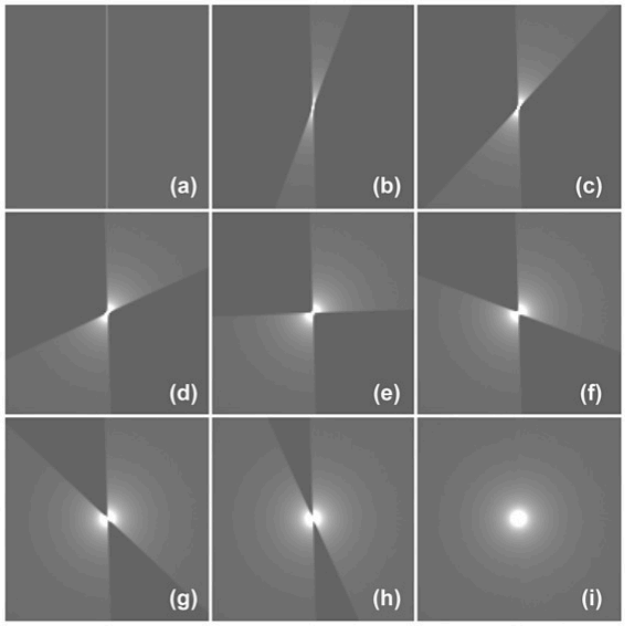

Figure 2. 12 - Back projection filtered approach [79].

The first X-ray path is vertical and perpendicular to the point (Figure 2.12(a)), but this information is not enough to understand where X-ray attenuation is located along the line. Additional X-ray paths (and consequently projections) corresponding to different angular positions (from Figure 2.12(b) to Figure 2.12(i)) provide further information to localise the position of the attenuating point. In this specific case each projection is represented by an impulse function with the peak centered in correspondence of the location where the X-rays intersect the object. This is valid for each single projection. Essentially the algorithm reverses the projections providing the 2D representation (Figure 2.12). For this reason the process is known as *backprojection*. As it is clearly visible from Figure 2.12(i), the final position of the object (point) has been identified, but the backprojection yields a blurred representation. The blurring can be understood by the profile of the reconstructed point, Figure 2.13. The black line is the representation of the object (image), while the real object is the grey line.

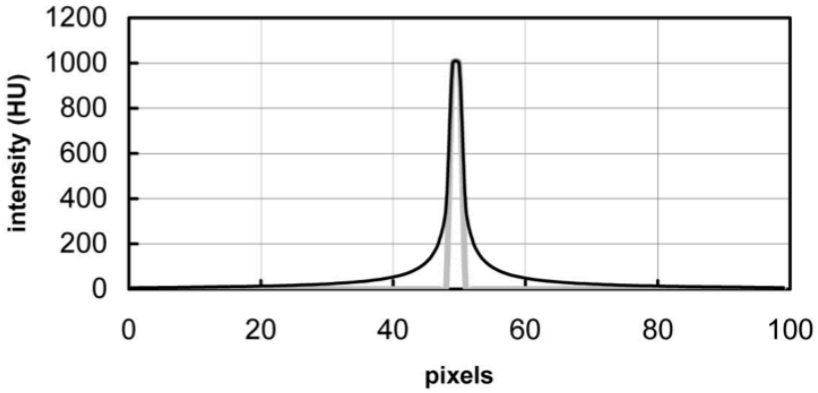

Figure 2. 13 - Profile of a reconstruction point: solid black line represents the reconstruction using backprojection and the grey line is the profile for the ideal reconstruction, which corresponds with the real object [79].

Since the final representation obtained in Figure 2.12(i) is the impulse response of the backprojection method, it is possible to obtain the original object by the deconvolution of the backprojections with the inverse of the impulse response [79]. This process is known as *filtered back projection*. A direct comparison between the application of the backprojection and filtered-backprojection method is shown in the example provided in Figure 2.14.

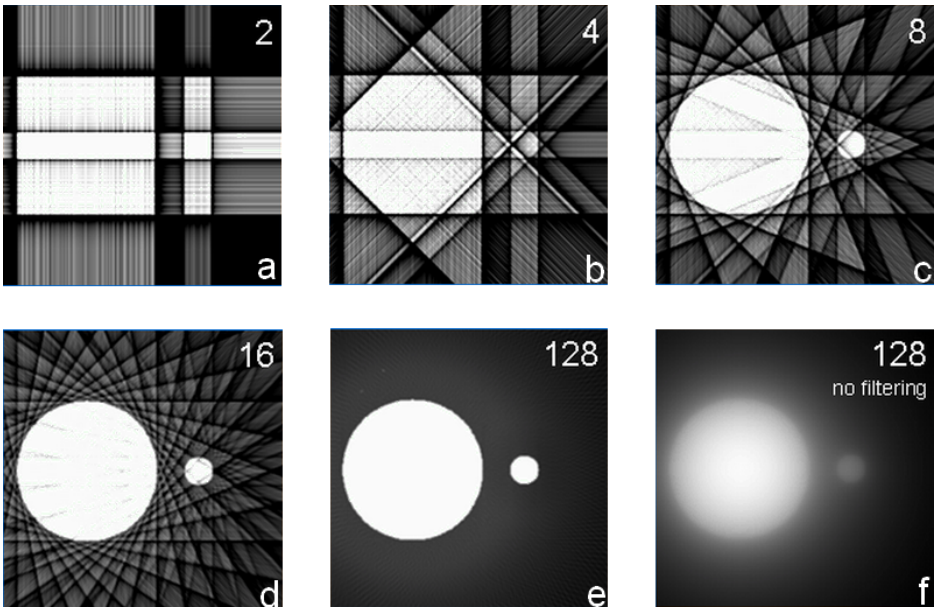

Figure 2. 14 - Filtered back projection algorithm application for different number of projections for 2,4,8,16,128 number of projections respectively (a,b,c,d,e) and comparison with the back projection algorithm (f) [85].

The method used for the reconstruction of the scans performed during this work at the Swiss Light Source is an in-house code based on the *gridrec* algorithm, which allows faster reconstruction than FBP and therefore, represents an alternative to the conventional filtered-backprojection method [86]. This reconstruction approach is based on the Fourier Transform Method (FTM) and uses the *gridrec* algorithm as the gridding method to resample the Fourier space from polar to Cartesian coordinates [87]. The solution, based on the interpolation in the 2D Fourier domain, depends on the number of projections acquired. Therefore, by increasing the number of projections, the signal-to-noise ratio is improved with respect to the traditional FBP [86].

2.12 Synchrotron radiation computed tomography

Two different types of sources are commonly used to produce X-rays for scientific CT applications: lab sources, also called microfocus CT, and synchrotron radiation facilities. The current work exploits synchrotron radiation computed tomography (SRCT) and the

focus in this section is the description of the main components of SRCT and how it works to produce X-rays.

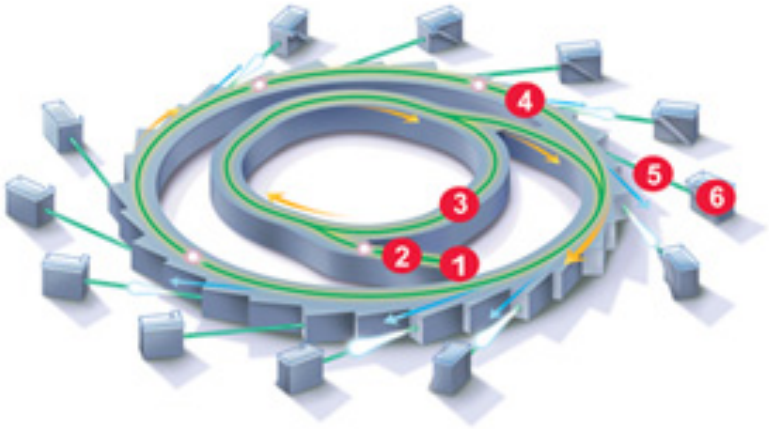

Figure 2. 15 – Schematisation of the main components of a SRCT facility: (1) electron gun, (2) linear accelerator, (3) booster, (4) storage ring, (5) beamlines, and (6) experiment stations [88]. (The schematisation is referred to the Australian Synchrotron, Illustrator: Michael Payne).

The Swiss Light Source (Paul Scherrer Institute) has three main parts, as schematized in Figure 2.15: a linear accelerator (called the linac) where the electrons are pre-accelerated up to an intermediate energy of 100 MeV [89], a circular accelerator with a diameter of 270 m (called the booster) where the electrons coming from the linac are further accelerated up to 2.4 GeV. The electrons in this final energy stage have a speed close to the speed of the light. The electrons from the booster are periodically injected into the storage ring keeping the intensity of the electrons constant. In the storage ring (diameter 288 m) electrons circulate for many hours generating X-rays via the various bending magnets and insertion devices present (see Figure 2.16). The presence of a high-vacuum system reduces the losses of electrons due to collisions maintaining the circulating beam for ~10h with small losses [89]. The storage ring contains magnets that force the electrons to follow a circular path. Bending magnets have a uniform dipole, which accelerates the electrons along an orbital trajectory within the storage ring, as schematized in Figure 2.16. The electrons in a bending magnet (represented in blue in Figure 2.16(a)) are accelerated as they are forced along a circular path in a strong magnetic field, and as a consequence they emit a continuous spectrum of synchrotron light (represented in yellow in Figure 2.16(a)) as they travel.

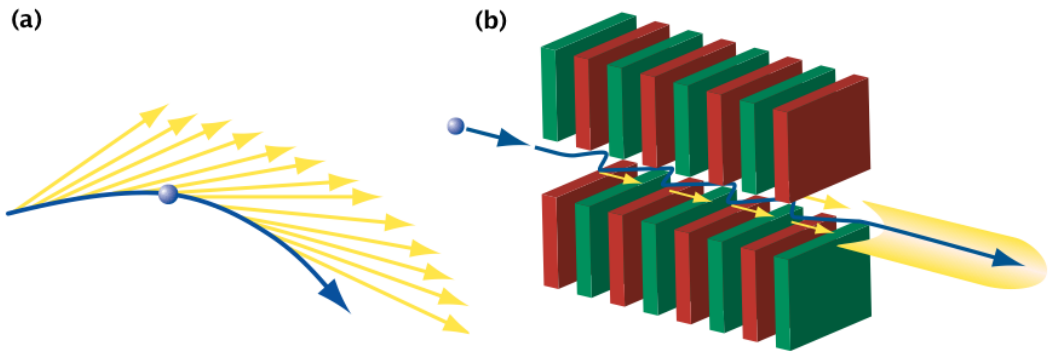

Figure 2. 16 - Schematization of (a) bending magnet, (b) undulator or wiggler magnets [90].

The SLS storage ring belongs to the so called 'third generation light source', which use insertion devices (typically 'undulators' & 'wrigglers') to generate the desired X-ray beam for a given experiment type. These can be thought as many magnetic beam deflectors installed next to each other [90], see Figure 2.16(b). The result is a very narrow cone beam and an increase of intensity/brightness of roughly 1000 times with respect to a bending magnet [89].

2.13 Artefacts

Reconstructed CT volumes typically use simple greyscale representation of the coefficient of linear attenuation. Many factors could interfere in this process, creating a final result that is different from the original object. All these potential sources of error are called artefacts, and have different consequences and solutions [79,81,91,92]. Artefacts appear as 'distortions' of the image (when the easiest case of a single 2D slice is considered) that affect the overall image quality, and in the worst case hides and/or compromises the information contained. It is clear that the presence of artefacts can introduce significant errors when CT data are used for quantification. The most common artefacts are [79,81]:

- Beam hardening, associated with a polychromatic X-ray spectrum and with the energy dependence of the attenuation coefficient. When a polychromatic source is used, most materials absorb X-rays at lower energy easily (due to photoelectric absorption), and this determines a change in the energy

spectrum that causes beam-hardening artefacts. These artefacts are not typical of synchrotron sources, where monochromatic radiation is used. Beam hardening can cause streaking artifacts, cupping or shading on the reconstructed images.

- Ring artefacts appear as concentric dark or bright rings centered on the rotation axis. They are due to the presence of individual miscalibrated or defective pixel elements in the detector. Therefore, when the object rotates during the scan, the greyscale deviation associated with the defective element traces a ring.
- Motion artefacts are due to movements that can occur during the scan or the setup of the scanner. The misalignment between the centre of rotation of the stage and the centre of rotation of the specimen causes blurring, such as double images, and crescent streaks.

Some artefacts can be corrected using specific software in the post-processing. However, not all artefacts can be avoided and/or corrected (e.g. some beam hardening effects will occur when polychromatic X-ray sources are used for imaging).

2.14 Phase contrast

When an X-ray beam passes through the object there is an interaction with the electrons of the object that creates a phase shift [93,94]. Interference of the phase shift patterns in the wavefront is responsible for the so-called phase contrast effect. Fringes are created depending on the distance between the detector and object.

Region	Distance z
Contact	$z = 0$ (pure absorption)
Near Field	$z < d^2/\lambda$
Fresnel	$z \approx d^2/\lambda$
Fraunhofer	$z > d^2/\lambda$

Table 2. 1 – Interference regions for difference distance specimen-detector (z) [95].

Table 2.1 shows the different regimes achievable, varying the distance *(z)* of the detector from the sample, where *d* is the feature size and λ the wavelength of the synchrotron radiation. Phase contrast may be exploited to improve the contrast between features with similar density or to detect narrow cracks, voids and inclusions in microstructures [16].

2.15 Advantages of using SRCT

The use of a laboratory X-ray source or a synchrotron source determines substantial differences in terms of available image quality (spatial resolution, signal to noise, beam hardening) and acquisition time (temporal resolution). The beam obtained using a laboratory device is typically polychromatic and divergent (cone beam), while the beam generated by a synchrotron source is parallel, monochromatic, coherent and orders of magnitude brighter. Therefore, the advantages associated with synchrotron radiation computed tomography are:

- High spatial resolution, which allows phenomena such as crack nucleation and resolving narrow damage to be examined.
- High temporal resolution, which is fundamental for *in situ* experiments.
- Enhancement of the signal to noise ratio due to the available flux.
- Phase-contrast effect, allowing for reliable edge detection.

Modern laboratory CT systems have narrowed the gap with the synchrotron sources, being able to achieve spatial resolution on the order of the one micrometer and below, and also allowing a degree of phase contrast, however signal to noise and scan duration remains high compromised compared to synchrotron facilities.

2.16 Concluding remarks

Toughening mechanisms in net resin have been extensively investigated in the last decades, highlighting the enhancement in terms of resistance to damage propagation associated with toughened resins. However, limited work has been carried out on toughening composites systems and consequently it is still unknown if the enhancement observed in the toughened net resin could be directly translated to a corresponding enhancement when composite materials used the same resin. In addition, the difference in behaviour between using toughened and untoughened composite systems can be also affected by other factors, such as the type of load, environmental condition (temperature and humidity). For instance, it can be possible that toughening systems perform better under quasi-static load, but do not show a real improvement under fatigue. Understanding the underpinning mechanisms associated with toughened composite systems subjected to different load conditions could provide a way to assess this. The evaluation of the effectiveness of toughening systems versus untoughened may have consequences for the damage tolerant design of structures for which durability is important, and also in the development of strategies for developing fatigue damage resistant materials.

2.17 References

[1] Bryan Harris, Ed., *Fatigue in Composites*.: CRC Press, 2003.

[2] B.D. Agarwal, L.J. Broutma, and K. Chandrashekhara, *Analysis and Performance of Fiber Composites*, Third edition ed.: Wiley.

[3] M.T. Kortschot and P.W.R. Beaumont, "Damage mechanics of composite-materials. I - Measurements of damage and strength," *Composites Science and Technology*, vol. 39, pp. 289-301, 1990.

[4] S.M. Spearing and P.W. Beaumont, "Fatigue damage mechanics of composite materials. I: Experimental measurement of damage and post-fatigue properties," *Composites Science and Technology*, vol. 44, pp. 159-168, 1992.

[5] S.M. Spearing, P.W.R. Beaumont, and M.T. Kortschot, "The fatigue damage

mechanics of notched carbon-fibre PEEK laminates," *Composites*, vol. 23, no. 5, pp. 305-311, 1992.

[6] O.J. Nixon-Pearson, S.R. Hallet, P.J. Withers, and J. Rouse, "Damage development in open-hole composite specimens in fatigue. Part 1: experimental investigation," *Composites Structures*, vol. 106, pp. 882-889, 2013.

[7] J.R. Gregory and S.M. Spearing, "Constituent and composite quasi-static and fatigue fracture experiments," *Composites Part A: Applied Science and Manufacturing*, vol. 36, pp. 665-674, 2005.

[8] S. Singh and E. Greenhalgh, "Delamination growth in epoxy-matrix composites under cyclic loading: implications for design and certifcation," in *8th European Conference on Composite Materials*, Naples, 1998.

[9] T. Adams, R. Dickson, C. Jones, H. Reiter, and B. Harris, "A power law fatigue damage model for fibre-reinforced plastic laminates," *Journal of Mechanical Engineering Science*, vol. 200, pp. 155-166, 1986.

[10] S.M. Spearing and P.W. Beaumont, "Fatigue damage mechanics of composite materials Part III: prediction of post-fatigue strength," *Composites Science and Technologies*, vol. 44, no. 4, pp. 299-307, 1992.

[11] S. Spearing and P. Beaumont, "Fatigue damage mechanisms of composite materials Part IV: Prediction of post-fatigue stiffness," *Composites Science and Technology*, vol. 44, pp. 309-317, 1992.

[12] S. Subramanian, K.L. Reifsnider, and W.W. Stichcomb, "A cumulative damage model to predict the fatigue life of composite laminates including the effect of fibre-matrix interphase," *International Journal of Fatigue*, vol. 17, no. 5, pp. 343-351, 1995.

[13] P. Paris, "Fatigue - an interdisciplinary approach," in *Proceeding of the Tenth Sagamore Conference*, New York, 1964.

[14] S.M. Spearing, P.W. Beaumont, and M.F. Ashby, "Fatigue damage mechanics of composite materials. II: a damage growth model," *Composites Science and Technology*, vol. 44, no. 2, pp. 169-177, 1992.

[15] P. Wright, X. Fu, I. Sinclair, and S.M. Spearing, "Ultra high resolution computed tomography of damage in notched carbon fiber-epoxy composites," *Journal of Composite Materials*, vol. 42, no. 19, pp. 1993-2002, 2008.

[16] A.J. Moffat, P. Wright, J-Y. Buffiere, I. Sinclair, and S.M. Spearing, "Micromechanics

of damage in 0 splits in a [90/0]s composite material using synchrotron radiation computed tomography," *Scripta Materialia*, vol. 59, pp. 1043-1046, 2008.

[17] P. Wright, A. Moffat, I. Sinclair, and S.M. Spearing, "High resolution tomographic imaging and modelling of notch tip damage in a laminated composite," *Composites Science and Technologies*, vol. 70, pp. 1444-1452, 2010.

[18] A.E. Scott, M. Mavrogordato, P. Wright, I. Sinclair, and S.M. Spearing, "In situ fibre fracture measurement in carbon-epoxy laminates using high resolution computed tomography," *Composites Science and Technologies*, vol. 71, pp. 1471-1477, 2011.

[19] R. Harrison and M. Bader, "Damage development in CFRP laminates under monotonic and cyclic loading," *Fibre Science and Technology*, vol. 18, pp. 163-180, 1983.

[20] E. Gamstedt and B. Sjogren, "Micromechanisms in tension-compression fatigue of composite laminates containing transverse plies," *Composites Science and Technology*, vol. 59, pp. 167-178, 1999.

[21] T. Yokozeki, T. Aoki, and T. Ishikawa, "Fatigue growth of matrix in transverse direction of CFRP laminates," *Composites Science and Technology*, vol. 62, pp. 1223-1229.

[22] J. Nairn, "Matrix microcraking in composites," in *Polymer Matrix Composites, Comprehensive composite materials*, J-A.E. Manson (Eds.) R. Talreja, Ed.: Elsevier Science, vol. 2, pp. 403-432.

[23] T. Vaughan and C. McCarthy, "Micromechanical modelling of the transverse damage behaviour in fibre reinforced composites," *Composites Science and Technology*, vol. 71, pp. 388-396, 2011.

[24] H. Mar and J. Daken, "Splitting initiation and propagation in notched unidirectional graphite/epoxy composites under tension-tension cyclic loading," *Composite Structures*, vol. 4, pp. 111-133, 1985.

[25] A. Garg, "0 splits initiation in fiber reinforced composites," *Engineering Fracture Mechanics*, vol. 24, pp. 255-261, 1986.

[26] D. Hull and T.W. Clyne, *An introduction to composite materials*, Second edition ed., Cambridge Solid State Science Series, Ed.: Cambridge University Press.

[27] A.C. Garg and Y-W Mai, "Failure mechanisms in toughened epoxy resins - a review," *Composites Science and Technology*, vol. 31, pp. 179-223, 1988.

[28] R.A. Pearson and A.F. Yee, "Toughening mechanisms in elastomer-modified epoxies, Part 3 The effect of cross-link density," *Journal of Materials Science*, vol. 26, pp. 2571-2580, 1989.

[29] B.U. Kang et al., "Effect of molecular weight between crosslink on the fracture behaviour of rubber-toughened epoxy adhesives," *Journal of Applied Polymer Science*, vol. 79, pp. 38-48, 2001.

[30] G. Levita, S. De Petris, A. Marchetti, and A. Lazzeri, "Crosslink density and fracture toughness of epoxy resins," *Journal of Materials Science*, vol. 26, pp. 2348-2352, 1991.

[31] R.A. Pearson and A.Y. Yee, "Toughening mechanisms in thermoplastic-modified epoxies: 1. Modification using poly (phenylene oxide)," *Polymer*, vol. 34, no. 17, pp. 3658-3670, 1993.

[32] H.R. Azimi, R.A. Pearson, and R.W. Hertzberg, "Fatigue of rubber-modified epoxies: effect of particle size and volume fraction," *Journal of Materials Science*, vol. 31, pp. 3777-3789, 1996.

[33] J. Spanoudakis and R.J. Young, "Crack propagation in a glass particle-filled epoxy resin, Part 1 Effect of particle volume fraction and size," *Journal of Materials Science*, vol. 19, pp. 473-486, 1984.

[34] A.F. Yee and R.A. Pearson, "Toughening mechanisms in elastomer-modified epoxies, Part 1 Mechanical properties," *Journal of Materials Science*, vol. 21, pp. 2462-2474, 1986.

[35] R. Bagheri, B.T. Marouf, and R.A. Pearson, "Rubber-Toughened Epoxies: a critical review," *Polymer Reviews*, vol. 49, no. 3, pp. 201-225, 2009.

[36] M.R. Groleau et al., "Mode II fracture of composites interlayered with nylon particles," *Composites Science and Technology*, vol. 56, pp. 1223-1240, 1996.

[37] R.A. Pearson and A.F. Yee, "Influence of particle size distribution on toughening mechanisms in rubber-modified epoxies," *Journal of Materials Science*, vol. 26, pp. 3828-3844, 1991.

[38] P. Dittanet and A. Pearson, "Effect of bimodal particle size distributions on the toughening mechanisms in silica nanoparticle filled epoxy resin," *Polymer*, vol. 54, pp. 1832-1845, 2013.

[39] R.P. Singh, M. Zhang, and D. Chan, "Toughening of a brittle thermosetting polymer: effect of reinforcement particle size and volume fraction," *Journal of*

Materials Science, vol. 37, pp. 781-788, 2002.

[40] J.H. Hodgkin, G.P. Simon, and R.J. Varley, "Thermoplastic toughening of epoxy resins: a critical review," vol. 9, pp. 3-10, 1998.

[41] J. He, D. Raghavan, D. Hoffman, and D. Hunston, "The influence of elastomer concentration on toughness in dispersions containing preformed acrylic elastomeric particles in an epoxy matrix," *Polymer*, vol. 40, pp. 1923-1933, 1999.

[42] L. Becu, A. Maazouz, H. Sautereau, and J.F. Gerard, "Fracture behavior of epoxy polymers modified with core-shell rubber particles," *Journal of Applied Polymer Science*, vol. 65, pp. 2419-2431, 1997.

[43] Y.L. Liang and R.A. Pearson, "The toughening mechanism in hybrid epoxy-rubber nanocomposites (HESRNs)," *Polymers*, vol. 51, pp. 4880-4890, 2010.

[44] F.F. Lange and K.C. Radford, "Fracture energy of an epoxy composite system," *Journal of Materials Science*, vol. 6, pp. 1197-1203, 1971.

[45] Y. Nakamura and M. Yamaguchi, "Effect of particle size on toughness of epoxy resin filled with angular-shaped silica," *Polymer*, vol. 32, pp. 2221-2229, 1991.

[46] S.-Y. Fu and B. Lauke, Y.-W. Mai X.-Q. Feng, "Effect of particle size, particle/matrix interface adhesion and particle loading on mechanical properties of particulate-polymer composites," *Composites: Part B*, vol. 39, pp. 934-961, 2008.

[47] Y.L. Liang and R.A. Pearson, "Toughening mechanisms in epoxy-silica nanocomposites (ESNs)," *Polymer*, vol. 50, pp. 4895-4905, 2009.

[48] M. Zamanian, M. Mortezaei, B. Salehnia, and J.E. Jam, "Fracture toughness of epoxy polymer modified with nanosilica particles: particles size effect," *Engineering Fracture Mechanics*, vol. 97, pp. 193-206, 2013.

[49] B.B. Johnsen, A.J. Kinloch, R.D. Mohammed, A.C. Taylor, and S. Sprenger, "Toughening mechanisms of nanoparticle-modified epoxy polymers," *Polymer*, vol. 48, pp. 530-541, 2007.

[50] S. Kunz-Douglass, P.W. Beaumont, and M.F. Ashby, "A model for the toughness of epoxy-rubber particulate composites," *Journal of Materials Science*, pp. 1109-1109, 1980.

[51] J. Spanoudakis and R.J. Young, "Crack propagation in a glass particle-filled epoxy resin, Part 2 Effect of particle-matrix adhesion," *Journal of Materials Science*, vol. 19, pp. 487-496, 1984.

[52] W.D. Bascom, R.Y. Ting, R.J. Moulton, C.K. Riew, and A.R. Siebert, "The fracture of an epoxy polymer containing elastomeric modifiers," *Journal of Materials Science*, vol. 16, pp. 2657-2664, 1981.

[53] R.A. Pearson and A.F. Yee, "Toughening mechanisms in elastomer-modified epoxies - Part 2 Microscopy studies," *Journal of Materials Science*, vol. 21, pp. 2475-2488, 1986.

[54] J. Kim, C. Baillie, J. Poh, and Y.-W. Mai, "Fracture toughness of CFRP with modified epoxy resin matrices," *Composites Science and Technology*, vol. 43, pp. 283-297, 1992.

[55] F. Gao, G. Jiao, and Z. Lu, "Mode II delamination and damage resistance of carbon/epoxy composite laminates interleaved with thermoplastic particles," *Journal of Composite Materials*, vol. 41, no. 1, pp. 111-123, 2007.

[56] D.J. Bull, S.M. Spearing, I. Sinclair, and L. Helfen, "Three-dimensional assessment of low velocity impact damage in particle toughened composite laminates using micro-focus X-ray computed tomography and synchrotron radiation laminography," *Composites: Part A*, vol. 52, pp. 62-69, 2013.

[57] D.J. Bull, A.E. Scott, S.M. Spearing, and I. Sinclair, "The influence of toughening-particles in CFRps on low velocity impact damage resistance performance," vol. 58, pp. 47-55, 2014.

[58] G. Borstnar, M.N. Mavrogordato, L. Helfen, I. Sinclair, and S.M. Spearing, "Interlaminar fracture micro-mechanisms in toughened carbon fibre reinforced plastics investigated via synchrotron radiation computed tomography and laminography," *Composites: Part A*, vol. 71, pp. 176-183, 2015.

[59] M. Beghini, L. Bertini, and E. Vitale, "Analysis of fatigue delamination growth in carboresin specimen with central hole," *Composite Structures*, vol. 17, no. 3, pp. 257-274, 1991.

[60] C. Scarponi and G. Briotti, "Ultrasonics technique for the evolution of delaminations on CFRP, GFRP, KFRP composite materials," *Composites Part B: Engineering*, vol. 31, no. 3, pp. 237-243, 2000.

[61] A.P. Mouritz, C. Townsend, and M.Z. Shah Khan, "Non-destructive detection of fatigue damage in thick composites by pulse-echo ultrasonics," *Composites Science and Technology*, vol. 60, no. 1, pp. 23-32, 2000.

[62] Y.A. Dzenis, "Cycle-based analysis of damage and failure in advanced composite under fatigue 1. Experimental observation of damage development within loading

cycles," *International Journal of Fatigue*, vol. 25, no. 6, pp. 499-510, 2003.

[63] S. Blassiau, A.R. Bunsell, and A. Thionnet, "Damage accumulation processes and life prediction in unidirectional composites," *Proceeding of the Royal Society A*, vol. 463, no. 2080, pp. 1135-1152, 2007.

[64] R. Gutkin et al., "On acoustic emission for failure investigation of CFRP: pattern recognition and peak frequency analyses," *Mechanical Systems and Signal Processing*, vol. 25, no. 4, pp. 1393-1407, 2011.

[65] P.F. Liu, J.K. Chu, Y.L. Liu, and J.Y. Zheng, "A study on mechanisms of carbon fiber/epoxy composite laminates using acoustic emission," *Materials and Design*, vol. 37, pp. 228-235, 2012.

[66] L. Toubal, M. Karama, and B. Lorrain, "Damage evolution and infrared thermography in woven composites laminates under fatigue loading," *International Journal of Fatigue*, vol. 28, no. 12, pp. 1867-1872, 2006.

[67] M. Pan, Y. He, G. Tian, D. Chen, and F. Luo, "Defect characterisation using pulsed eddy current thermography under transmission mode and NDT applications," *NDT & E International*, vol. 52, pp. 28-36, 2012.

[68] E. Maire and P.J. Withers, "Quantitative X-ray tomography," *International Materials Reviews*, vol. 59, pp. 1-43, 2014.

[69] E. Bayraktar, S. Antolonovich, and C. Bathias, "Multiscale study of fatigue behaviour of composite materials by X-rays computed tomography," *International Journal of Fatigue*, vol. 28, no. 10, pp. 1322-1333, 2006.

[70] J.-Y. Buffiere, E. Maire, J. Adrien, J.-P. Masse, and E. Boller, "In situ experiments with X ray tomography: an attractive tool for experimental mechanics," *Experimental Mechanics*, vol. 50, no. 3, pp. 289-305, 2010.

[71] K.H. Khor, J.-Y. Buffiere, W. Ludwig, and I. Sinclair, "High resolution X-ray tomography of micromechanisms of fatigue crack closure," *Scripta Materialia*, vol. 55, no. 1, pp. 47-50, 2006.

[72] J. Baruchel et al., "Advanced in synchrotron radiation microtomography," *Scripta Materialia*, vol. 55, no. 1, pp. 41-46, 2006.

[73] G. Requena et al., "3D-Quantification of the distribution of continuous fibres in unidirectionally reinforced composites," *Composites Part A: Applied Science and Manufacturing*, vol. 40, no. 2, pp. 152-163.

[74] P.J. Schilling, B.R. Karedla, A.K. Tatiparthi, M.A. Verges, and P.D. Herrington, "X-ray computed microtomography of internal damage in fiber reinforced polymer matrix composites," *Composites Science and Technology*, vol. 65, no. 14, pp. 2071-2078, 2005.

[75] J. Lambert, A.R. Chambers, I. Sinclair, and S.M. Spearing, "3D damage characterisation and the role of voids in the fatigue of wind turbine blade materials," *Composites Science and Technology*, vol. 72, no. 2, pp. 337-343, 2012.

[76] D.R-B. Aroush et al., "A study of fracture of unidirectional composites using in situ high-resolution synchrotron X-ray microtomography," *Composites Science and Technology*, vol. 66, no. 10, pp. 1348-1353, 2006.

[77] D.J. Bull, L. Helfen, I. Sinclair, S.M. Spearing, and T. Baumbach, "A compariosn of multi-scale 3D X-ray tomographic inspection techniques for assessing carbon fibre composite impact damage," *Composites Science and Technology*, vol. 75, pp. 55-61, 2013.

[78] D.J. Bull, S.M. Spearing, and I. Sinclair, "Observations of damage development from compression-after-impact experiments using ex situ micro-focus computed tomography," *Compsoites Science and Technology*, vol. 97, pp. 106-114, 2014.

[79] J. Hsieh, *Computed Tomography*, Secon Edition ed., SPIE Press, Ed.: Wiley Inter-Science.

[80] http://commons.wikimedia.org/wiki/File:EM_spectrum.svg

[81] Thorsten M. Buzug, *Computed Tomography*.: Springer, 2008.

[82] Willi A. Kalender, *Computed Tomography: Fundamentals, System Technology, Image Quality, Applications*, 3rd ed.: Wiley VCH, 2011.

[83] E. N. Landis and D.T. Keane, "X-ray microtomography," *Material Characterization*, vol. 61, pp. 1305-1316, 2010.

[84] A.C. Kak and M. Slaney, *Principles of Computerized Tomographic Imaging*.: IEEE Press, 1988.

[85] ImPACT 2005. http://www.impactscan.org/impactcourseslides.htm

[86] B.A. Dowd et al., "Developments in synchrotron x-ray computed tomography at the National Synchrotron Light Source," *Proc. SPIE 3372*, pp. 224-236, 1999.

[87] F. Marone and M. Stampanoni, "Regridding reconstruction algorithm for real-time tomographic imaging," *Journal of Synchrotron Radiation*, vol. 19, pp. 1029-1037,

2012.

[88] http://www.lightsources.org/what-does-light-source-look-today

[89] PSI. http://www.psi.ch/sls/accelerator#Linear_Accelerator_Linac

[90] PSI. http://www.psi.ch/info/MediaBoard/SLS_2008_e.pdf

[91] F.P. Vidal, J.M. Letang, G. Peix, and P. Cloetens, "Investigation of artefact sources in synchrotron microtomography via virtual X-ray imaging," *Nuclear Instruments and Methods in Physics Research Section B: Beam Interactions with Materials and Atoms*, vol. 234, no. 3, pp. 333-348, 2005.

[92] M. Krumm, S. Kasperl, and M. Franz, "Reducing non-linear artifacts of multi-material objects in industrial 3D computed tomography," *NDT & E international* , vol. 41, no. 4, pp. 242-251, 2008.

[93] P. Cloetens et al., "Hard x-ray phase imaging using simple propagation of a coherent synchrotron radiation beam," *Journal of Physics D: Applied Physics*, vol. 32, no. 10A, pp. 145-151, 1999.

[94] S.C. Mayo et al., "X-ray phase-contrast microscopy and microtomography ," *Optics Express*, vol. 11, no. 19, pp. 2289-2302, 2003.

[95] P.M. Wright, "Investigation of damage in laminated carbon fibre composites using high resolution computed tomography," PhD Thesis - University of Southampton, 2011.

Chapter 3

Materials and experimental procedure

This chapter contains a summary of the material systems taken into account in this study, providing an explanation of the choices made in terms of fatigue experiments and experimental scans. The materials with the conditions used have been divided into different sets, which correspond to Chapters 4-7 respectively.

The second part of this chapter describes the methodologies implemented to perform the image analyses using a range of software (VGStudio MAX, ImageJ, Matlab), and the procedures used to quantify damage. Particular emphasis is given to the explanation of the logic behind the image processing (also written codes), which provides the flexibility to use multiple software packages in sequence to achieve the final aim.

3.1 Materials

Three carbon/epoxy material systems have been assessed in the present work: two toughened systems; one containing thermoplastic toughening particles (M21/T700), the other utilizing a homogeneous, intrinsically toughened matrix (8552/IM7), along with an untoughened system (3501-6/IM7). In the appendix of this chapter the main mechanical properties for these materials are provided, see Appendix A, Tables A.1-A-3. All systems contain intermediate modulus carbon fibres, IM7 and T700. A cross-ply lay-up was used throughout, with a $[90/0]_s$ stacking sequence for the particle-toughened M21/T700 system, and a $[90/0]_{2s}$ lay-up for the other two systems. The nominal overall laminate thickness was maintained at ~1 mm for all three systems. The main difference between the two layups is the double-thickness (250 µm) of plies for the particle-toughened system compared with the other two systems, which have standard individual ply thickness (125 µm). Materials were laid up and auto-clave cured as flat plates using a standard aerospace cure cycle [1-3]; more details on curing processes for the systems used are given in the Appendix A, Figure A.1-A.3.

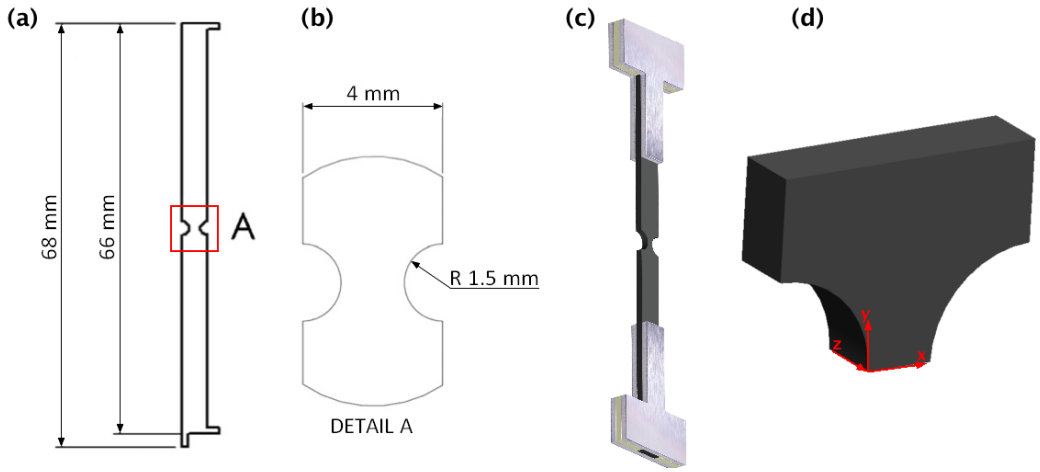

Figure 3.1 - Geometry and dimensions of the specimens (a), detail of the notch zone (b), specimen with tabs bonded (c), schematic of the region of interest considered during the scans (d).

Rectangular coupons containing two semi-circular notches of radius 1.5 mm were introduced by water jet cutting, leaving a nominal central cross-section between the

notches of 1 mm. The geometry and the dimensions of the specimens used are shown in Figure 3.1. A coupon length of 68 mm and 34 mm were selected with the requirement to fit the specimen into the compact/portable tensile and fatigue-loading device respectively to perform *in situ* experiments. Laser cut aluminium tabs were bonded to each end of specimens using standard epoxy adhesive [4]. Coupons with tabs were used for *ex situ* experiments. The use of tabs and of different specimen lengths for *in situ* and *ex situ* experiments are only related to the different loading devices employed: overall specimen length is much larger than the notched/crack growth region of interest in both cases, and is therefore not considered to affect local loading conditions.

Table 3.1 - Ultimate tensile failure strength for material systems considered [5].

Material	**UTS (MPa)**	**C_v**
M21/T700	918	0.03
8552/IM7	1271	0.12
3501-6/IM7	1419	0.07

The average ultimate tensile failure strength (UTS) for each material system has been evaluated in previous studies [5], and is calculated based on the failure load and the net cross-sectional area between the notches. Values are reported in Table 3.1, where C_v represents the coefficient of variation. The consistent tendency for the specimens to split and delaminate extensively from the notch before the final ultimate failure event (as shown in Chapter 4 and 5) justifies the use of the net section to calculate the nominal UTS.

3.1.1 Toughened particle system

The key feature of the particle-toughened system (M21/T700) is the presence of thermoplastic particles [6-8] used to increase the toughness. The nominal volume fraction of fibre is 60% [9].

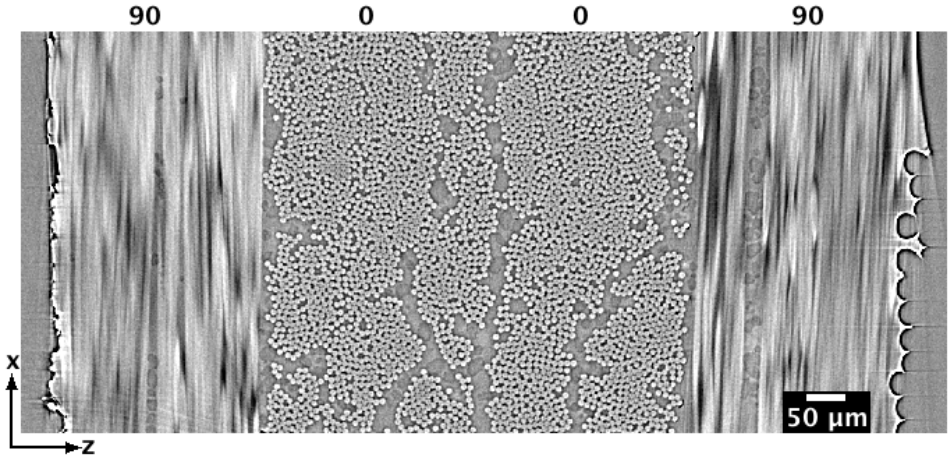

Figure 3.2 – Cross-section perpendicular to the coupon thickness of the toughening particle system.

The resulting microstructure is represented by the presence of zones with a high concentration of fibre packing, and by resin rich regions particularly in the middle of the 0˚ plies thickness, where the two plies are connected and in correspondence of the interfaces, Figure 3.2.

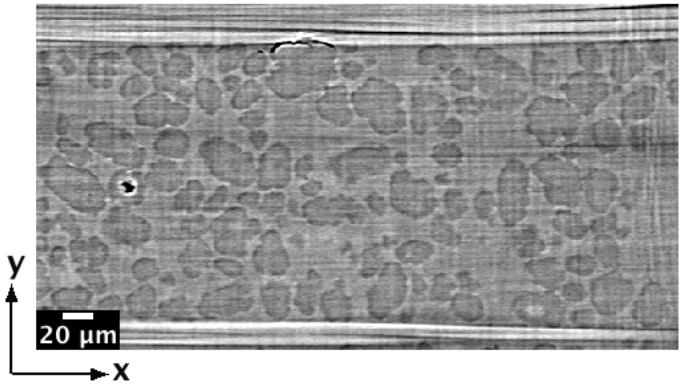

Figure 3.3 - Toughening particle in the M21/ T700 material system.

Toughening particle diameters are in the range 10-50 µm, and are in themselves heterogeneously distributed to some extent within the resin rich regions. Aspect ratios are on the order of 1-2, although there is clear variability in the exact particle shape, as shown in Figure 3.3.

3.1.2 Untoughened system

The untoughened system (3501-6/IM7) is characterised by a more uniform fibre distribution, with a total fibre volume fraction of 60%. The presence of resin rich regions is limited, as shown in Figure 3.4 where a cross section perpendicular to the loading direction is presented for the untoughened material.

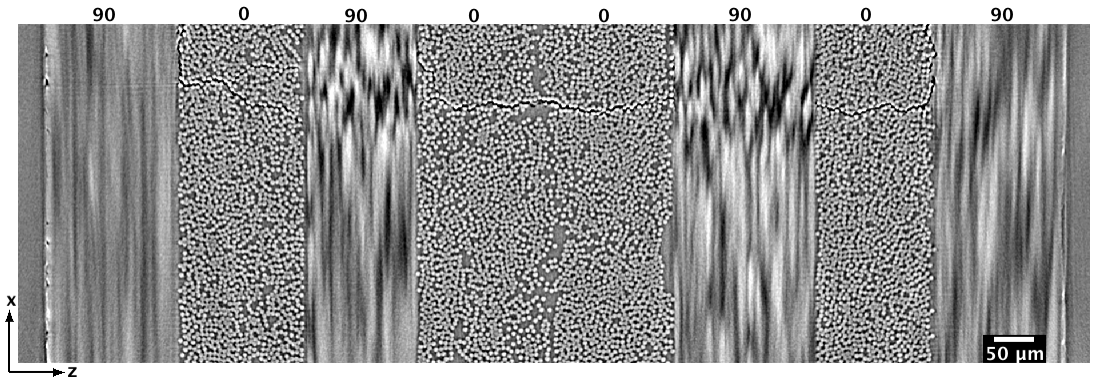

Figure 3.4 – Cross-section perpendicular to the loading direction for the untoughened system.

The relative absence of resin-rich regions is evident both within plies of same orientation (specifically at the mid-thickness of the $[90/0/90/0]_s$ layup), and between different orientations (ply interfaces), see Figure 3.4. A modest resin-rich region is perceptible in Figure 3.4, *e.g.* along the central 0/0 ply interface, but it is markedly reduced compared to the broad 'channels' of resin detected in the particle-toughened system, Figure 3.3.

3.1.3 Intrinsically toughened system

The intrinsically toughened system (8552/IM7) is characterised by a tougher resin compared to that in the untoughened material [10], with a total fibre volume fraction of 60% [10]. Figure 3.5 displays a cross-section perpendicular to the specimen thickness, wherein some resin rich regions are evident within the plies (0˚ plies in this image) and at the corresponding ply interfaces.

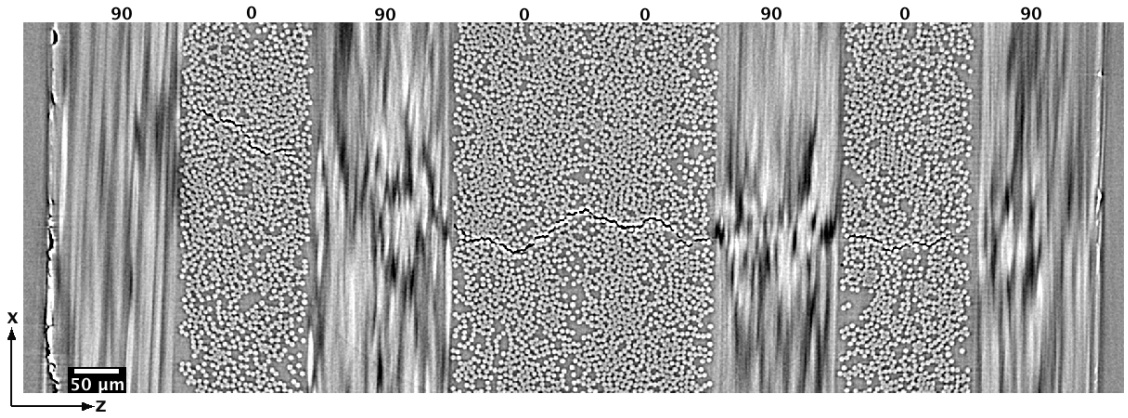

Figure 3.5 - Cross-section perpendicular to the loading direction for the intrinsically toughened material system.

The most visible difference between the untoughened and the intrinsically toughened system with the particle system is due to the difference in layup. Comparing Figure 3.2 with Figure 3.4 and Figure 3.5, the particle system consists of two external 90˚ plies and two internal 0˚ plies, therefore only two interfaces are present between plies of differing orientation. In contrast, the $(90/0)_{2s}$ lay up used in the other two systems results in six ply interfaces.

3.2 Load frame for *in situ* quasi-static loading

A simple tensile stage was designed and used in previous work by Wright *et al*. [11] with the aim to perform *in situ* SRCT tensile tests within the constraints imposed by the limited space and weight. The maximum weight allowed by SRCT sample holder base table is of 2 kg [12], while the tensile rig used is less than 2 kg, Figure 3.6. The same load frame was employed in the present work to load pre-fatigue specimens (in tension) during the time that scans were performed. The ability to scan specimens with an applied load is important as it allows parameters such as crack opening displacement and crack shear displacement to be quantified with higher accuracy. The load is applied using a screw driven mechanism at the top of the rig that applies a linear displacement to the upper loading point. The load is transferred to the specimen by the aluminium tabs, which are connected with the top and bottom loading point "fingers" as shown in Figure 3.6.

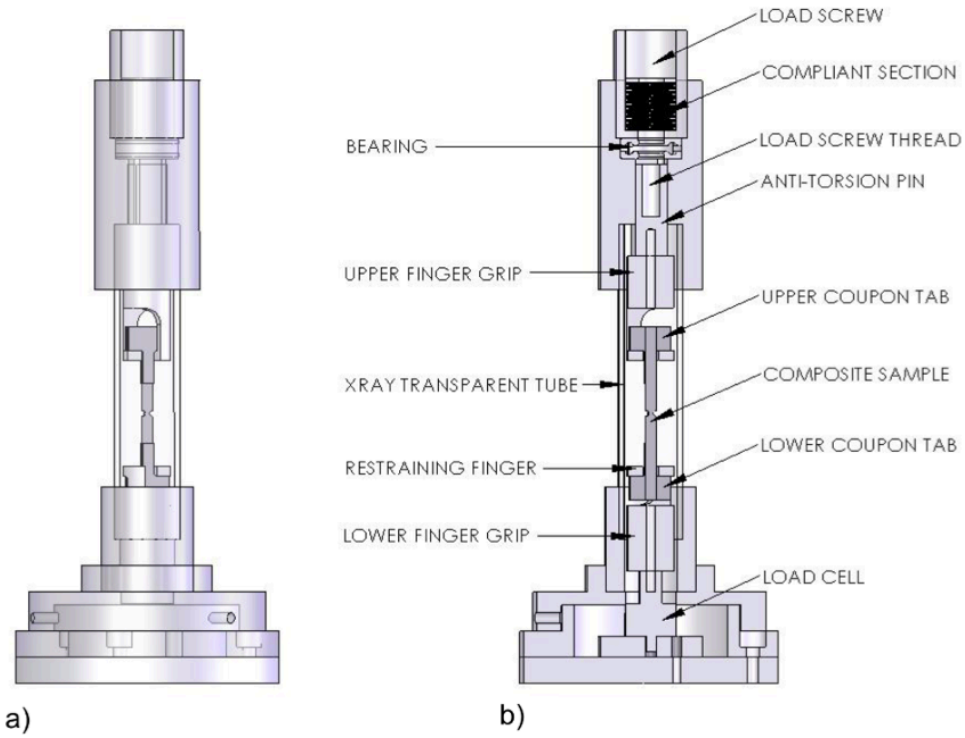

Figure 3.6 - Schematic of load frame used to load pre-fatigue specimens, (a); annotated cross section (b) [11].

Any torsion is avoided via use of a square section bolt and corresponding square-section keyway, ensuring that only uniaxial loads are applied. To reduce the effect of stress relaxation due to the visco-elastic properties of the tube and/or thermal expansion changes, a compliant section made using disc springs was included, which improves the stability of the load with time. In the present work, loads considered were found to be stable within 1% over the typical 10 minutes settings/scan duration. The system is able to apply tensile loads up to 1 kN. Independent calibration of the small internal load cell was carried out using a standard Instron universal test machine.

3.3 Load frame for *in situ* fatigue experiments

In situ SRCT fatigue experiments have been performed using a compact load device manufactured by Deben Ltd [13], Figure 3.7. This system allows for the application of tensile, compression and fatigue loads up to a maximum load of 5 kN. Some modifications to the original version were applied to reduce the weight of the

structure, in order to be suitable for the tomographic stage, and to centre the mass, which was initially asymmetrical. Modifications were also made to allow for more rapid specimen exchange. The final version achieved is shown in Figure 3.7.

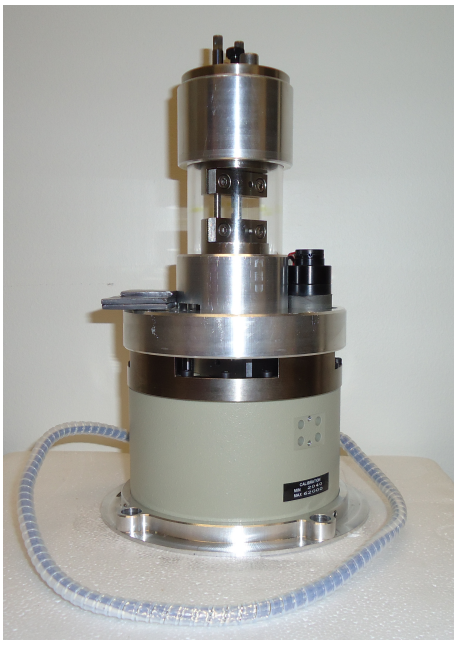

Figure 3.7 - *In situ* compact loading device for tension, compression and fatigue experiments [13], the modified version for current SRCT fatigue testing.

The gauge length allowable between the grips was between 12.3 and 22 mm. Consistent with this, specimens were cut to a total length of 34 mm, allowing > 5 mm of specimen at each end for clamping in the simple bolt-loaded grips. This was found to be sufficient and stable (no slipping detected) for the loads used in the present work.

3.4 Experimental procedure

Five different categories of experiment were conducted within the overall experimental programme. Fatigue loading conditions and scan procedures were different according to the particular objectives of each set of experiments. Details are described in the following sub-sections, with the results presented in Chapters 4 to 7. In particular, *set 1* and *set 2* are referred to Chapter 4, *set 3* to Chapter 5, *set 4* to Chapter 6, and *set 5* to Chapter 7.

Set 1: Damage initiation

The main aim of these experiments was to observe the early stages of damage initiation for the particle-toughened system (M21/T700) in both fatigue and quasi-static cases. Therefore, the peak load considered was relatively low: 30% UTS for the fatigue case and 35% UTS for the tensile condition. For the fatigue case, only 200 cycles were applied at a frequency of 5 Hz, with an R-ratio=0.1 using a standard servo-hydraulic load frame. Pre-fatigued coupons were loaded using the simple tensile load rig (described in the section 3.2), up to 90% of the cyclic load peak considered. This allowed the opening of the crack to be visualised, avoiding at the same time further damage propagation. In a similar way *in situ* quasi-static tensile tests were performed. Specimens were scanned in the loaded state at the Swiss Light Source (on the TOMCAT-X02DA Beamline, Paul Scherrer Institut, Villigen, Switzerland). The distance between specimen and detector for these experiments was set to provide a degree of phase contrast (~22 mm), without undue streaking artefacts. The beam energy was 14 keV, and the isotropic voxel resolution was 0.325 μm, consistent with capturing the early stages of damage initiation at high resolution.

Set 2: Fatigue micromechanisms

Tensile fatigue tests with a peak load of 30% and 50% of nominal UTS were performed using a load ratio of R=0.1 for the particle-toughened system (M21/T700). Experiments were conducted at 10 Hz, up to 10^4 cycles using a standard servo-hydraulic load frame. The pre-fatigue coupons were loaded (~90% of peak) in the tensile device during the scan to enable opening of the crack. Comparable quasi-static tests had been previously performed as part of an earlier study [5]. Results of the quasi-static tests were chosen for comparison to the present tests such that crack lengths (particularly 0˚ ply split cracks) were comparable to those achieved in the fatigue case. The required tensile loads applied were correspondingly in the order of 60 to 70% of UTS, significantly higher than those used for fatigue.

The voxel resolution chosen for the pre-fatigued coupons was 1.5 μm, which represents a good trade-off between the resolution required to measure crack opening displacements and the optimum field of view; ideally keeping all of the crack length inside the field of view, and avoiding the need to stitch together multiple volumes. The

pre-fatigued coupons were scanned at the Swiss Light Source (on the TOMCAT-X02DA Beamline, Paul Scherrer Institut, Villigen, Switzerland) using beam energy of 19 keV and a propagation distance of 30 mm.

The tensile specimens had been previously scanned [14] at the ESRF (on the ID19 Beamline, European Synchrotron Radiation Facility, Grenoble, France) employing beam energy of 20 keV and a propagation distance of 37 mm [5,11]. The voxel resolution used was similar to fatigue tests, and equal to 1.4 µm.

Set 3: Toughening processes

All the material systems described in the Section 3.1 were considered in this evaluation, toughened and untoughened systems. Fatigue cycling was initially carried out at a frequency of 5 Hz with a peak load of 50% UTS and R=0.1 using a standard servo-hydraulic load frame up to 700 load cycles. After the pre-cycling had been applied, each specimen was placed in the *in situ* load frame, a load less than the corresponding maximum peak load (~90% of peak) was applied to open the crack, and the coupon was scanned. Following these initial scans, the *in situ* load frame was used to apply an additional 100 full load cycles, and then the specimens were imaged again while under load. A voxel resolution of 0.69 µm was used. For the particular micromechanistic focus of this work, the high resolution used and the full-field imaging afforded by SRCT allowed detailed observations to be made with relatively few cycles applied. *In situ* fatigue tests were performed at the Swiss Light Source (on the TOMCAT-X02DA Beamline, Paul Scherrer Institut, Villigen, Switzerland) using beam energy of 19 keV and a propagation distance of ~22 mm.

Set 4: Fibre failure

Both fatigue and tensile tests were assessed to evaluate the mechanisms of fibre fracture in the particle-toughened system (M21/T700). The experimental conditions investigated are reported in Table 3.2. A combination of *ex situ* and *in situ* fatigue experiments were considered. In particular, the *ex situ* tests were used to monitor the accumulation of fibre breaks for different loads and number of cycles. The volume of the coupons scanned (fibre length of ~3 mm starting from the middle of the notch) was maintained the same between these cases, as also the voxel resolution (1.6 µm).

The *in situ* experiments had the aim to understand the micromechanisms of fibre failure, and for this reason were conducted at higher resolution (0.69 µm). Consequently, the field of view achieved in these last cases was smaller compared with the *ex situ* scans. However, the number of breaks detected in the *in situ* volumes were not compared with those observed in the *ex situ* volumes for the aforementioned reason (different volumes and consequently different fibre sampling lengths/volumes), but were used for the assessment of fibre failure micromechanisms.

Table 3. 2 - Experimental tests used for fibre failure assessment in the particle-toughened system.

%UTS (Peak load)	N (Cycles)	Type of test	Voxel resolution (µm)
50	700	*In situ*	0.69
50	800	*In situ*	0.69
30	10^6	*Ex situ*	1.6
50	10^3	*Ex situ*	1.6
50	10^5	*Ex situ*	1.6
70	10^3	*Ex situ*	1.6
80	1	*In situ*	1.4

All the fatigued specimens were scanned while applying a pre-load less than the maximum peak used during cycling, whereas the tensile tests [14] were scanned at the same time that the load was applied using the tensile loading rig. The voxel resolution used is reported in the Table 3.2 for the different cases considered. Fatigue experiments were performed at the Swiss Light Source (on the TOMCAT-X02DA Beamline, Paul Scherrer Institut, Villigen, Switzerland) using a beam energy of 19 keV and a propagation distance of ~22 mm. Quasi-static tests and scans of the same material system, were performed at the ESRF, ID19 Beamline, European Synchrotron Radiation Facility, Grenoble, France; employing beam energy of 20 keV and a propagation distance of 37 mm, and were conducted during previous work [14]. One of these scans (80% UTS) was used in this study to compare the fatigue behaviour with the quasi-static case, reported in the Table 3.2 with a number of cycles equal to 1. The comparison was conducted ensuring that the location and the fibre length in the quasi-static case were similar to the fatigue cases.

Set 5: Damage quantification

Ex situ fatigue tests were used to quantify the damage propagation (0˚ ply splits) in the particle-toughened system (M21/T700) in terms of crack opening displacement and crack shear displacement. In the cases considered, different load levels and number of cycles were applied, as shown in Table 3.3. The influences of the peak load, number of cycles, crack length, and damage modes interaction on the crack opening and shear displacement were evaluated. All the scans have been performed in a loaded state (~90% of maximum fatigue peak load) at the Swiss Light Source (on the TOMCAT-X02DA Beamline, Paul Scherrer Institut, Villigen, Switzerland) using beam energy of 19 keV and a propagation distance of ~22 mm.

Table 3. 3 - Experimental tests used to quantify fatigue damage in the particle-toughened system.

%UTS (Peak load)	N (Cycles)
30	10^6
50	10^3
50	10^5
70	10^3

The voxel resolution chosen was 1.6 μm, which represents a good trade-off between the resolution required to measure crack opening displacements and the field of view achievable. However, high peak loads and/or high number of cycles involve in long 0˚ ply splits, which exceed the field of view of a single scan. In this contest, multiple scans were performed and concatenated to ensure that all the damage is included in the scans. This procedure is described in the Section 3.6.1.

3.5 SRCT procedure

As noted above, two synchrotron radiation facilities were used: Swiss Light Source (TOMCAT-X02DA Beamline, Paul Scherrer Institut), and ESRF (ID19 Beamline, European Synchrotron Radiation Facility). This latter was exploited in previous study [5] to

perform tensile tests. However, some of these coupons, and the previously obtained data, were also utilised to provide a comparison with the fatigue cases.

During each tomographic scan performed at SLS, 1500 projections were collected on a 2560 x 2160 pixel detector, through a rotation of 180˚. The exposure time for each radiograph was 150 ms, resulting in a total scan time of approximately 4 minutes. Previous study [5] has shown that repeat scanning under these conditions did not affect failure processes (due to photon density flux). Figure 3.8 shows the SRCT configuration with the *in situ* loading device in place. Projections obtained from the scans were reconstructed using an in-house code based on the GRIDREC/FFT approach [15].

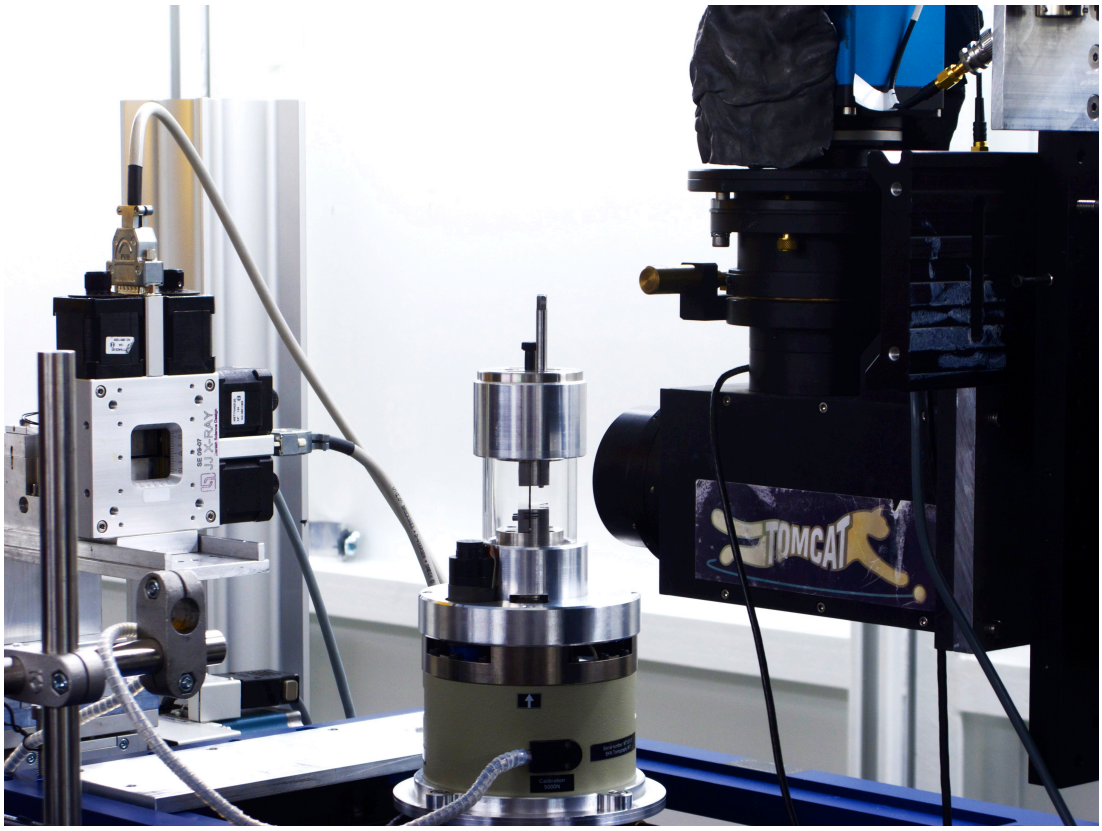

Figure 3.8 - Scan setup used for the *in situ* experiments at the TOMCAT-X02DA beamline, SLS.

3.6 Data processing

In this section a brief description of the techniques and tools used for image analysis is provided. Image analysis is a key to obtaining and interpreting the results presented in the Chapter 4-7.

3.6.1 Volume concatenation

The requirement to include all damage at specific high resolutions was addressed using multiple scans, and concatenating them during post-processing (stitching). Volume registration to achieve stitching is not trivial, considering all the degrees of freedom that each volume can have in 3D. In order to simplify this problem and to increase the accuracy of the overlap between concatenated volumes, only a translation along the loading direction was allow during the scan, locking all the remaining degrees of freedom. This choice is consistent with the fact that the splits, the primary objects of this study, propagate from the notch parallel to the loading direction, corresponding with the direction perpendicular to the beam.

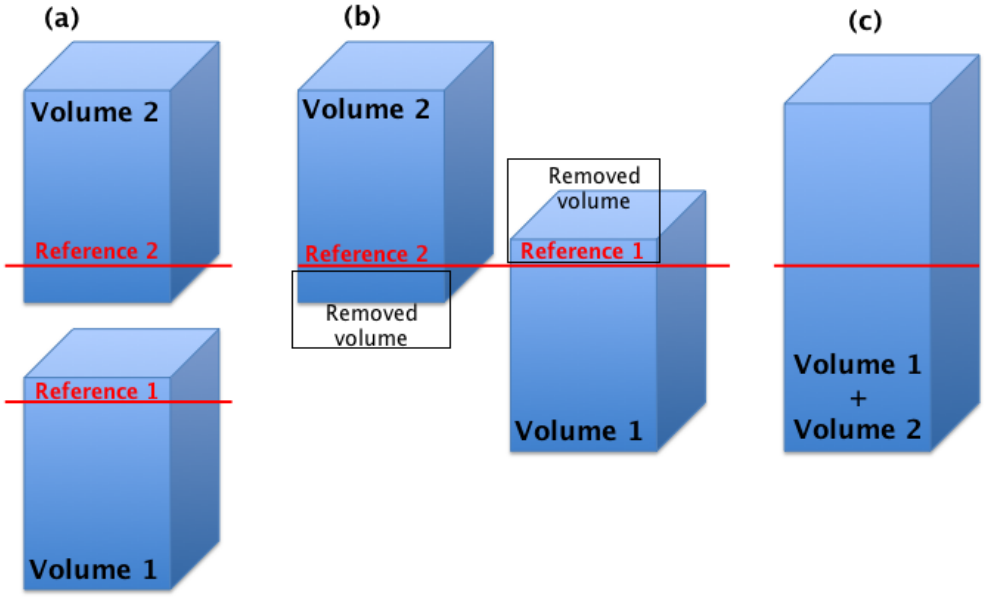

Figure 3. 9 – Schematisation of the concatenation procedure between two adjacent volumes: (a) find the reference slide in the direction along the scan translation (loading direction) for both volumes, (b) removing the overlapping regions, (c) concatenation of the volumes obtained in (b).

The procedure followed was: (1) perform the first scan, at one end (usually near the notch root) of the region of interest desired; (2) translate the field of view along the loading direction keeping an overlapped volume between the first and the second scan; (3) repeat until the entire crack/damage region is covered. The overlapped volume between two consecutives scans is very important to allow subsequent concatenation of the scans. This process involves finding similar features (by eye) in the two volumes, along the plane perpendicular to the loading direction (and thus the axis of the imaging translation). The final aim is to perfectly register the two adjacent image volumes. Using software such as ImageJ™ it is possible to duplicate each single volume, excluding the overlapped region and then concatenate them. Figure 3.9 provides a schematisation of the procedure of concatenation followed between two consecutive volumes, while a flow chart description is reported in the Appendix A.4. The process is iterative until all the scans are merged into a single volume. Up to six concatenated volumes were used in this work. This highest number was required for a crack length of roughly 9 mm. This resulted in a raw data file size of ~70 GB, which of itself results in challenges of data handling and processing speed.

3.6.2 Segmentation

Segmentation is a process, which consists of dividing an image volume into sub-volumes, usually to separate/isolate key features (*e.g.* damage or microstructure), allowing subsequent three-dimensional visualization and quantification. A convenient method to achieve this, implemented in the VGStudio Max™ 2.1 software [16] and used in the present work, is the seed-growing algorithm [17,18]. A global grey-scale threshold value can be used to identify the surfaces of objects/feature, but this usually causes geometric errors due to the variation in the local threshold at the surface. Instead, region growing is an image processing technique that segments all voxels connected to a seed point, which are within a defined grey-scale tolerance, defined by the user. Defining the effective spatial resolution of a given CT image is a non-trivial issue [19]. Work by Bull *et al.* [20] and Guvenilir *et al.* [21] note the ability to exploit the so-called 'partial volume' effect to extend the resolution of crack opening measurements to sub-voxel level. This is particularly useful when working at lower

resolutions and in the absence of phase contrast to define surfaces. In the present work, with high-resolution synchrotron images, sub-voxel estimation has not been carried out, although a consistent method of estimating and comparing crack opening between samples has been adopted, with typical results illustrated in Figure 3.10. Reconstructed data was analysed essentially as raw form, without additional post-processing (de-noising, edge enhancement, *e.g.* median filtration), avoiding to introduce any modifications.

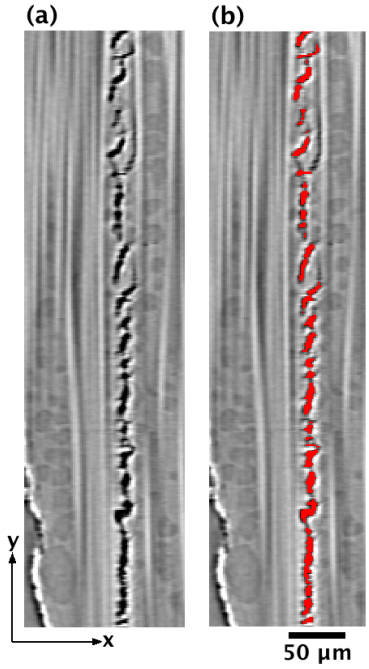

Figure 3.10 - Cross-section of a 0˚ ply split for the load of 30% UTS and 10^4 cycles: (a) original greyscale image, (b) corresponding crack/damage segmentation (in red).

In most of the cases considered achieving segmentation required a semi-automatic procedure, shown schematically in Appendix A.5. The procedure ends when all the voxels that describe the crack are included in a new region of interest (ROI), which represents the segmented crack. In detail, considering a specific crack visualized using VGStudio Max 2.1, the first step consists of identifying the crack and defining a region of interest (ROI) around it (in a 2D plane as shown in Figure 3.11(a)); the second step is to extend the ROI around the crack in 3D (*i.e.* perpendicular to the plane chosen initially). This process has the objective of restricting the region where the seed-growing algorithm is applied and consequently reduces the computational time. The

application of the seed growing tools is an iterative process in 3D, and the final result is a region of interest containing only the crack, Figure 3.11(b).

In all cases the resulting segmentation was checked by eye, scrolling through all the slices and adding regions missed and/or removing uncracked zones. However, the segmentation procedure is not straightforward for all situations, and it is strictly affected by imaging properties, such as signal-to-noise ratio, image contrast, and voxel resolution.

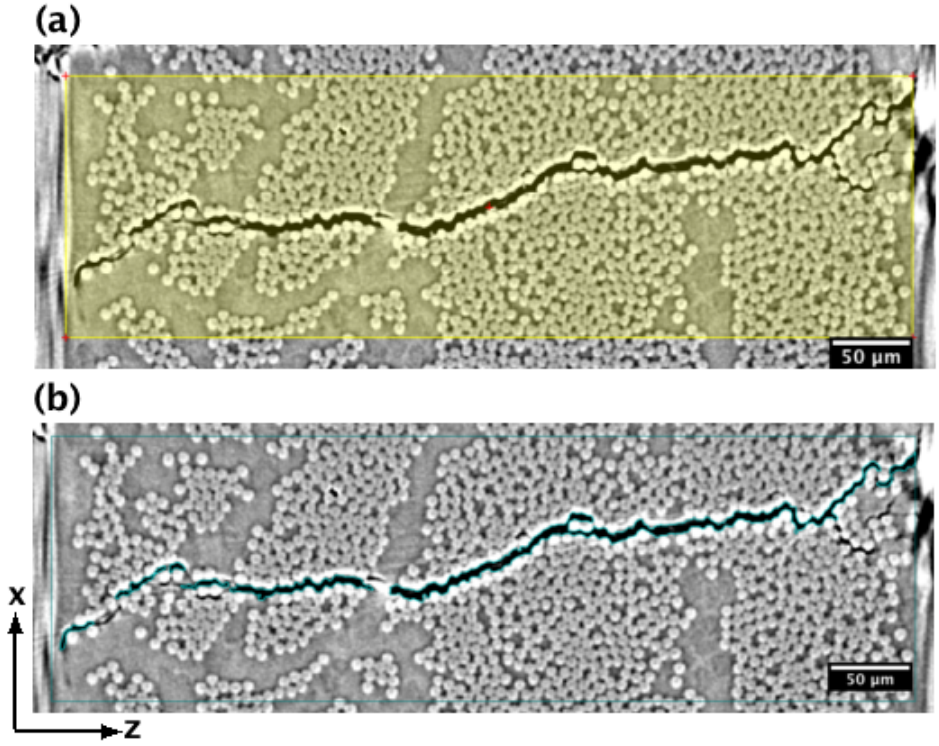

Figure 3.11 – Segmentation process: defining a region of interest (a), applying the seed-growing algorithm in the aforementioned region (b).

Consequently, it may result in a time consuming process, particularly when the crack is discontinuous or when the crack opening is high, due to the fact that this latter case may exhibit a wider range of greyscale associated with the damage, as illustrated in Figure 3.12 for a more open ((Figure 3.12(a)) versus a narrow crack ((Figure 3.12(b)) within the same specimen. The greyscale plots associated with lines A and B through the two cracks considered display a constant value (equal to zero, black region) for the narrow crack, Figure 3.12(b); while a wider range is found (0-150) for the more open

crack, Figure 3.12(a). The range in greyscale within the more open crack is directly attributable to the edge detection conditions being used (near-field Fresnel). In turn the wider range of greyscale generally requires more iteration using the seed-growing algorithm to obtain a complete segmentation. When segmentation of the feature of interest (*i.e.* the crack in this specific case) is completed, it is possible to extract the segmented damage as a separate volume in order to produce the three-dimensional visualization. Furthermore, setting the material as semi-transparent and colouring the damage by type, it is possible to visualise the three-dimensional rendering of the different components of damage inside the specimen.

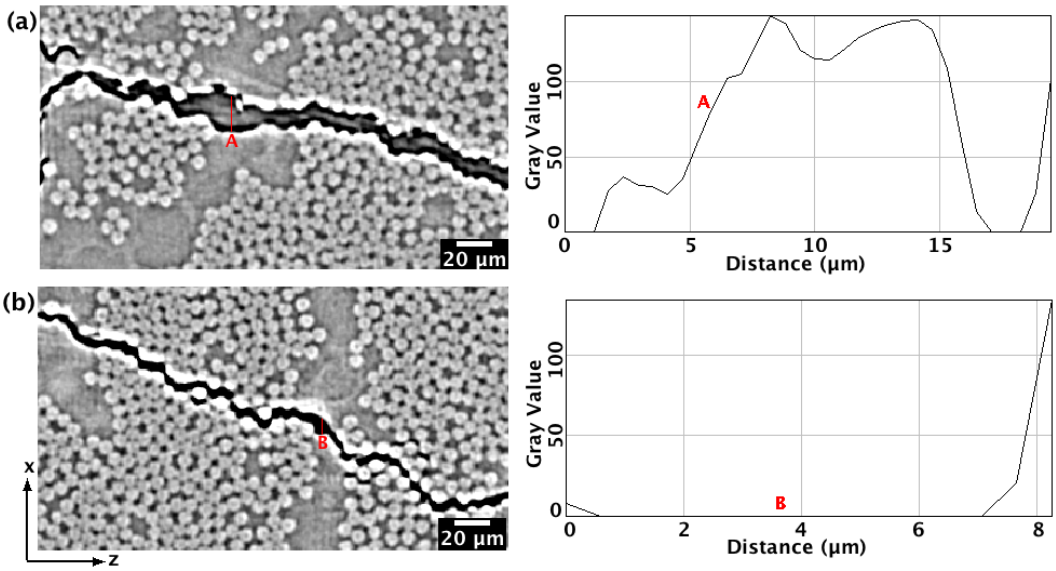

Figure 3.12- Greyscale value along the line across the crack: A for a wide opening (a), B for a narrow crack (b).

3.6.3 Crack opening displacement procedure

Following the methodology identified by Moffat *et al.* [22] damage quantification of cracks was performed via crack opening displacement measurement using a Matlab code that takes as input the binary volume of the crack, and plots as output the colour map of the crack opening displacements. The overall procedure is schematized in Figure 3.13, and a flow chart for the procedure followed is reported in the Appendix A.6. Cracks were carefully segmented (as described in section 3.6.2) and exported as new binary volumes for subsequent processing in ImageJ™, for which a macro was

written [5] and applied. This draws a rectangle with dimensions of one pixel wide by the height of the 2-D image slice considered. Crack opening displacement within this rectangle is calculated as the mean greyscale value multiplied by the height of the rectangle and then divided by 255 (maximum value that a pixel may assume in a binary image). The rectangle covers all the image width (pixel by pixel) and the results obtained (COD in pixel) are written in a text file. The process is iterative and terminates when all the slices of the volume are analysed.

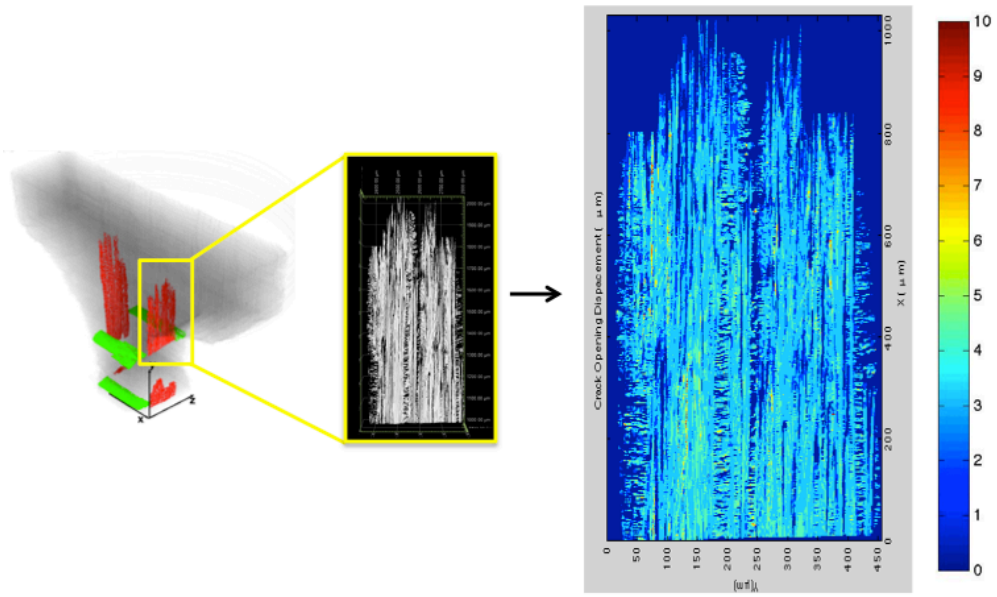

Figure 3.13 - Procedure followed to generate Crack Opening Displacement maps.

A Matlab code was written to import the text file provided by ImageJ™. The values of crack opening displacement in output from ImageJ™ were converted into μm, multiplying the value in pixels by the voxel size, and represented as colour map, see Figure 3.13. Three-dimensional damage rendering demonstrates that 0˚ ply splits are not planar [11]; however, the COD map represents a 2D projection of the split onto the plane of the 0˚ plies, obtained by summing the voxels in the crack-thickness direction.

3.6.4 Crack shear displacement procedure

Crack shear displacements (CSD) associated with the 0˚ ply splits have been evaluated following the methodology of Toda *et al.* [23] using the occasional fibre breaks along

the 0˚ ply splits as reference features, as shown in Figure 3.14(a). CSD was obtained by measuring the relative displacements parallel to the fibre direction between pairs of fibre breaks on opposite faces of the split, Figure 3.14(b). The relatively infrequency of such breaks does not support such 'full-field' representation as achieved for the COD, especially for a combination of load/number of cycles that shows relatively low number of fibre breaks.

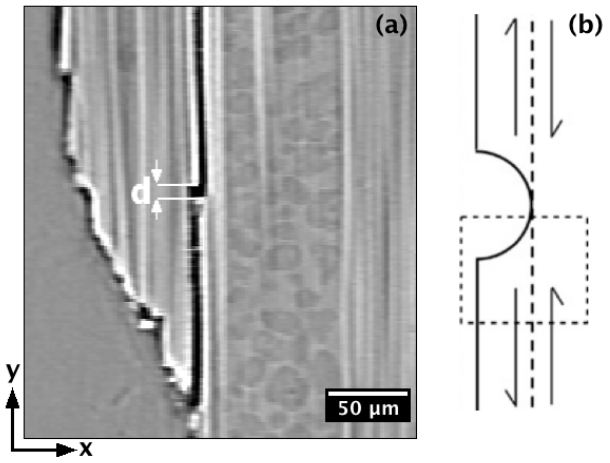

Figure 3.14 - Crack shear displacement evaluation: fibre breaks as reference features (a), and (b) schematic representation of the shear strains that develop in correspondence of 0˚ split.

3.6.5 Crack front profile and variation

The crack profile of the 0˚ ply splits was evaluated using a Matlab routine, which takes as input the COD map data, represented by a matrix in Matlab, where the uncracked material is represented by zero and the other values are the COD values. The routine evaluates the last pixel different from zero along the crack length for each pixel across the split width. The resulting plot is the crack-front profile, *i.e.* Figure 3.15(a). Based on these values, the red line represented in Figure 3.15(a) was taken as a reference line from which the other measurements were taken. The new reference (red line) was defined as the minimum value showed from the crack profile through the 0˚ ply split width. The variation of the profile has been calculated as the root mean square value across the split width, Figure 3.15(b).

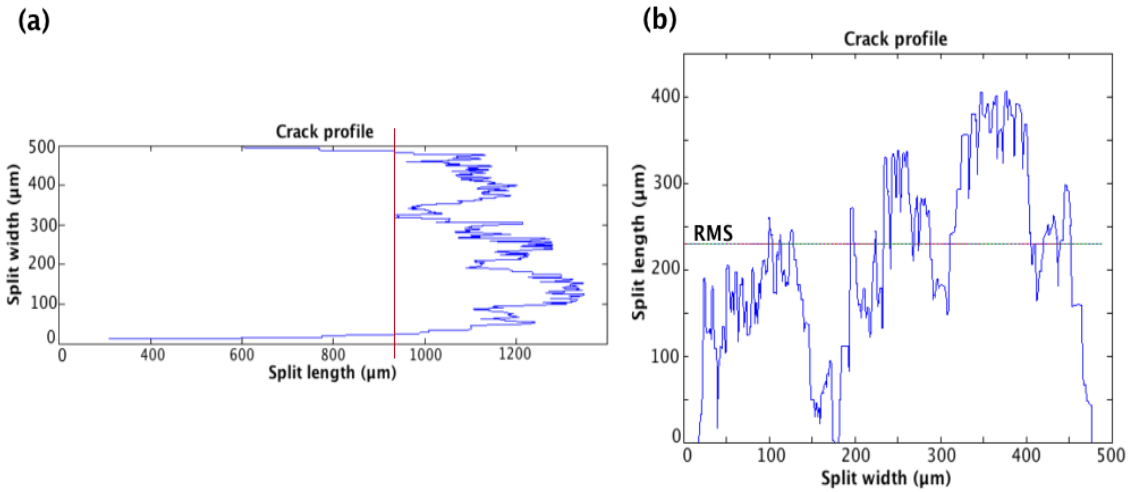

Figure 3.15 – Crack front profile shape (a), and the measurement of its variation (b).

3.7 Accuracy of the measurements

The accuracy of the measurements obtained (COD, CSD) is related to the voxel resolution, which represents the smallest value measurable (in the absence of partial-volume estimates). In other words we can say that is not possible to achieve accurate COD values in the interval between zero and the voxel resolution. The partial volume effect occurs when two phases with different density are presented within a single voxel. The direct consequence is an averaging of the attenuation coefficient for the considered voxel, often assumed to be a simple linear weighting by the relative fill of each phase present in a given voxel (e.g. see [21]). Clearly, lower resolutions may involve in higher inaccuracies due to this effect. Bull *et al*. [20] considered the effect of partial volume on the evaluation of COD using microfocus scans with a voxel resolution of 4.3 µm, and compared results obtained with the CODs associated to synchrotron computed tomography (voxel resolution 1.4 µm) of the same volumes. They found that microfocus scanning overestimated COD by up to three times without consideration of partial volume effects. The use of the partial volume correction on microfocus provided COD values in agreement with those detected by synchrotron tomography [20].

3.8 References

[1] Hexcel. www.hexcel.com/Resources/DataSheets/Prepreg-Data-Sheets/M21_global.pdf

[2] Hexcel. http://www.hexcel.com/Resources/DataSheets/Prepreg-Data-Sheets/8552_eu.pdf

[3] Hexcel. http://www.hexcel.com/Resources/DataSheets/Prepreg-Data-Sheets/3501-6_eu.pdf

[4] Devcon. http://www.itw-devcon.co.uk/images/uploads/tds/Devweld_531.pdf

[5] P.M. Wright, "Investigation of damage in laminated carbon fibre composites using high resolution computed tomography," PhD Thesis - University of Southampton, 2011.

[6] R.A. Pearson and A.Y. Yee, "Toughening mechanisms in thermoplastic-modified epoxies: 1. Modification using poly(phenylene oxide)," *Polymer*, vol. 34, no. 17, pp. 3658-3670, 1993.

[7] J.H. Hodgkin, G.P. Simon, and R.J. Varley, "Thermoplastic toughening of epoxy resins: a critical review," *Journal of Materials Science*, vol. 9, pp. 3-10, 1998.

[8] A.J. Kinloch, M.L. Yuen, and S.D. Jekins, "Thermoplastic-toughened epoxy polymers," *Journal of Materials Science*, vol. 29, pp. 3781-3790, 1994.

[9] A.E. Scott, M. Mavrogordato, P. Wright, I. Sinclair, and S.M. Spearing, "In situ fibre fracture measurement in carbon-epoxy laminates using high resolution computed tomography," *Composites Science and Technologies*, vol. 71, pp. 1471-1477, 2011.

[10] A.S. Kaddour, M.J. Hinton, P.A. Smith, and S. Li, "Mechanical properties and details of composite laminates for the test cases used in the third world-wide failure exercise," *Journal of Composite Materials*, vol. 47, pp. 2427-2442, 2013.

[11] P. Wright, A. Moffat, I. Sinclair, and S.M. Spearing, "High resolution tomographic imaging and modelling of notch tip damage in a laminated composite," *Composites Science and Technologies*, vol. 70, pp. 1444-1452, 2010.

[12] PSI. http://www.psi.ch/sls/tomcat/Station1_IntroEN/sample_holder_specs2.pdf

[13] Deben. http://deben.co.uk/products/µxct-in-situ-holders-testing-stages/tensile-

stages-for-x-ray-ct-tomography/

[14] P. Wright and M.N. Mavrogordato, Private Communications, 2009, Data from European Synchrotron Radiation Facility.

[15] B.A. Dowd et al., "Developments in synchrotron x-ray computed tomography at the National Synchrotron Light Source," *Proc. SPIE 3372*, pp. 224-236, 1999.

[16] VGStudio Max. Volume Graphics. http://www.volumegraphics.com/en/

[17] R. Adams and L. Bischof, "Seed region growing," *IEEE Tansactions on Patter Analysis and Machine Intelligence*, vol. 16, no. 6, pp. 641-647, 1994.

[18] J. Fan, G. Zeng, M. Body, and M.-S. Hacid, "Seed region growing: an extensive and comparative study," *Pattern Recognition Letters*, vol. 26, pp. 1139-1156, 2005.

[19] ASTM E1441, Standard Guide for Computed Tomography (CT) Imaging, 2005.

[20] D.J. Bull, I. Sinclair, and S.M. Spearing, "Partial volume correction for approximating crack opening displacements in CFRP material obtained from micro-focus X-ray CT scans," *Composites Science and Technology*, vol. 81, pp. 9-16, 2013.

[21] A. Guvenilir, T.M. Breunig, J.H. Kinney, and S.R. Stock, "Direct observation of crack opening as a function of applied load in the interior of a notched tensile sample of Al-Li 2090," *Acta Materialia*, vol. 45, no. 5, pp. 1977-1987, 1997.

[22] A.J. Moffat, P. Wright, J-Y. Buffiere, I. Sinclair, and S.M. Spearing, "Micromechanics of damage in 0 splits in a [90/0]s composite material using synchrotron radiation computed tomography," *Scripta Materialia*, vol. 59, pp. 1043-1046, 2008.

[23] H. Toda et al., "A 3D measurement procedure for internal local crack driving forces via synchrotron X-ray microtomography," *Acta Materialia*, vol. 52, no. 5, pp. 1305-1317, 2004.

[24] A. Moffat, "In situ calibration of cohesive zone models for composite damage," University of Southampton, Handover report 2007.

[25] Q.D. Yang et al., "On the crack initiation in notched, cross-plied polymer matrix composites," *Journal of Mechanics and Physics of Solids*, vol. 78, pp. 314-332, 2015.

[26] E.J. Barbero, *Introduction to Composite Materials Design*, Second Edition ed.: CRC Press, 2010.

Appendix A

Table A. 1- Mechanical properties of unidirectional M21/T700 [5,24].

E_1 (GPa)	E_2 (GPa)	G_{12} (GPa)	ν_{12}	σ_{1ten} (MPa)	σ_{1comp} (MPa)	σ_{2ten} (MPa)	σ_{2comp} (MPa)	σ_{12} (MPa)	$\alpha_1 (K^{-1})$	$\alpha_2 (K^{-1})$
148	7.8	3.8	0.35	2200	1280	75	250	95	$-1e^{-6}$	$34\ e^{-6}$

Table A. 2 – Mechanical properties of unidirectional 3501-6/IM7 [10,25,26].

E_1 (GPa)	E_2 (GPa)	G_{12} (GPa)	ν_{12}	σ_{1ten} (MPa)	σ_{1comp} (MPa)	σ_{2ten} (MPa)	σ_{2comp} (MPa)	σ_{12} (MPa)	$\alpha_1 (K^{-1})$	$\alpha_2 (K^{-1})$
142	10.3	7.2	0.27	2280	1480	57	200	72	$-1e^{-6}$	$26\ e^{-6}$

Table A. 3 – Mechanical properties of unidirectional 8552/IM7 [10].

E_1 (GPa)	E_2 (GPa)	G_{12} (GPa)	ν_{12}	σ_{1ten} (MPa)	σ_{1comp} (MPa)	σ_{2ten} (MPa)	σ_{2comp} (MPa)	σ_{12} (MPa)	$\alpha_1 (K^{-1})$	$\alpha_2 (K^{-1})$
165	9	5.6	0.34	2560	1590	73	185	90	$-1e^{-6}$	$18\ e^{-6}$

Figure A. 1 - Schematic process of the curing conditions for HexPly M21 for parts with a thickness less than 15 mm [1].

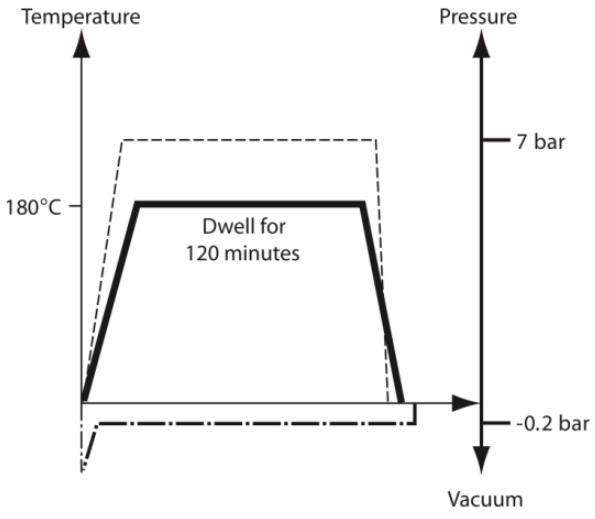

Figure A. 2 - Schematic process of the cure cycle for 3501-6 Epoxy matrix [3].

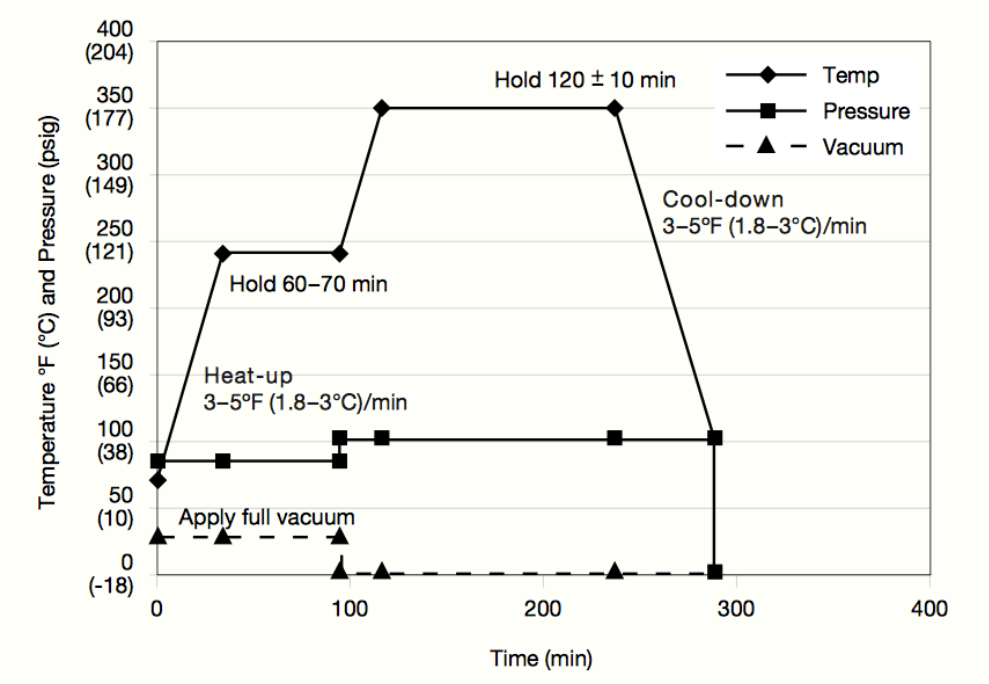

Figure A. 3 - - Schematic of the curing cycle for the HexPly 8552 [2].

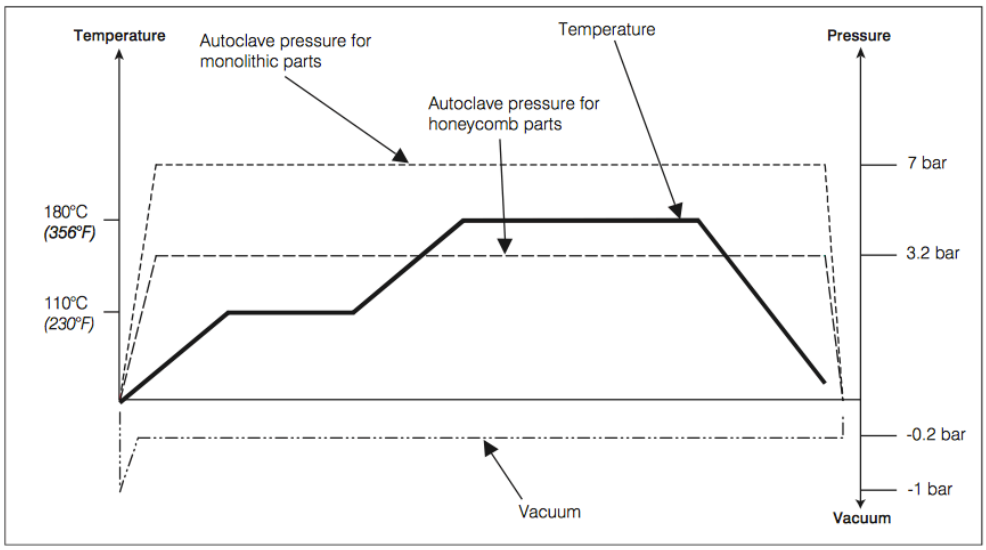

Figure A. 4 – Flow chart of the concatenation process.

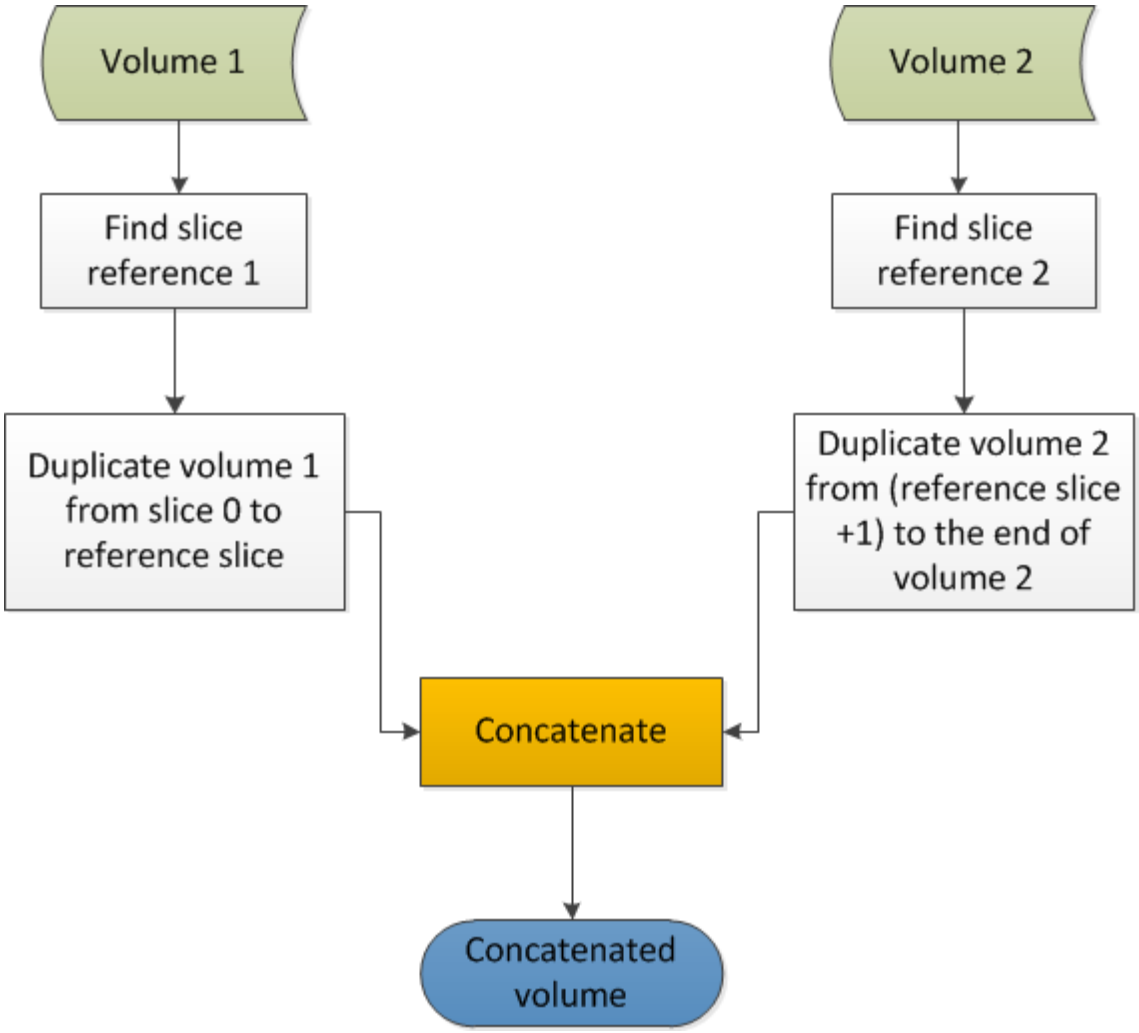

Figure A.5 - Flow chart of the iterative segmentation process.

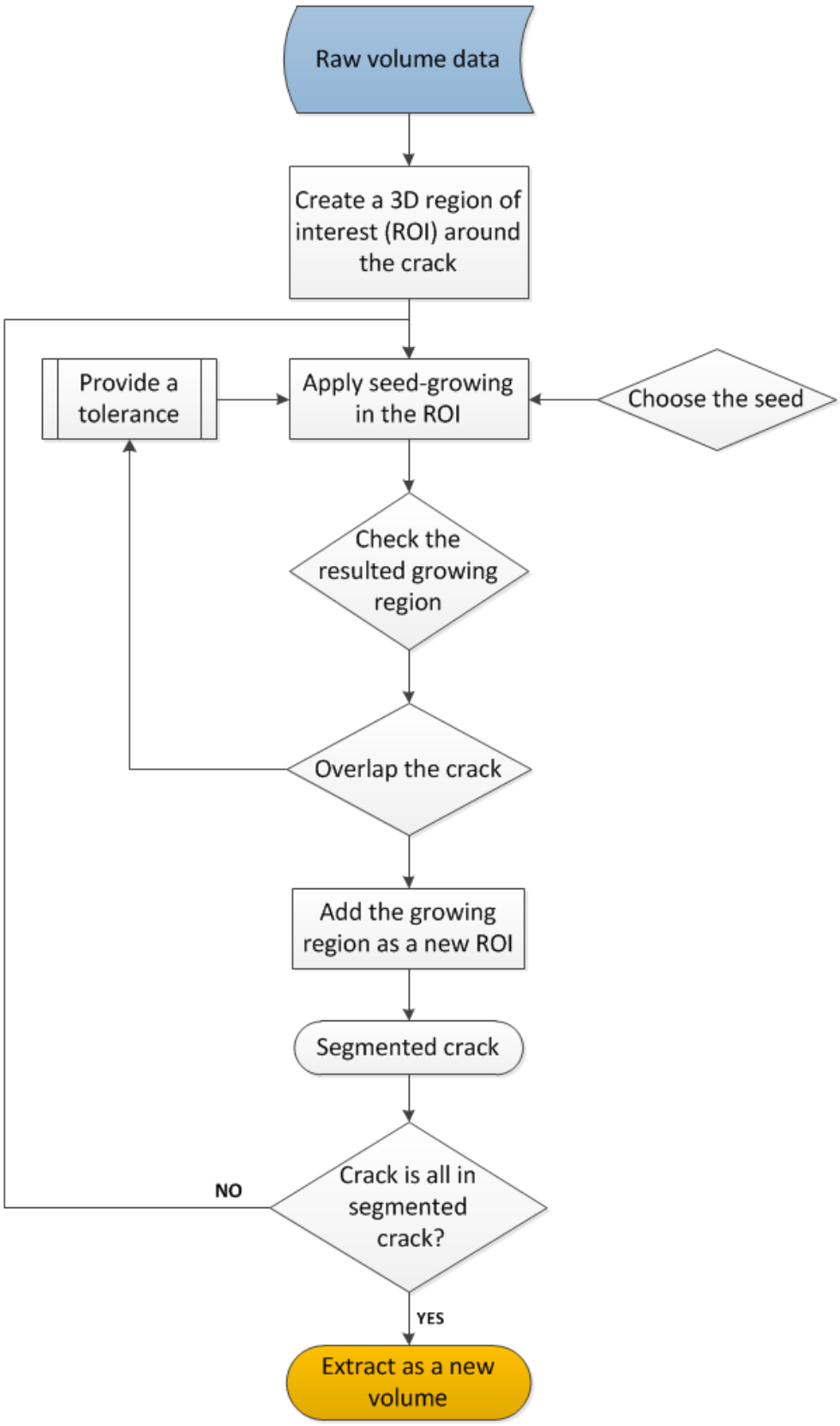

Figure A.6 - Flow chart of the crack opening displacement procedure.

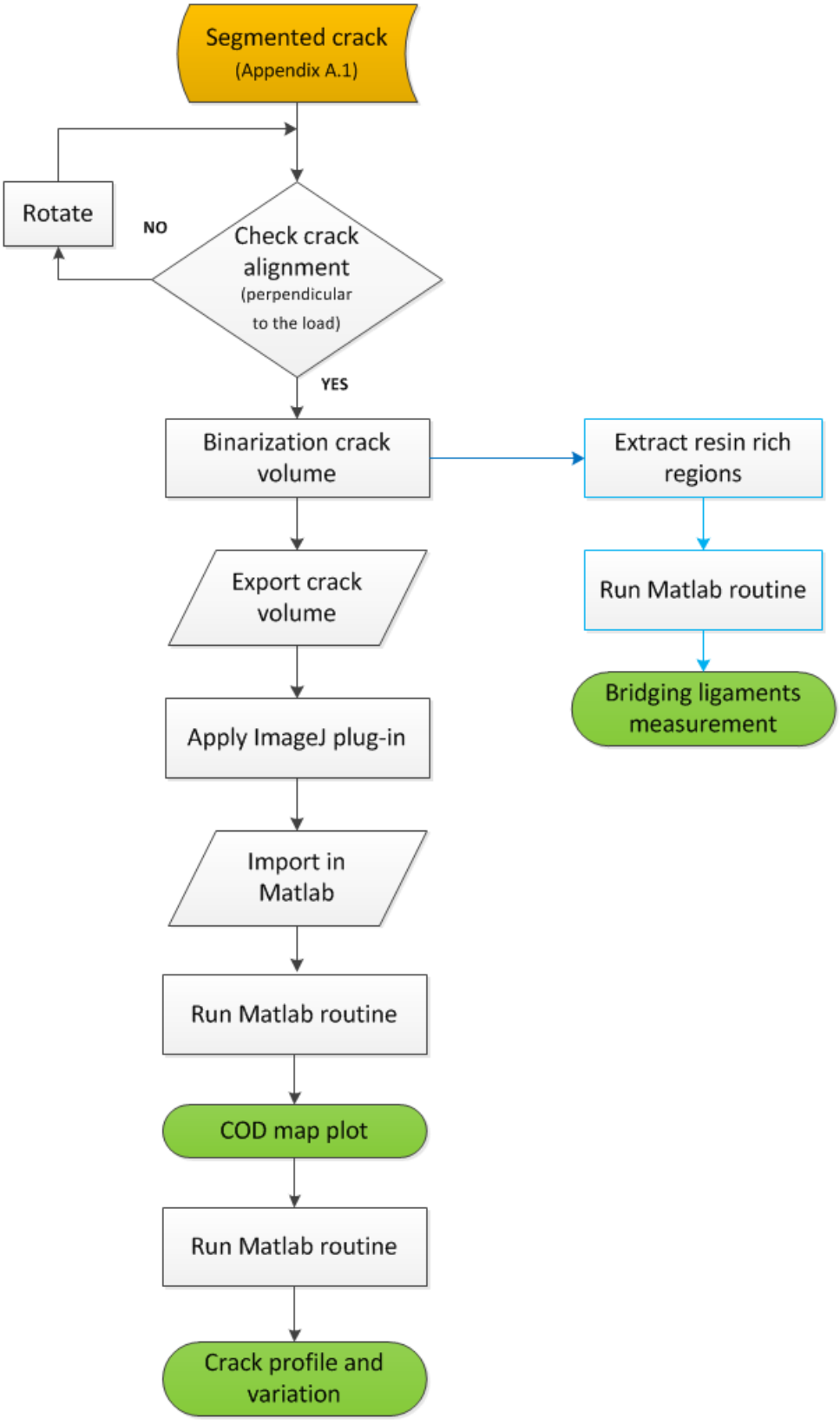

Chapter 4

Fatigue micromechanism characterisation in a particle – toughened system

This work represents the first use of high-resolution computed tomography to understand and quantify fatigue damage mechanisms in a polymer composite material. Particular attention was given to the micromechanical characterisation with the aim to evaluate the dependence of damage initiation and propagation on the microstructure, particularly with regard to the presence of toughening particles.

Due to the presence of narrow microcracks associated with the process of damage initiation, the combination of loaded coupons, ultra-high resolution imaging, and phase contrast effects, represents a suitable approach to investigate damage nucleation.

Damage behaviour has been compared with the quasi-static case, highlighting interesting differences in terms of damage initiation, bridging ligament formation and crack opening displacement. The content of this chapter has been partially published in Composites Science and Technology, vol. 99, pp. 22-30, 2014.

4.1 Introduction

Damage initiation in composites subjected to fatigue is known to occur even at relatively low loads, as shown from previous work [1], and being strongly dependent on the load ratio [1,2]. There is agreement in the literature that the first damage mode detected under monotonic and cyclic load in laminates is commonly intralaminar failure, often in the form of matrix cracks within the plies [1,3]. Studies conducted on the micromechanisms associated with matrix cracks orientated perpendicular to the loading direction (*i.e.* transverse ply cracks), have identified fibre debonding as the main process that leads to damage initiation [4]. No evidence has been provided regarding the initiation sequence for damage parallel to the loading direction (i.e. 0˚ ply splits). Previous investigations have reported the damage progression for a particle-toughened carbon/epoxy subjected to quasi-static tensile load [3] showing the nucleation of transverse ply cracks at relative low loads (∼20% UTS) with 0˚ ply splits initiating at ∼40% UTS. Moffat *et al.* [5] showed that the presence of the toughening particles, primarily in resin rich regions, results in a retardation of damage growth in these locations.

However, limited studies are present in the literature on the micromechanisms of fatigue damage initiation and propagation in composites. In this chapter, the particles-toughened system has been examined using SRCT imaging to characterize the micromechanical fatigue behaviour of damage initiation and propagation, assessing the rule of toughening particles. A direct comparison with the quasi-static case highlights similarities and differences between these two loading conditions. This provides important insights into the fundamental mechanics with potential implications for model development.

4.2 Assessment of damage initiation

Fatigue tests showed that particles do not exhibit an active role in terms of 0˚ ply split initiation, and do not represent the location where damage occurs in first instance.

Cracks nucleate in the resin between fibres in the fibre-packed regions within the 0˚ plies, and at this early stage do not propagate in the resin rich regions. Damage is discontinuous: many parallel microcracks initiate, separated from each other by the presence of small bridging ligaments (on the order of a few micrometers). This is clearly visible in Figure 4.1(a) and 4.1(b) where a cross-section parallel to the loading direction is shown for a specimen subjected to 200 fatigue cycles, at a peak load of 30% UTS. Therefore, even in the fibre-packed regions, where damage progression appeared as smooth and continuous in the developed stage, the process of initiation detected is similar to that observed in the resin rich regions during propagation.

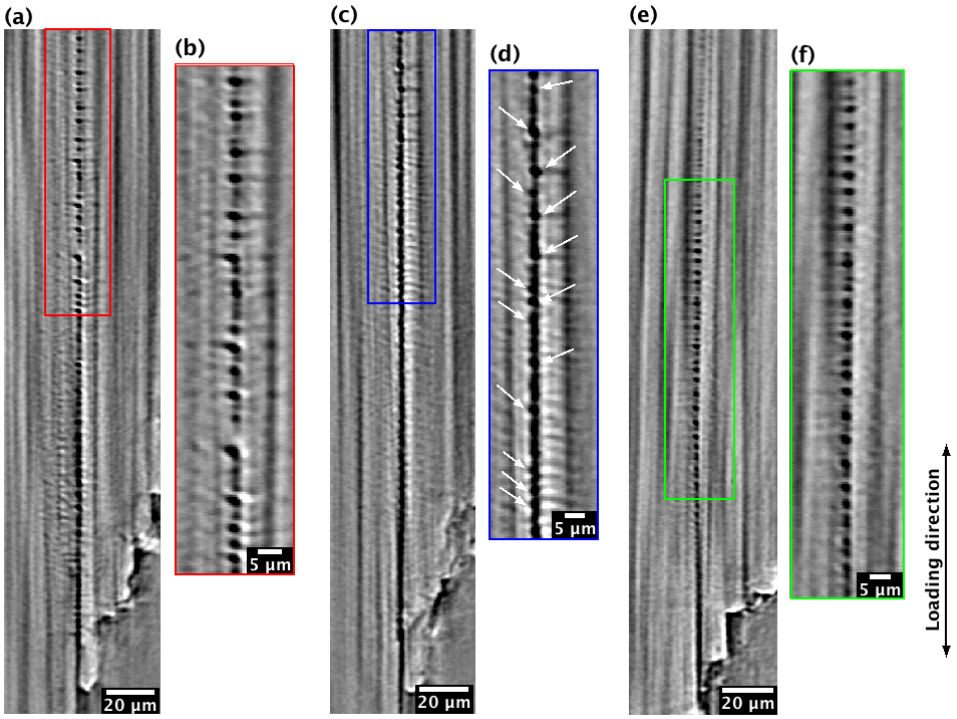

Figure 4. 1 - Cross-sections parallel to the loading direction of 0˚ ply split: (a)-(b) discontinuous fatigue damage initiation for a peak load of 30% UTS and 200 cycles, (c)-(d) continuous fatigue damage for a peak load of 30% UTS and 200 cycles, (e)-(f) quasi-static case for a load of 35% UTS.

The damage does not advance as a dominant crack, but is represented by small microcracks, separated from each other by resin ligaments. However, the length-scale between damage initiation in the fibre packet regions and the propagation in the resin rich regions is different: bridging ligaments along the fibre/matrix interface are on the order of a few micrometers (1-3 µm), whereas the ligaments in the resin rich regions

during damage propagation are defined by the thickness of the resin rich region and by particle size, resulting in the range of 10-100 µm. The small length of bridging during the process of damage initiation is related to the local microstructure: no particles are present in the fibre packed regions, and therefore only the bulk resin contributes to the formation of ligaments. These fail progressively due to the cyclic loading, creating a more continuous crack, as shown in Figure 4.1(c). Figure 4.1(d) highlights a detail of 4.1(c); the damage nucleation locations are easily discernible and indicated with white arrows. A direct comparison with the quasi-static case (Figure 4.1(e) and 4.1(f)), using a similar peak load (35% UTS), shows similar behaviour with the fatigue case (Figure 4.1(a) and 4.1(b)) in terms of damage location and bridging formation.

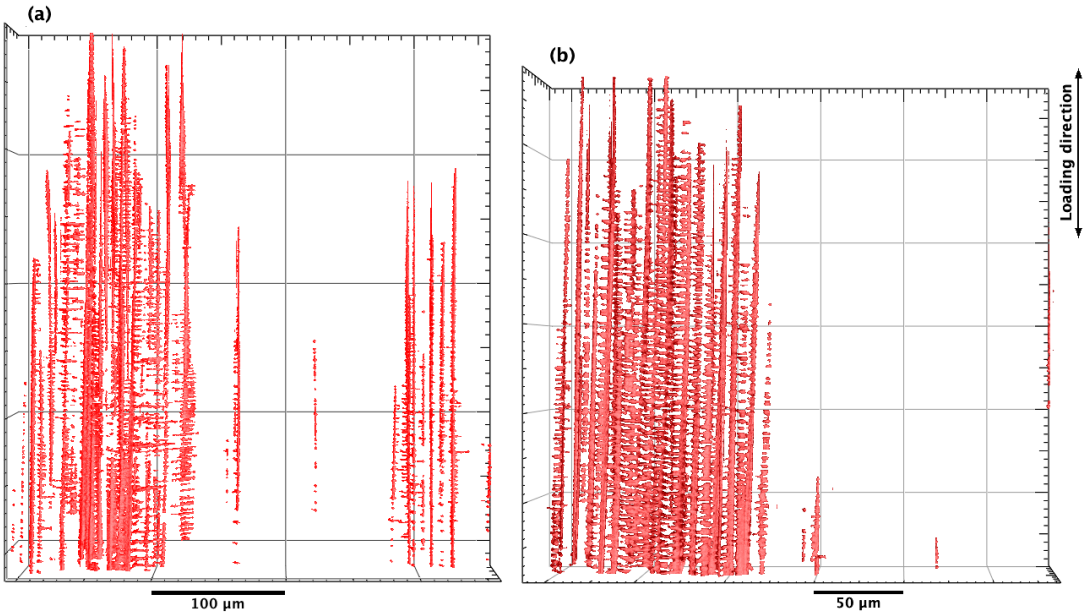

Figure 4. 2 - Three-dimensional rendering of damage initiation in the fibre-packed regions: 0˚ ply split in (a) fatigue case with peak load of 30% UTS up to 200 cycles, (b) quasi-static case for a load of 35% UTS.

Three-dimensional rendering of the 0˚ ply splits detected during this stage of damage initiation for the fatigue and quasi-static case are reported in Figure 4.2. A longer crack length, larger number of crack initiation sites across the ply thickness, and longer local microcracks characterize the fatigue case, Figure 4.2(a). In contrast, the quasi-static case shows damage mainly localized over only half of the ply thickness, with a crack front profile characterized by smaller and more frequent microcracks, Figure 4.2(b). The damage propagation through the ply thickness is arrested by the resin rich region

that connects the two 0˚ plies. The other half ply thickness does not exhibit developed damage, but only three separate damage initiation sites. A noticeable difference between the two loading conditions is the tendency of the crack to advance along the loading direction, removing locally the bridging ligaments for the fatigue case, Figure 4.2(a). Therefore, this initial stage of damage development appears as nucleation of single/local cracks, which tend to grow along the loading direction. Their coalescence across the ply thickness (perpendicular to the loading direction) is limited and the amount of remaining bridging ligaments (white region in Figure 4.2) across the split width is clear from the 3D rendering, Figure 4.2(a). The quasi-static case displays a different behaviour: more connections between single initiation sites across the ply thickness (split width) have been detected, and more bridging ligaments along the loading direction, Figure 4.2(b). Overall, damage under quasi-static loading is more connected and more uniform in terms of crack growth within the fibre-packed region with respect to the fatigue case, while fatigue case is characterized by a larger number of discrete damage nucleation sites.

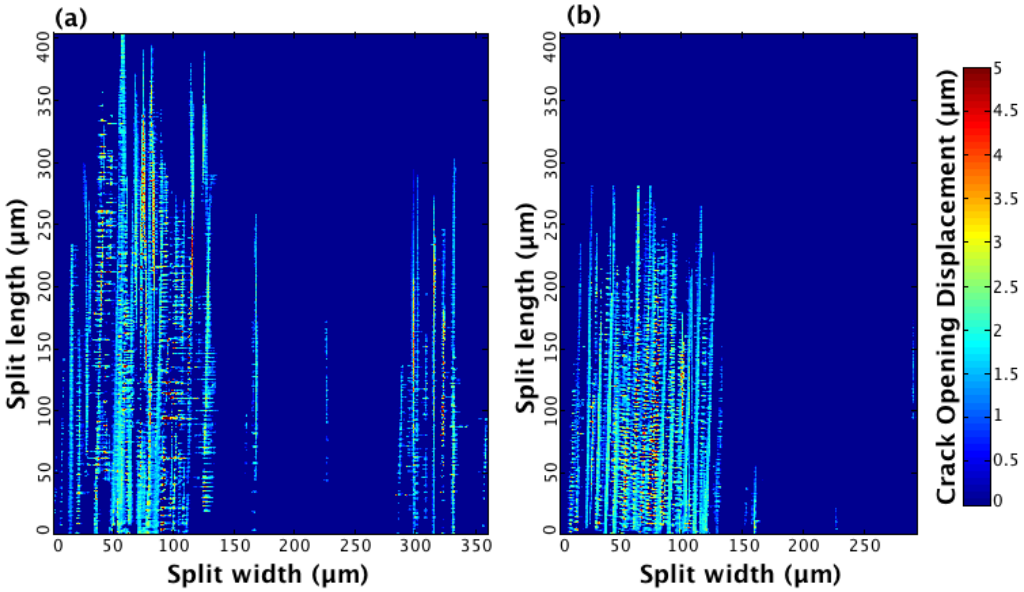

Figure 4. 3 - Crack opening displacement maps of the 0˚ ply split: (a) fatigue with peak load of 30% UTS and a number of cycles of 200 cycles, (b) quasi-static case under the load of 35% UTS.

The crack opening displacement maps associated with the 0˚ ply splits in Figure 4.2 were assessed and reported in Figure 4.3 for fatigue (Figure 4.3(a)) and quasi-static loading (Figure 4.3(b)). In the fatigue case there are similar values of COD over the

entire split area without a substantial difference between values at the split root and tip, Figure 4.3(a). The quasi-static case is characterised by decreasing values of COD from the root towards to the tip, even if at this stage the difference is not substantial. In addition, local higher values of COD (in the range of 50-100 µm across the split width) were detected, consistent with the reduced incidence of bridging across the split width and presumably less constraint of crack opening, Figure 4.3(b).

4.3 Fatigue damage modes

Segmentation enables three-dimensional fatigue damage to be characterized, providing the identification of the different damage types, their location and shape. This gives an insight regarding any reciprocal interaction between damage modes. Observations have shown the presence of intralaminar and interlaminar damage in the notch region after 10^4 fatigue cycles at loads of 30% and 50% UTS. Figure 4.4 illustrates the damage modes detected, consisting of: transverse ply cracks (in green); 0˚ ply splits (in red), and delamination (in blue). Transverse ply cracks initiate in the 90˚ ply within the notch region, propagate from one side of the specimen to the other, and increase in number with increasing load for a given number of cycles, Figure 4.4.

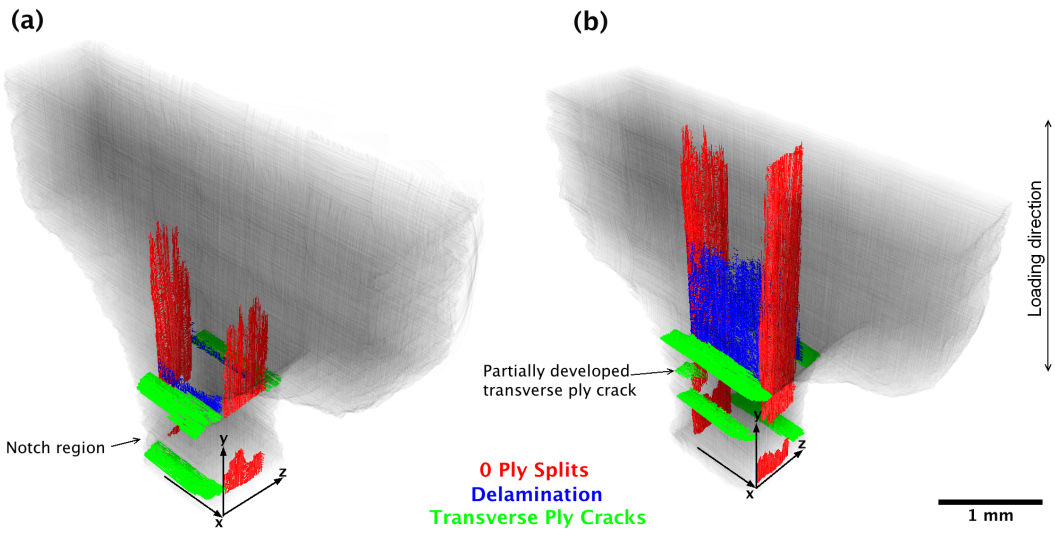

Figure 4. 4 -Three-dimensional fatigue damage for: (a) 30% UTS and (b) 50% UTS, at 10^4 cycles.

In the 50% UTS loading case one transverse ply crack was captured before complete propagation across the ply width, demonstrating its initiation at the specimen edge, as shown in Figure 4.4(b). 0˚ ply splits originated from the notch and propagated parallel to the load direction within the 0˚ plies. Increasing load level results in an increase in split length for a given cycle count, which exceeded the field of view of the scan for one split in the 50% UTS specimen, as shown in Figure 4.4(b). However, the other 0˚ ply split remained within the field of view. Other than longer split lengths at the higher load, the images of the two specimens in Figure 4.4 show splits with similar overall shapes and degrees of crack front serration. As will be discussed subsequently, the serrated split crack fronts are attributable to the presence of resin rich regions containing the majority of matrix toughening particles. Isolated fibre breaks were observed along the 0˚ ply splits; some of them were apparently fibres that were misaligned with respect to the loading direction. Delamination was seen at the (90/0) ply interfaces for both loads, Figure 4.4. The 30% UTS case is characterised by a very small-delaminated area, represented in blue in Figure 4.4(a).

Overall damage modes detected are broadly the same as those found in a previous study by Spearing *et al.* using radiography [1] on a double notch carbon/epoxy subjected to fatigue. However, conventional radiography is a 2D non-destructive technique, with a relatively low resolution, and therefore, provides limited information associated with the 3D nature of damage, such as crack profile shape and crack opening/shear displacements.

4.4 Micromechanical characterisation

The micromechanisms of damage propagation were seen to depend on the local microstructure, which plays a strong role in determining the crack path development across a given ply thickness. A 0˚ split, obtained by loading to 30% UTS (cycles 10^4), is shown in two orthogonal cross-sections at three locations, Figure 4.5. Figure 4.5(a) displays the split occurring within a resin-rich region. Debonded toughening particles are clearly visible, with their spacing essentially determining the distance between microcracks oriented at approximately 45˚ with respect to the overall tensile loading

direction. The damage does not propagate as a single/dominant crack, but discontinuously with bridging ligaments remaining intact between propagating microcracks. Figure 4.5(b) represents the typical behaviour in a region with a high local fibre volume fraction: damage is more constrained by the presence of fibres compared with the resin rich regions, being closely aligned with the loading direction.

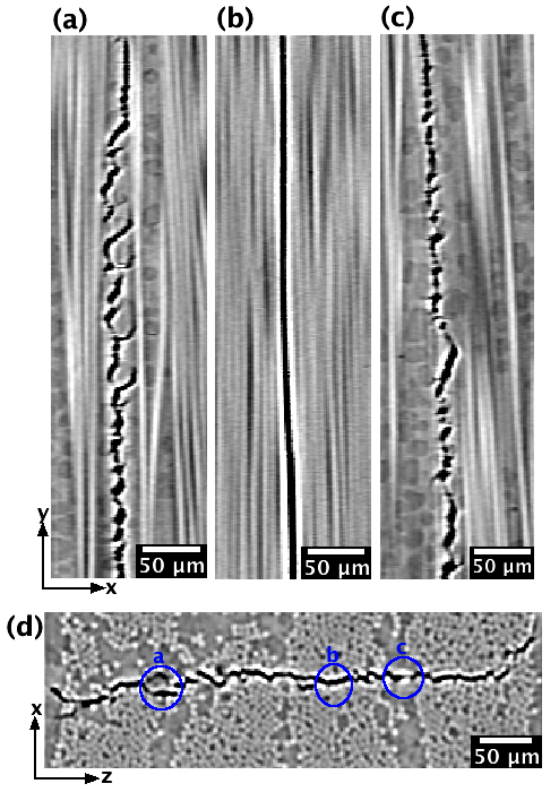

Figure 4. 5 - 0˚ Ply split growth for 30% UTS and 10^4 cycles in correspondence of three sections along the loading direction (a), (b), (c), and their locations through the ply thickness respectively (d).

Damage propagation appears continuous and straight, following the fibre/matrix interface with no bridging ligaments. The section shown in Figure 4.5(c) depicts split growth in a large resin rich region. The micromechanical behaviour is slightly different compared with the other resin rich region shown in section in Figure 4.5(a) due to the presence of microcracks along the split path which fracture (rather than debond) a few of the toughening particles, resulting in a more planar crack surface.

Similar behaviour of that reported in Figure 4.5 for the fibre-packet regions (Figure 4.5(b)) and in the resin rich regions (Figure 4.5(a)) has been identified for fatigue case at maximum load of 50% UTS.

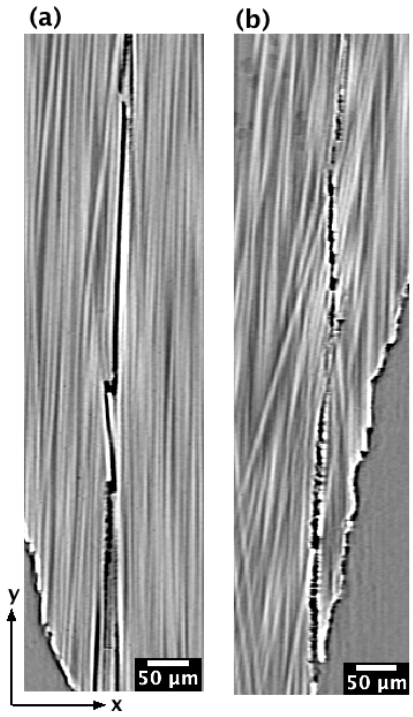

Figure 4. 6 - Fibre breaks along 0˚ ply split (a), and fibre misaligned associated with fibre breaks (b) for a peak load of 50% UTS after 10^4 cycles.

In situ experiments were designed to monitor damage development through and around the toughening particles, investigating their bridging behaviour, and to evaluate if particles retard damage propagation and what mechanisms contribute to this. This aspect will be addressed in chapters 5.

Fibre breaks were observed along the 0˚ split path, some of these are associated with misaligned fibres within the plies, as shown in Figure 4.6. It was not clear at this stage if the split development determines fibre breaks or if the two damage modes are not correlated, and consequently when the split interacts with fibres that are already broken, it is able to jump across the fibre breaks maintaining the direction parallel to the loading. The use of *ex situ* tests does not allow establishing a sequence of events, and consequently understand the micromechanisms, as in this case. Therefore, this aspect was further investigated by *in situ* scans, and the results achieved will be provided in chapter 6.

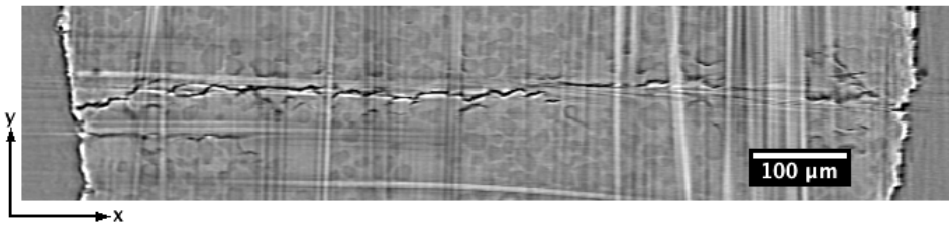

Figure 4. 7 - Transverse ply crack near the ply interface for 50% UTS fatigue load after 10^4 cycles.

The debonding of toughening particles also creates preferential crack paths for transverse ply cracks through the 90˚ ply thickness. Figure 4.7 illustrates a transverse ply crack section near the 90/0 interface. Misaligned fibres have also been detected across the transverse ply cracks; some of these act as bridging ligaments between the crack flanks, whilst others are seen to be broken.

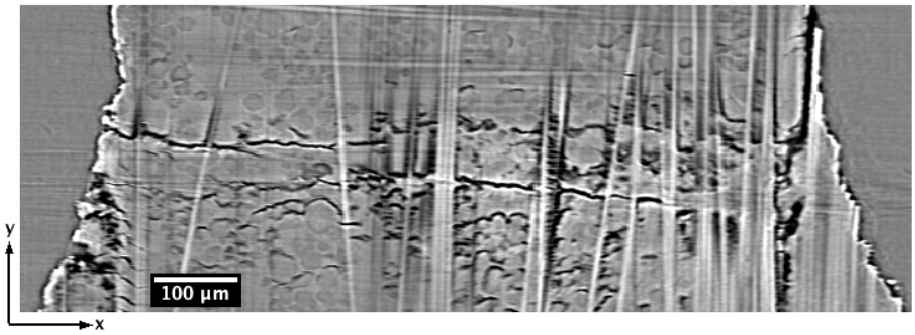

Figure 4. 8 – Cross-section parallel to the loading direction at the (90/0) interface of specimen loaded to 50% UTS, for 10^4 cycles.

Contrary to the case of quasi-static loading, where delamination appears only at the relatively high load levels, such as 60% UTS or higher [3], fatigue loading showed delamination occurring for a load level of 30% UTS after 10^4 cycles, as shown in Figure 4.4. Ply interfaces are zones of particular interest due to the damage interaction with toughening particles. Delamination initiates in this material via the interaction and coalescence of transverse ply cracks, 0˚ ply splits, and numerous fibre and toughening particle debonds, see Figure 4.4 and Figure 4.8. In this latter case, two interacting transverse ply cracks span the specimen width and combine with numerous partially debonded toughening particles and fibres to initiate delamination.

4.5 Damage quantification

Exploiting the observations of damage detected via three-dimensional tomographic images, damage quantification has been conducted focusing on the evaluation of the crack length and crack opening displacement of 0˚ ply splits, as explained in section 3.6.3, and shown in Figure 4.9. This follows earlier work [5,6] on 0˚ ply splits propagated under quasi-static loading. Three-dimensional damage rendering, represented in Figure 4.4, demonstrates that 0˚ ply splits are not planar; therefore, the COD map represents a 2D projection of the split onto the plane of the 0° plies, obtained by summing the voxels in the through-thickness direction. Figure 4.9(a) and Figure 4.9(b) show the crack opening contour map of 0˚ ply splits grown in fatigue loading at 30% and 50% UTS respectively for 10^4 cycles. The red regions correspond to large values of COD, while blue regions are uncracked. The COD maps evidence that the crack front growth does not advance evenly. Regions with higher local fibre volume fractions are characterized by a locally more advanced crack front, while in resin-rich regions toughening particles evidently interact with fatigue damage, and consequently retard crack growth, as shown in Figure 4.9. The COD map for an applied load of 30% UTS, Figure 4.9(a), exhibits two main regions across the split width (ply thickness) separated by a large resin rich region located roughly in the middle (250 μm), at the interface between the two central 0° plies. Both regions, from 50–220 μm and the other from 270-420 μm, are characterized by a jagged crack front; with similar overall extent on each side and retarded crack growth close to the interfaces with the 90° plies, i.e. from 0 μm to 50 μm and from 420 μm to 450 μm, where the crack interacts with particles at the interfaces. Another prominent resin rich region is located between 180-200 μm. The COD values appear similar across the majority of the split, with average values on the order of 2.5-3.5 μm at the root and 1.5-2.5 μm in the region 200 μm back from the crack tip. The COD map obtained for an applied load of 50% UTS is shown in Figure 4.9(b). Similar behaviour to the lower load is observed: two main zones are visible across the split width (ply thickness), from 50 μm to 250 μm and from 270 μm to 500 μm, corresponding to regions of higher fibre volume fraction, and separated by a resin rich region in the middle of the ply, at 250 μm. The split shape is

similar to the lower load case, with a comparable local jagged region of amplitude 200-250 μm.

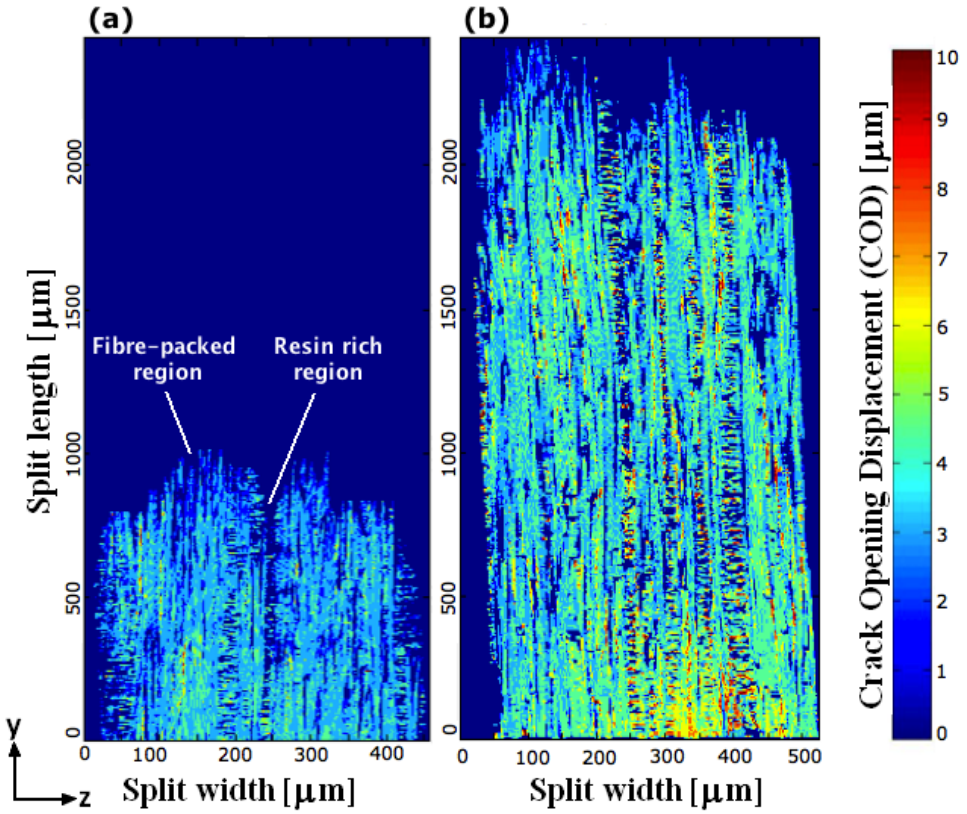

Figure 4. 9 - Fatigue crack opening displacement mapping for 0º ply splits at: (a) 30% UTS and (b) and 50% UTS (10^4 cycles).

The increase in load clearly results in a longer crack length for the same number of cycles (10^4), higher COD at the root, and reduced bridging within the resin rich regions and at the interfaces. Higher local values of COD have been also detected; mostly located along the cracked resin rich regions (e.g. 250-270 μm and 400-420 μm), within which the "echelons" of microcracks oriented at 45˚ respect to the load are clearly visible along the split length. The average COD values decrease from the root towards the crack tip. The COD map in Figure 4.9(b) depicts values on the order of 4.5-6 μm close to the root (within 250 μm) and in the range of 3-4.5 μm for the majority of the crack length. The crack opening displacement at the same distance (~250 μm) back from the nominal tip is similar to that measured for the lower load; within the range of 1.5-3 μm. It should be noted that the minimum COD value measurable is associated

with the voxel resolution, which in this case corresponds to 1.5 μm. Locations along the 0˚ ply splits have been referenced with respect to distance from the crack tip, in order to compare the COD evolution associated with these two different split lengths. For instance, at a position of 500 μm back from the crack tip for both loading conditions, the COD is lower for the lower load case. This is in part simply attributable to the load difference, but it is also clear that there has been additional degradation of crack wake bridging ligaments at the higher loading. For instance, at the central ply interfaces, close to the crack tip, there is a smaller intact bridging region at the higher load case, Figure 4.9(b), compared to that present in the lower load case, Figure 4.9(a).

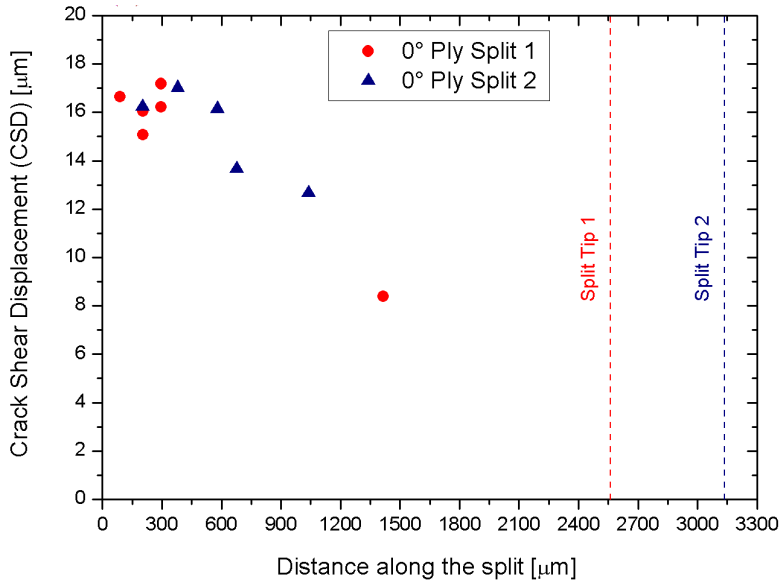

Figure 4. 10 - Fatigue crack shear displacement along the split lengths, obtained for 50% UTS load and 10^4 cycles.

Crack shear displacements (CSD) associated with the 0˚ ply splits have been evaluated following the methodology of Toda *et al.* [7] using the occasional fibre breaks along the 0˚ ply splits as reference features, as illustrated in section 3.6.4. CSD was obtained by measuring the relative displacements parallel to the fibre direction between pairs of fibre breaks on opposite faces of the split. Due to the small number of suitable broken fibres it is not possible to map the CSD over the whole split area. However, results indicated the dependence of CSD on the position along the split, decreasing with the distance from the notch towards the split tip, as shown in Figure 4.10, where the CSD

associated with two 0˚ ply splits within the same specimen and on the same notch side have been reported for the load of 50% UTS. The graph in Figure 4.10 shows the positions along the 0˚ ply splits for which measurements have been taken, relative to the crack root (position zero). In the first instance, the error associated with these measures is estimated to be of the order of ±1.5 μm, resulting from the voxel resolution of the scan.

4.6 Fatigue and quasi-static damage comparison

Qualitative analyses using 3D rendering of damage have demonstrated broadly similar behaviour between fatigue and quasi-static loading in terms of crack location and shape. However, fatigue loading clearly results in more extensive damage than for quasi-static loading at the same peak load. In addition, delamination is not detected for the load levels under quasi-static conditions considered, whereas delamination has been observed in the fatigue case.

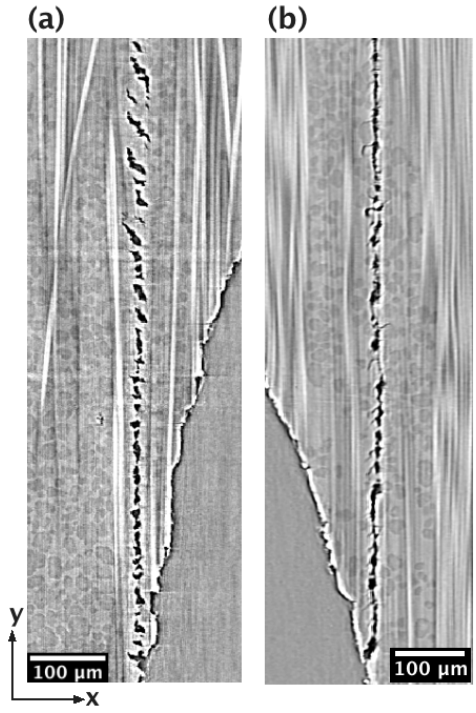

Figure 4. 11 – Comparison of the micromechanical behaviour along the 0˚ ply split in (a) quasi-static case loaded to 60% UTS, and (b) fatigue loaded to 50% UTS with number of cycles of 10^4.

In both quasi-static and fatigue a similar correlation between damage and microstructure was observed, suggesting similar micromechanical behaviour of 0˚ ply split propagation in resin rich regions and high-fibre volume fraction regions. Figure 4.11 displays a cross section of a 0˚ ply split in a resin rich-region for quasi-static loading (Figure 4.11(a)), and for fatigue (Figure 4.11(b)); loaded respectively at 60% UTS and at 50% UTS after 10^4 cycles. The discrete microcracks in the resin rich regions are much more apparent in the quasi-static loading case, as shown in Figure 4.11(a). In cyclic loading the bridges between the individual microcracks appear to have largely failed, presumably due to local cyclic degradation, yielding more continuous cracks as shown in Figure 4.11(b).

Similar behaviour is also demonstrated when comparing transverse ply cracks near the 0° ply interfaces, as shown in Figure 4.7 (fatigue) and Figure 4.12 (quasi-static). In the fatigue case the crack is distinctly more continuous with less bridging ligaments than this observed in quasi-static loading, Figure 4.12.

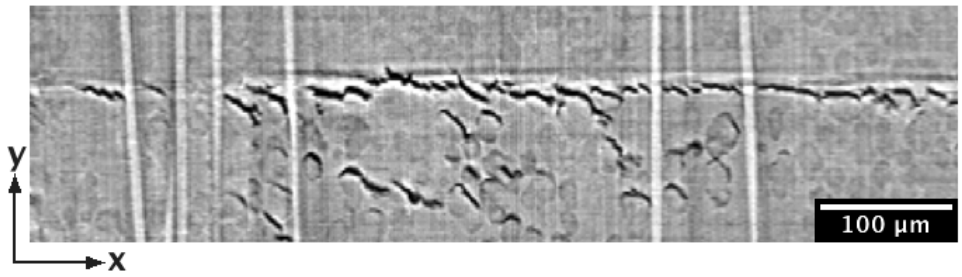

Figure 4. 12 – Transverse ply crack near the interface induced by quasi-static loaded to 50% UTS (courtesy A.J. Moffat).

In order to provide a direct comparison of crack morphology between the fatigue and quasi-static loading, CODs have been compared between 0˚ ply splits of two similar total lengths (1mm and 2.5mm) obtained in fatigue (albeit at lower maximum load levels) and quasi-static loading as shown in Figure 4.13. Fatigue plots correspond to the cases with peak loads of 30% and 50% UTS, and 10^4 cycles; whereas the quasi-static cases were obtained at load levels of 70% and 60% UTS respectively. Both fatigue and quasi-static loading result in similar features: a jagged crack front, with greater crack advance along areas with higher local fibre volume fractions, and crack

retardation along resin rich regions with the formation of bridging ligaments and echelons of microcracks oriented at 45˚ respect to the loading direction in the resin rich regions. The fatigue-loaded specimens, Figure 4.13(a) and 4.13(c), present more uniform crack advance across the ply thickness, along with more uniform crack opening displacement over the area of the crack (width and length) with respect to the quasi-static cases, Figure 4.13(b) and 4.13(d).

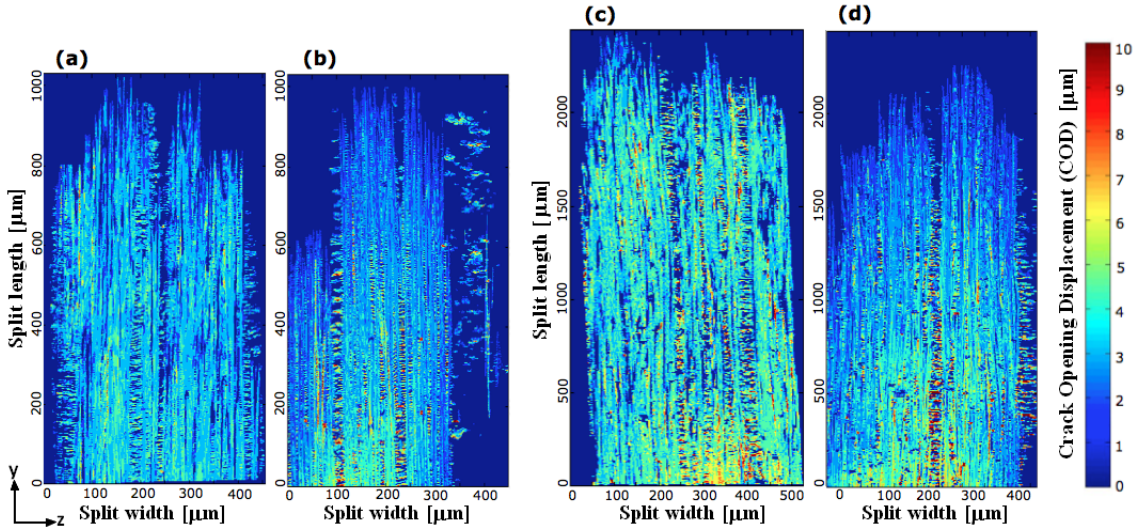

Figure 4. 13 - Split crack opening displacement contours: (a) crack length of 1 mm: fatigue case with peak load of 30% UTS and 10^4 cycles, (b) quasi-static case for 70% UTS; crack length of 2.5 mm: (c) fatigue case with peak load of 50% UTS and 10^4 cycles, and (d) quasi-static case for the load of 60% UTS.

In terms of uniformity of crack across the ply thickness (split width), large uncracked resin rich areas characteristically seen in static load cases (e.g. a band of ~100 µm width along the right hand ply interface of the 0˚ ply split in Figure 4.13(b)) were largely absent in the fatigue loading cases. Comparing Figure 4.13(a) with 4.13(b) and Figure 4.13(c) with 4.13(d), it is apparent that in the quasi static cases (4.13(b), 4.13(d)) there is a significantly higher crack opening displacement towards the centre line of the 0˚ ply split and/or the centre line of the resin rich regions. Figures 4.13(a) and 4.13(c), associated with fatigue loading, exhibit more uniform crack opening displacements across the ply thickness.

The comparison between these two loading conditions highlights the presence of higher average values of COD in the fatigue cases (Figure 4.13(a), 4.13(c)), even though the applied loads were higher for the quasi-static cases (Figure 4.13(b), 4.13(d)). This is

attributable to the reduced number and reduced cross-sectional area of load bearing ligaments in the wake of the fatigue cracks, and/or the corresponding incidence of delamination in fatigue. The presence of delamination in the fatigue case could affect the COD due to the fact that the 0˚ plies are less constrained. However, the delamination is not completely developed along the split length, as shown in Figure 4.4, extending only along 10% and 35% of the total 0˚ ply split lengths considered for the COD maps for the cases of loading at 30% and 50% UTS respectively. The quasi-static cases considered showed no delamination for the smaller crack and a minimal area of delamination for the longer crack, only amounting to 5% of the 0˚ ply split length.

Crack shear displacement has been also compared for both loading conditions, using the method described in the section 3.6.4. Again, it is not possible to map CSD across the all specimen, but comparing similar locations and load levels it is found that for fatigue, a CSD of 16.2 μm (± 1.5 μm) is developed at 50% UTS at a distance of 500 μm from the notch mid-plane, whereas for quasi-static a value of 8.4 μm (± 1 μm) has been reported by Moffat *et al.* [5].

Higher CODs and CSDs for the fatigue cases compared to similar split lengths in quasi-statically loaded specimens are consistent with the local degradation of bridging ligaments under fatigue loading, as illustrated in Figure 4.13(a) and 4.13(c), resulting in reduced effectiveness of bridging and higher crack opening and shear displacements.

4.7 Conclusions

Similar micromechanisms of damage initiation have been identified in fatigue and quasi-static loading in a particle-toughened carbon fibre-epoxy composite system. Cracks nucleate in the matrix/fibre-matrix interface region within volumes of high local fibre-volume fraction in the 0˚ plies. This initial stage is not characterized by the propagation of a single dominant crack, but multiple microcracks separated by bridging ligaments have been observed. Therefore, the micromechanisms of damage initiation are similar to those of damage propagation. Study of the crack morphology reveals interesting differences between the fatigue and quasi-static case in terms of nucleation sites of damage, higher in number in the fatigue case, and bridging

ligaments formation along and across the 0˚ ply split, which resulted less effective in the fatigue case.

Novel observations have been obtained for the micromechanisms of fatigue crack growth. It seems likely that a key mechanism of fatigue in intralaminar damage is the degradation of bridging ligaments introduced by particles in the fatigue crack wake rather than due to processes at or ahead of the crack tip; resulting in higher, more uniform crack opening (and shear) displacements and less-jagged crack fronts compared to quasi-static loading. This observation may have consequences for the damage tolerant design of structures for which durability is important, and also in the development of strategies for developing fatigue damage resistant materials. The ability to quantify crack opening and shear displacements has the potential to allow the quantitative comparison of the effectiveness of toughening strategies in achieving fatigue damage resistance and provide a basis for trade-offs with quasi-static and impact damage resistance.

4.8 References

[1] S.M. Spearing and P.W. Beaumont, "Fatigue damage mechanics of composite materials. I: Experimental measurement of damage and post-fatigue properties," *Composites Science and Technology*, vol. 44, pp. 159-168, 1992.

[2] E. Gamstedt and B. Sjogren, "Micromechanisms in tension-compression fatigue of composite laminates containing transverse plies," *Composites Science and Technology*, vol. 59, pp. 167-178, 1999.

[3] A.E. Scott, M. Mavrogordato, P. Wright, I. Sinclair, and S.M. Spearing, "In situ fibre fracture measurement in carbon-epoxy laminates using high resolution computed tomography," *Composites Science and Technologies*, vol. 71, pp. 1471-1477, 2011.

[4] R. Harrison and M. Bader, "Damage development in CFRP laminates under monotonic and cyclic loading," *Fibre Science and Technology*, vol. 18, pp. 163-180, 1983.

[5] A.J. Moffat, P. Wright, J-Y. Buffiere, I. Sinclair, and S.M. Spearing, "Micromechanics of damage in 0 splits in a [90/0]s composite material using synchrotron radiation computed tomography," *Scripta Materialia*, vol. 59, pp. 1043-1046, 2008.

[6] P. Wright, A. Moffat, I. Sinclair, and S.M. Spearing, "High resolution tomographic imaging and modelling of notch tip damage in a laminated composite," *Composites Science and Technology*, vol. 70, pp. 1444-1452, 2010.

[7] H. Toda et al., "A 3D measurement procedure for internal local crack driving forces via synchrotron X-ray microtomography," *Acta Materialia*, vol. 52, no. 5, pp. 1305-1317, 2004.

Chapter 5

Evaluation of the effect of toughening strategies on fatigue damage progression

The current work represents the first use of in situ *high-resolution computed tomography to assess fatigue micromechanisms in toughened and untoughened CFRP systems. The advantage of conducting* in situ *fatigue experiments consists of monitoring the interaction between damage and microstructure during multiple cycle increments on the same coupon, removing any ambiguities associated with the use of different* ex situ *specimens.*

The results presented herein show that the different microstructures associated with these three systems affect damage propagation, creating non-uniform crack growth in the toughened systems, and a more uniform propagation for the untoughened system. The formation of bridging ligaments associated with the toughened systems has a fundamental role in the process of fatigue degradation. The content of this chapter has been partially published in Composites Science and Technology, vol. 109, pp. 32-39, 2015.

5.1 Introduction

Several approaches to enhance the toughness of CRFRPs have been developed to a sufficient level of maturity that they are employed in service in aerospace applications; however, the underpinning micromechanisms of failure associated with the modified microstructures have not been widely investigated. The literature review provided in Chapter 2 has covered the toughening mechanisms observed in thermoset resins (section 2.6), and the different variables that could have influence on the toughness behaviour, such as particle type, particle volume fraction, and particle size. Studies on toughening micromechanisms in composite laminates are relatively limited (section 2.7), and the effectiveness of toughening strategies under fatigue loading has been largely neglected.

The work presented in this chapter represents the first use of *in situ* synchrotron radiation computed tomography imaging to understand the micromechanisms operating in toughened and untoughened composite systems subjected to fatigue loading. The comparison of damage propagation for three different material configurations provides insights as the effect of fatigue on shielding micromechanisms in toughened composite systems. The particular focus of this work is to determine the evolution of the crack tip process zone and the corresponding damage events at the length-scale of individual microstructural features (e.g. toughening particles, and fibres).

5.2 Macro-scale measurement of splits

The damage types detected in the three systems considered (particle toughened system, untoughened and intrinsically toughened system) are: matrix/intralaminar cracking within the 90˚ and 0˚ plies, interlaminar cracks (delamination) at the interfaces between plies, and fibre breaks. The 0˚ ply split length *(l)* as a function of the number of fatigue cycles, using the same loading condition, is reported in Figure 5.1 for the three material systems. Crack length was normalized with respect to the notch

dimension *(a)*, following the approach used by Spearing *et al.* [1]. Cycle 1 represents the crack length obtained for a quasi-static tensile load (50% UTS). The solid bar describes the average value, and the scatter was evaluated as the total range of the measurements. Similar trends were reported in previous studies for carbon/epoxy [1] and carbon/PEEK systems [2].

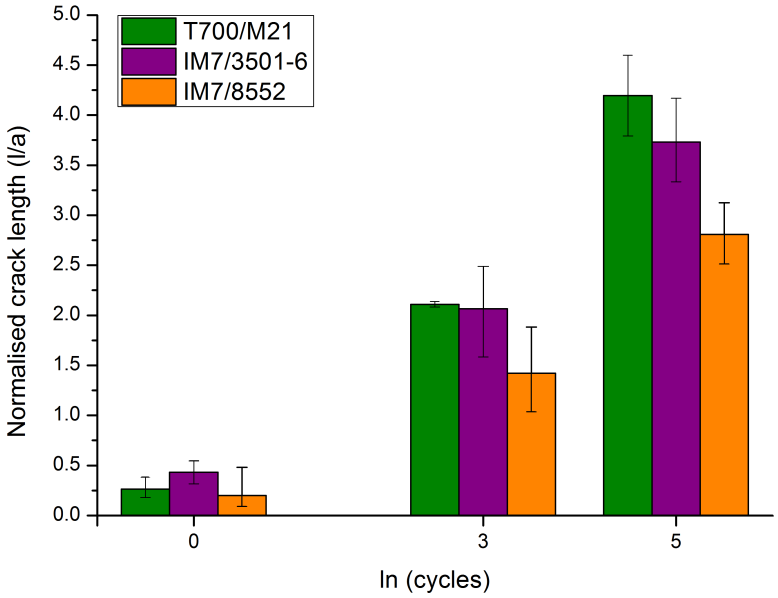

Figure 5. 1 – Normalized 0˚ ply split length as a function of the fatigue cycles for the particle toughened (M21/T700), untoughened (3501-6/IM7), and for the intrinsically toughened system (8552/IM7) cycled at a peak load of 50% UTS.

Figure 5.1 indicates the beneficial effect of toughening systems particularly under quasi-static loading, for which the crack length of the untoughened system is clearly longer than in the toughened systems after the first cycle. After further cycling the three materials behave quite similarly, with no significant improvement in fatigue crack growth resistance afforded in the toughened matrix materials. A similar observation was made for the relative lack of improved fatigue damage resistance of PEEK matrix material versus epoxy in ref [2]. Therefore, the assessment of the underpinning micromechanisms of the different systems, described in this chapter, is conducted to provide insights regarding the fatigue behaviour, focusing on role of the toughening mechanisms in fatigue, relative to their effectiveness in enhancing quasi-static fracture resistance.

5.3 Particle-toughened system

The particle-toughened M21/T700 system showed highly non-uniform growth of the fatigue crack front, exhibiting zones of retarded crack growth corresponding to the resin rich regions, which contain the majority of toughening particles, and zones of accelerated growth corresponding to local high fibre-volume fraction regions. Detailed imaging has been focused on resin rich regions with the aim of understanding potential shielding mechanisms that may influence the overall damage progression, see Figure 5.2. Damage development appears very discontinuous in the resin rich regions, characterized by multiple microcracks, which are mainly associated with the debonding of toughening particles, as shown in Figure 5.2(a).

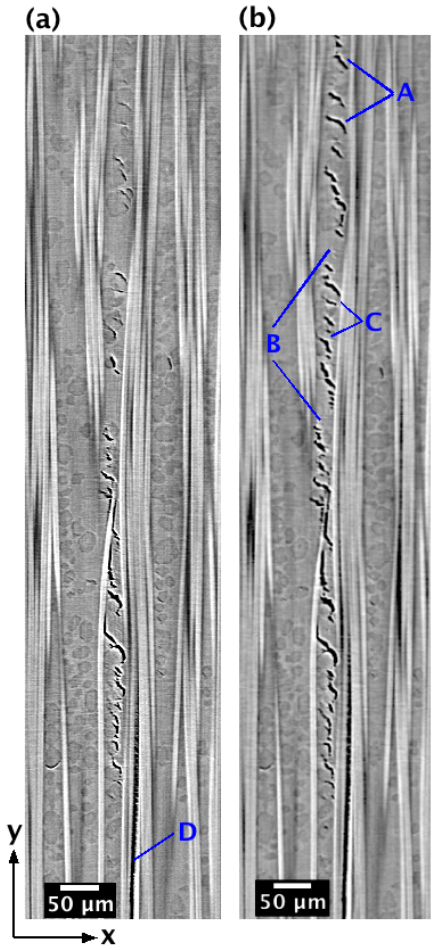

Figure 5. 2 – 0˚ ply split growth propagation in the particle toughened system within the resin rich region for a peak load of 50% UTS: 700 cycles (a) and 800 cycles (b).

Interfacial debonding of particles tends to follow a specific direction: damage is typically oriented at 45˚ with respect to the loading direction, and this is consistent with the influence of macroscale shear on what then appears to be essentially a tensile particle debonding/crack initiation process at the microscale. The growth of a 0˚ ply split associated with a further 100 cycles at a peak load of 50% UTS is shown in Figure 5.2(b), where the same cross-section of Figure 5.2(a) has been reported. From a direct comparison before and after the additional 100 cycles (Figure 5.2(a) and 5.2(b)), the crack growth is easily identified in Figure 5.2(b). Damage progression is seen to be highly discontinuous, with crack extension being dominated by the growth and coalescence of many small cracks, rather than the progression of a dominant crack tip.

The primary process of damage propagation at the nominal crack tip, defined as the furthest extent of the damage zone, is represented by particle debonding (Figure 5.2(b), highlighted with (A)), which results in the creation of bridging ligaments along the crack wake. The process is distributed over a length of approximately 1 mm around the nominal crack tip, with partially debonded particles remaining intact relatively far behind the nominal crack tip (over several hundred micrometers) and acting as bridging ligaments between the crack flanks. The periodicity and scale of microcracking is clearly defined by the particle size and separation distances, as shown in Figure 5.2(b). Crack bridging ligaments consist of resin between debonded particles (e.g. Figure 5.2(b), highlighted with (B)) and/or particles themselves (e.g. Figure 5.2(b), highlighted with (C)). The presence of particles clearly promotes the nucleation and propagation of local damage events. Figure 5.2(a), (D) shows the difference between the split propagation along the fibre/matrix interface, which appears smooth and straight, versus the damage developed in the resin rich region, characterized by significant crack deflection.

A cross-section parallel to the loading direction of a 0˚ ply split is provided in Figure 5.3. Considering the same region of interest in the coupon, several bridging ligaments present at 700 cycles (Figure 5.3(a), location (A) and (B)) are removed, wholly or partially, at 800 cycles (Figure 5.3(b), location (A') and (B')). Two different behaviours have been detected, depending on the resin ligament size: (i) small bridges (on the order of ~10-20 μm); these fail by connecting adjacent microcracks along the direction of damage propagation, as show in Figure 5.3b (A'); and (ii) large ligaments (on the

order of ~50-100 µm cross-section), fail by the formation of local echelon microcracks within the resin ligament itself (i.e. not from toughening particles) at 45˚ to the loading direction, as shown in Figure 5.3b (B).

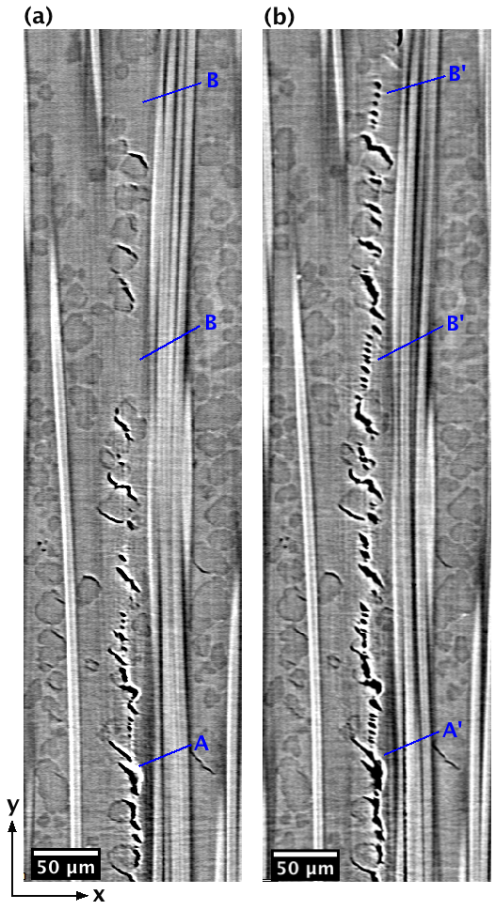

Figure 5. 3 - Failure of the resin bridging ligaments in the particle toughened system: 700 cycles (a) and 800 cycles (b), peak load of 50% UTS.

Further analysis showed that the echelon cracks detected in the bulk matrix originate from the damage at the fibre/matrix interface, extending into the bulk resin, Figure 5.4. Figure 5.4(a) shows the damage that has propagated in the resin rich region (red serration), and the fibres along the loading direction (in grey). The direct connection between echelon formation in the resin and the damage at the fibre/matrix interface underneath (continuous damage in red) is clearly visible in the Figure 5.4(b), where the material on the flank of the damage was rendered as partially transparent. Toughening

particles act also as bridging ligaments when they are partially debonded along the crack wake, as shown in Figure 5.2(b), location (C).

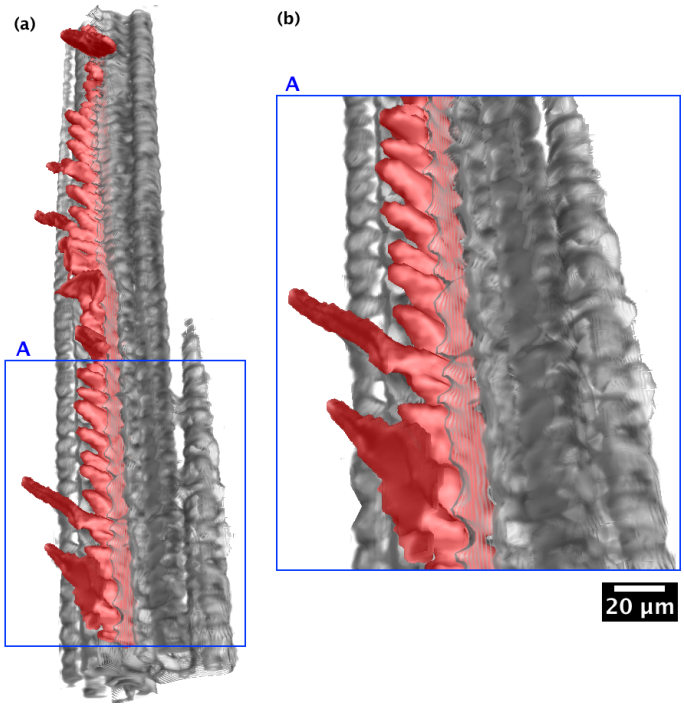

Figure 5. 4 – 3D rendering of the echelons in the bulk resin (a) that originates as propagation of the continuous damage at the fibre/matrix interface (b). Damage is represented in red, while the fire along the loading direction in grey.

The cross-section perpendicular to the loading direction, reported in Figure 5.5(a), similarly shows a toughening particle that bridges between the surfaces of a 0˚ ply split. Additional cycles can lead to complete debonding of such particles, with the consequent linkage of the two crack branches and the loss of bridging function as shown in Figure 5.5(b). A few particles located along the 0˚ ply split propagation path fracture internally during cyclic loading. Figure 5.5(c) displays an example of this viewed on a cross-section parallel to the loading direction. Damage initiated within the particles, and progressed along the same orientation of surrounding echelon formations (*i.e.* at 45˚ to the loading direction). The reason for such particle fracture is unclear, but is potentially attributable to variations in the relative particle/matrix interface strength. Similar behaviour has been detected for particles located at the 0˚/90˚ interfaces, as shown in Figure 5.5(d).

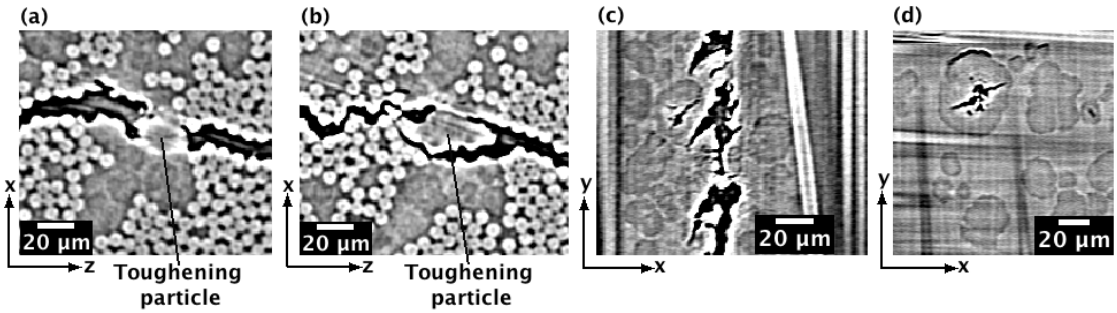

Figure 5. 5 – Particle failure modes in the particle-toughened system: particle bridging crack flanks (a), particle completely debonded (b), particle fractured along the 0˚ ply split path (c) and at the interface (d).

Particles debonded were also observed in regions neighbouring the crack plane, independent of the main crack/split development. In these cases debonding does not exhibit a preferential orientation, as observed along the 0˚ ply splits, with local interface failure being influenced by some combination of microstructural and/or micromechanical effects, Figure 5.6(a). The 100 additional cycles does not involve a progression of particle debonding, which appears to be unchanged between Figure 5.6(a) and 5.6(b).

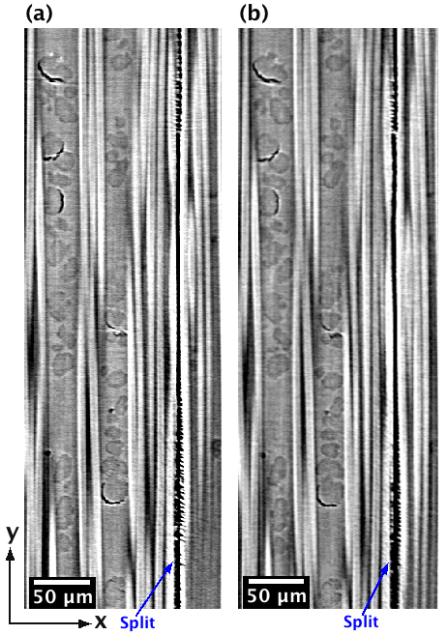

Figure 5. 6 - Debonding particles close to the region of damage (split) for a peak load of 50% UTS and (a) 700 cycles and (b) 800 cycles.

Similar conclusions on particle partially debonded, which are not on the wake of the main damage development, can be done considering the full split width, taking into account that the number of cycles added is relatively low. Single fibre breaks and doublets (two adjacent broken fibres) have been detected along the 0˚ ply split path associated with misaligned and bridging fibres, as shown in Figure 5.7. Focusing on fibre breaks that specifically occurred in the 700 to 800 cycle interval, Figure 5.7(a) depicts a slightly misaligned fibre bridging the 0˚ ply split.

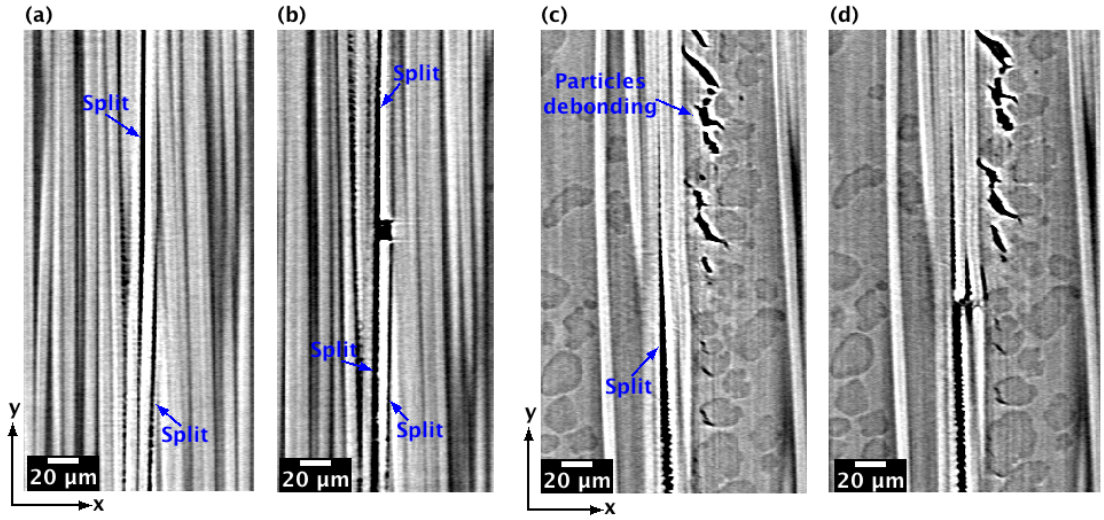

Figure 5. 7 - Fibre breaks along the 0˚ ply split in the particle-toughened system: partially debonded fibre at 700 cycles (a, c), fibre failure at 800 cycles (b, d).

Fibre debonding occurs asymmetrically with respect to the loading direction, and consequently the traction associated with the fibre bridging is consistent with local bending of the fibre. The additional cycle increment causes failure of the fibres in the region where debonding between the fibre/resin interface has occurred, an example is shown in Figure 5.7(b). Damage coalescence between high fibre-volume fraction regions and resin rich regions can lead to fibre breaks, as shown in Figure 5.7(c) and 5.7(d). In the first stage the 0˚ ply split propagates as fibre/matrix debonding, and at the same time, in an adjacent resin rich region in the form of particle debonding and microcracking; with fibres in between acting as bridges, as shown in Figure 5.7(c). The next increment (to 800 cycles) causes complete fibre/matrix debonding and the failure of the fibres. Further analyses conducted on quasi-static tensile tests showed that the first cycle at this load level introduces just a few fibre breaks (~4) over the average

crack length of 400 µm (see Figure 5.1). The number of fibre breaks detected after 700 cycles is roughly twenty times higher (74 fibre breaks) than in the quasi-static case. Therefore, it is indicated that whilst fatigue leads to additional fibre breaks, it is less clear whether these are all due to the failure of bridging fibres, and also the extent to which they affect the residual properties of the material.

5.4 Untoughened system

The untoughened system exhibits fewer and smaller resin-rich regions, especially within each individual ply. This microstructure clearly affects damage initiation and propagation, which occurs preferentially at the fibre/matrix interfaces for both 0˚ ply splits and delaminations, as shown in Figure 5.8, for the specific case of a 0˚ ply split.
As such, 0˚ ply splits manifest similar behaviour to the particle-toughened system within the fibre packed regions, developing relatively straight and smooth fracture paths.

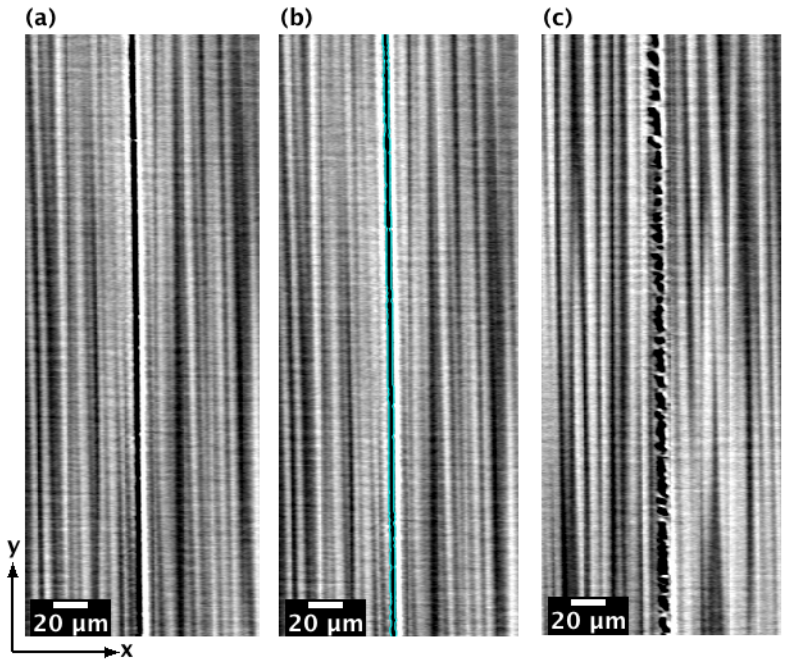

Figure 5. 8 - 0˚ ply split propagation in the untoughened system at 50% UTS and 700 cycles: within the fibre packed region (a) with representation of the segmented damage (b), and corresponding to fibres surrounded by resin (c).

This is depicted in Figure 5.8(a) and 5.8(b), where damage (in cyan) was segmented to distinguish features with similar greyscale values. When the fibres are surrounded by resin, the crack propagation was seen to be discontinuous, assuming the form of small microcracks at the fibre/matrix interface, retaining very small resin ligaments (on the order of a few micrometers), e.g. Figure 5.8(c). Fatigue loading of the untoughened system generated a higher number of fibres breaks for the given load level and number of cycles (50% UTS and 700 cycles) compared with the particle toughened system for which fibre breaks were observed only along the 0˚ ply split path. Conversely, the untoughened system exhibits fibre breaks within the bulk composite (0˚ plies).

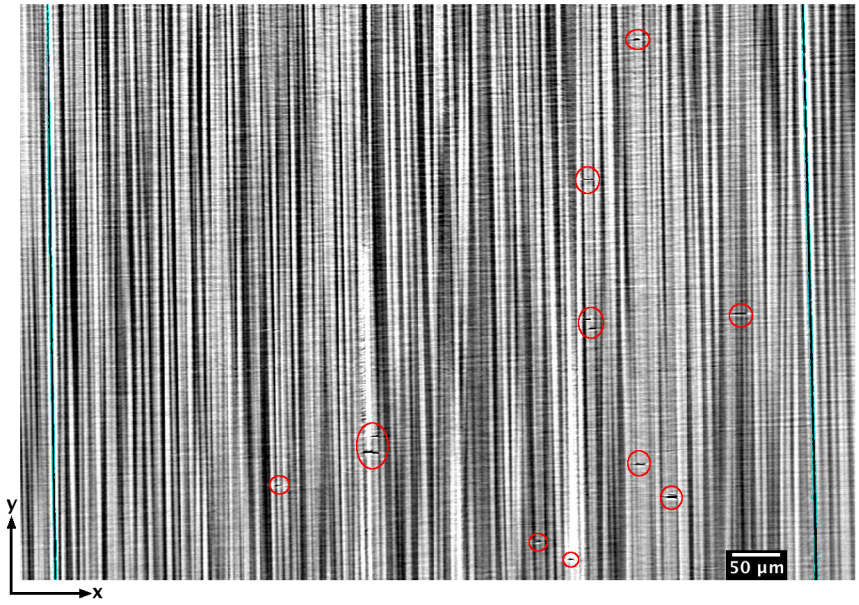

Figure 5. 9 - Fibre breaks (in the red circles) in the untoughened system within the 0º plies, in the region between splits, segmented in cyan. Peak load of 50% UTS and 700 cycles.

The number of fibre breaks counted for the untoughened material was 191 versus the 74 breaks detected for the particle-toughened system. The location (notch region) and the volume of material considered to compare fibre failure on the different material systems are the same for all the cases assessed. Specifically, the untoughened system shows single and multiple fibre breaks along the 0˚ ply split, but also a significant number of fibre breaks within the 0˚ plies (highlighted with red circles), in the region

between the 0˚ ply split paths (segmented in cyan), as shown in Figure 5.9. While it is clear that these are not all due to fibres bridging the splits, the mechanism of fibre failure away from the path of the split is unclear and merits further investigation.

5.5 Intrinsically toughened matrix system

The intrinsically toughened matrix (8552) results in micromechanical behaviour that is, in broad terms, intermediate to the untoughened and particle toughened systems. Intralaminar damage initiates in high fibre volume fraction regions as fibre debonding and propagates in a relatively straight/simple manner as detected for the untoughened system, Figure 5.10.

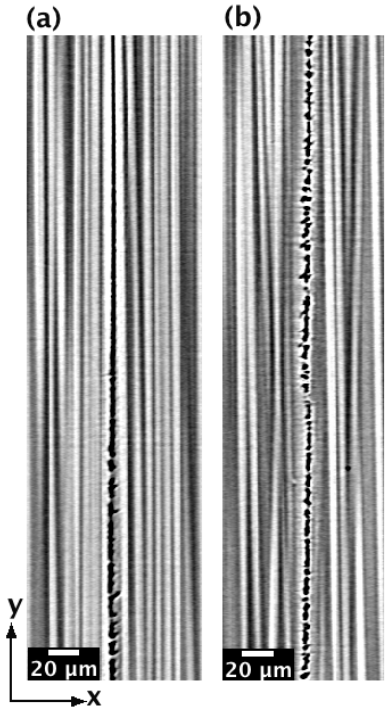

Figure 5. 10 - 0˚ ply split growth in the intrinsically toughened at 50% UTS and 700 cycles in the fibre packed region (a), in comparison with fibre surrounded by resin (b).

Failure in the resin rich regions occurs via small microcracks originating at the fibre/matrix interface. The resin remaining between microcracks forms bridging ligaments, which are smaller than those in the particle-toughened system and of a

similar scale to those observed in the untoughened system. Single and multiple fibre breaks have been detected along the 0˚ ply split paths and within the 0˚ plies in the regions close to the splits. 147 fibre breaks were detected for the intrinsically toughened material system which is smaller than that observed for the untoughened system (191), but higher than in the particle-toughened system (74). In addition, fibre breaks detected in the intrinsically system are located along the 0˚ ply splits, but also within the 0˚ plies, as observed for the untoughened system.

5.6 Crack morphology

The toughening micromechanisms associated with the particle-toughened system, such as particle debonding, crack deflection, fracture surface roughness and the formation of bridging ligaments are more evident in the 3D representation of a region of interest within the resin rich region of the particle toughened system, Figure 5.11.

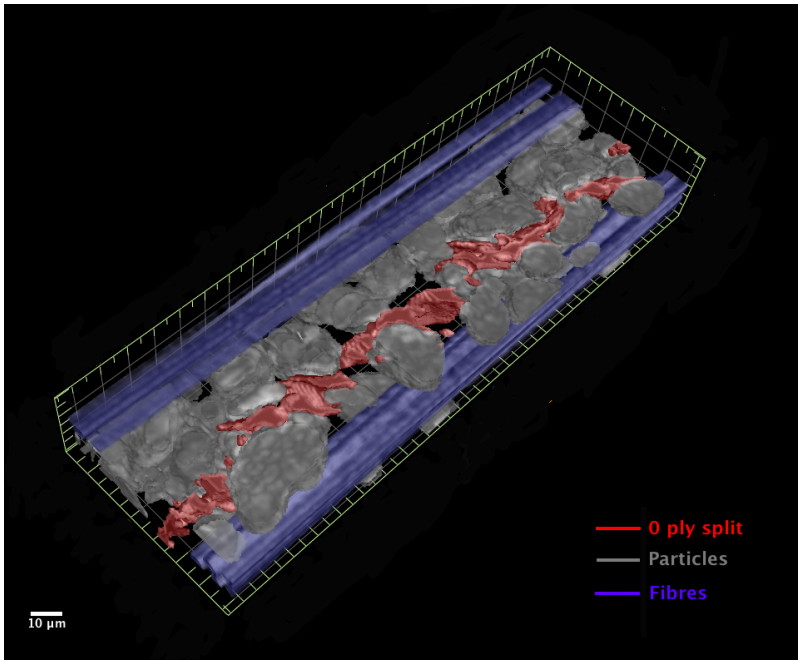

Figure 5. 11 - 3D rendering of a region within the resin rich zone for the particle-toughened system: 0˚ ply split (red), toughening particles (grey), and fibres oriented along the loading direction (blue).

Due to the modest contrast with respect to the surrounding resin, the particle segmentation requires a degree of manual intervention. Features of interest are

segmented and coloured by type: fibres along the loading direction are in blue, toughening particles in grey and the 0˚ ply split damage in red. The density of the particles within the volume taken into account is higher than those represented in Figure 5.11. However, to facilitate visualization of crack interactions, only the particles along the 0˚ ply split have been segmented. Such image analysis confirmed that the presence of particles creates a preferential path for damage initiation and propagation; the split surface conforms to the particle shape exactly in many locations, and follows the particle/resin interface (to within the resolution of these images). Therefore, particle volume, particle distribution, and consequent reciprocal distance between particles may be identified as parameters of fundamental importance in defining the processes of damage growth.

The two-dimensional slices used to assess the micromechanical interaction between damage and microstructure were exploited to segment the fatigue damage and provide a 3D representation of the crack front profile, as shown in Figure 5.12 for the peak load of 50% UTS and 800 cycles. This allows the effect of toughening micromechanisms on the crack growth to be visualised. Interest was focused on 0˚ ply splits and different crack profiles have been detected, depending on the material system considered, and in particular on the interaction between damage and the local microstructure.

The three-dimensional rendering of the damage within the particle-toughened system (Figure 5.12(a)) confirms that particles play a fundamental role in crack development, also shown in Figures 5.2, 5.3 and 5.5. The local crack path is three-dimensional with a roughness and tortuosity defined by the particle size, and is a significant fraction of the inter-ply resin rich region. By contrast, as indicated by Figure 5.8, the untoughened material exhibits much more planar crack surfaces, with 3-D features determined by the scale of the fibre diameter and the inter-fibre spacing, Figure 5.12(e).

Figures 5.12(a-c), obtained using the segmentation process, shows plan views of one of the splits from each material. Toughening mechanisms in the particle system are seen to act locally within the material, with corresponding consequences for apparent local fracture energy dissipation, consistent with the uneven crack advance, as shown in Figure 5.12(a).

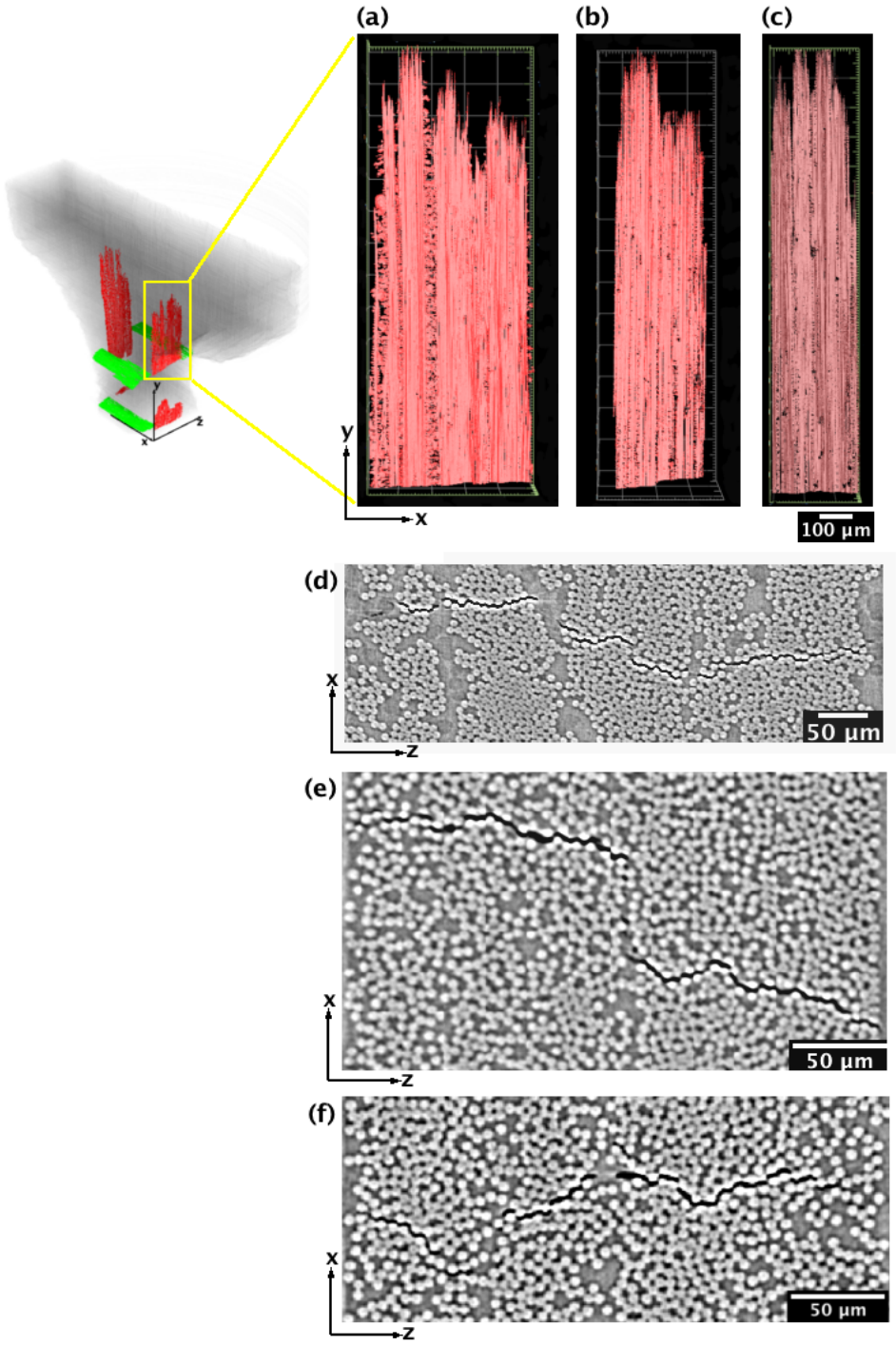

Figure 5. 12 – Three-dimensional rendering of the 0˚ ply split at 50% UTS and 800 cycles, with a typical cross section perpendicular to the loading direction: (a, d) particle-toughened system; (b, e) untoughened system; and (c, f) intrinsically toughened system.

The presence of retarded zones (pinning of the crack front) is related to the location of resin-rich regions containing the majority of toughening particles, which inhibit crack propagation, as shown in the cross-section perpendicular to the loading direction,

Figure 5.12(d). The result is a crack front that exhibits a “jagged” shape (Figure 5.12(a)), characterized by extended crack growth in the high fibre volume fraction regions, associated with extensive debonding of fibre/matrix interfaces.

Figure 5.12(b) displays the 0˚ ply split segmentation for the untoughened system. Fibre packing is more homogeneous in the untoughened system, and this may play a role in defining the crack path. Consequently, split propagation at the matrix/fibre interface is more uniform across the ply split width due to the absence of resin and particle-rich bands. The crack propagation along the ply thickness, which shows two levels of growth is affected by the fact that these two damage branches develop along two fracture planes, corresponding to two different initiation sites and they are not connected each other, as shown in cross-section in Figure 5.12(e). However, considering each branch separately the crack growth is relatively uniform, as shown in Figure 5.12(b). Resin bridging ligaments (black regions within the segmentation) comprise a relatively small area (fraction) compared with the particle-toughened material, with a corresponding expectation of reduced effectiveness of bridging and hence crack shielding. The intrinsically toughened system demonstrated an intermediate behaviour, between that of the particle-toughened and the untoughened systems, as shown in Figure 5.12(c). In particular, even though no toughening particles are present within the matrix, the resin rich regions act as crack retardation sites, creating a non-uniform crack growth, and contributing to the overall toughness. The cross-section perpendicular to the loading direction, presented in Figure 5.12(f) confirms that the split was constrained by a resin-pocket, whereas in fibre rich volumes the extent of growth was higher. The density of bridging ligaments along the crack wake is much less than for the particle-toughened system but is slightly higher than for the untoughened system.

The root mean square (RMS) of the crack front profiles was calculated in order to quantify the variation. The particle toughened and the intrinsically toughened systems exhibited similar values (RMS $\sim$230 μm), which were much higher than the value measured for the untoughened system (RMS $\sim$70 μm). In this latter case the RMS was evaluated separately along the two crack branches, each one showed a similar value.

5.7 Discussion

The experimental observations conducted have shown that the fatigue damage micromechanisms depend on the microstructure and on the material composition, leading to distinctly different behaviour between toughened and untoughened systems. The particle-toughened system shows an increase in fracture resistance in the intraply region due to the presence of particles and the stacking sequence considered (cross-ply layup, with a resin rich region between the 0˚ plies). A key mechanism identified for the particle-toughened system is the degradation during cycling of bridging ligaments introduced by particles along the crack wake. This is apparently a significant aspect of fatigue damage propagation in this material. Previous results found by Bull *et al*. [3,4] considering composites subjected to impact damage showed that the tendency to form bridging ligaments close to the crack tip correlates strongly with the resulting impact damage resistance. This suggests that fatigue may be particularly detrimental to structures that have already sustained damage due to impact. It is likely that bridging ligaments play some role in determining the effective toughness, and these are adversely affected by fatigue. However, the bridging ligaments in the untoughened system are at a much smaller scale, defined by the matrix properties and the inter-fibre spacing, which is smaller in the absence of particles. Consequently, the micromechanical behaviour of the untoughened matrix system shows clear differences in terms of damage propagation under fatigue loading with respect to the particle-toughened material. The presence of extensive but localized fibre breaks (single or multiple) under fatigue merits further investigation, which could have implications for damage tolerant design approaches. This aspect will be discussed in Chapter 6.

It is noteworthy that macroscopically, the three toughening strategies examined in this chapter result in similar fatigue damage growth rates, as evidenced by Figure 5.1. This suggests that, although toughening has a strong role in the quasi-static response and local aspects of fatigue development, it is much less significant in affecting overall fatigue propagation. The intrinsically toughened system showed marginally the lowest crack length at all numbers of cycles considered, as shown in Figure 5.1. It is likely that in fatigue, toughening particles become isolated and fail, and consequently the

toughening strategy is rendered less effective. We also note that in previous work [2,5] a macroscale “Paris Law” approach has worked well to model fatigue damage growth in both untoughened and intrinsically toughened systems, which suggests that micromechanical process zone aspects can till be treated with a reasonable degree of similitude, at least under simple, steady-state growth conditions. Further work is required to understand this, perhaps using an approach of cohesive elements and addressing the issue of small scale versus large scale bridging conditions.

5.8 Conclusions

In situ SRCT has been used to investigate the fatigue behaviour of toughened and untoughened CFRP composite material systems. Results showed that damage propagation is related to the local microstructure. Toughened systems exhibit different damage behaviour in resin-rich regions and fibre-packed zones, which leads to a non-uniform crack growth. Zones of retarded crack growth correspond to resin rich regions, which contain bridging ligaments. This was most pronounced in the particle-toughened system, and less so in the intrinsically toughened system. There is evidence that the load cycling contributes to the failure of bridging ligaments, especially in the toughened particle system, and consequently increases the crack length and the crack opening displacement. The untoughened system showed more uniform damage propagation across the crack front, due to the more uniform microstructure. Consequently, fracture occurs by the propagation of a well-defined crack front, whereas in the toughened systems there is considerable micro cracking ahead of the crack tip and crack bridging processes behind the crack tip. The untoughened system showed a higher number of fibre breaks within the 0˚ plies with respect to the toughened systems, particularly within regions close to the 0˚ ply splits.

5.9 References

[1] S.M. Spearing and P.W. Beaumont, "Fatigue damage mechanics of composite materials. I: Experimental measurement of damage and post-fatigue properties,"

Composites Science and Technology, vol. 44, pp. 159-168, 1992.

[2] S.M. Spearing, P.W.R. Beaumont, and M.T. Kortschot, "The fatigue damage mechanics of notched carbon fibre/PEEK laminates," *Composites*, vol. 23, pp. 305-311, 1992.

[3] D.J. Bull, A.E. Scott, S.M. Spearing, and I. Sinclair, "The influence of toughening-particles in CFRPs on low velocity impact damage resistance performance," vol. 58, pp. 47-55, 2014.

[4] D.J. Bull, S.M. Spearing, I. Sinclair, and L. Helfen, "Three-dimensional assessment of low velocity impact damage in particle toughened composite laminates using micro-focus X-ray computed tomography and synchrotron radiation laminography," *Composites: Part A*, vol. 52, pp. 62-69, 2013.

[5] S.M. Spearing, P.W. Beaumont, and M.F. Ashby, "Fatigue damage mechanics of composite materials. II: a damage growth model," *Composites Science and Technology*, vol. 44, no. 2, pp. 169-177, 1992.

Chapter 6

Fibre failure during fatigue loading

This chapter describes the fibre break behaviour detected for the particle-toughened system: the micromechanisms of fibre failure were investigated by in situ *fatigue tests, while the accumulation and distribution of fibre breaks for different loading conditions were determined from* ex situ *fatigue cases.*

Quantitative analysis was conducted considering the same volume (notch region) for direct comparison of the total number of fibre breaks in the different cases; whilst the evaluation of the fibre breaks along 0˚ ply splits and the fibre break distribution in the bulk composite were conducted considering concatenated volumes to include the different damage modes in the field of view.

A comparison with an equivalent quasi-static case was used to assess similarities and differences with the fatigue cases.

6.1 Introduction

Fibre failure represents a fundamental issue in the progress of damage accumulation, and is presumed to be a critical factor in determining final failure under tensile loading [1]. In this context different approaches have been developed to simulate fibre failure dominated conditions [2-6]. However, experimental results to validate models are limited. *In situ* computed tomography was used for the first time by Scott *et al.* [7] to investigate fibre failure in a double notch particle-toughened system loaded in tension. They found a suddenly acceleration of fibre breaks in the bulk (0˚ plies) within the notch region for loads higher than ~85% UTS, suggesting that failure under a tensile load is associated with fibre cluster formation at high loads (from 95% UTS), which are not necessarily linked with the locations of fibre breaks at lower loads [7]. Therefore, new cluster, defined as more than two adjacent fibre fragmented, can occur directly in a new location rather than a progressive growth of the number of breaks in a specific place [7]. The investigation of fibre breaks in composites under fatigue loading is not trivial due to the fact that *in situ* tests are highly desirable in order to monitor the accumulation of fibre failure in the same specimen. This approach represents an advantage for the understanding of all the other damage modes due to the variability of composites materials. Particularly, in the context of fibre fracture, where factors such as the influences of statistical distributions of fibre strength, fibre packing, and fibre alignment, make the analysis of fibre failure complex when multiple interrupted tests are considered. In this chapter, both *in situ* and *ex situ* fatigue experiments have been used to assess the micromechanisms of fibre failure.

6.2 Methodology

The material system used to assess fibre breaks under fatigue loading was the particle-toughened system, for further details refer to the Chapter 3, Section 3.1.1. The procedure used and the loading conditions applied in the analysis were described in Section 3.4. However, further details regarding the geometry and the reference

volumes taken into account in the different comparisons are provided in this section. The approach chosen in this work was to make use of *in situ* tests to understand the micromechanisms of fibre failure along the 0˚ ply splits, see Section 3.4. The volume of reference used for the *in situ* tests is represented by all the filed of view achievable from the scan, starting from the middle of the notch up to 1.5 mm, which roughly represents the geometrical dimension of the notch region, Figure 6.1(a). The investigation on *ex situ* tests, aimed to quantify fibre failure, resulted on a broader volume that starts from the middle of the notch and extends for a length of 3 mm, Figure 6.1(b).

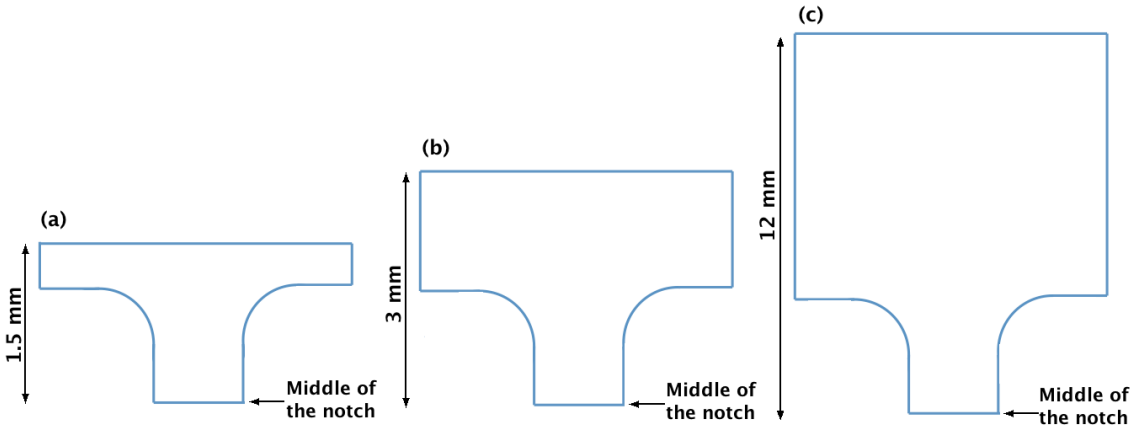

Figure 6. 1 – Volume of reference used for: (a) *in situ* evaluations; (b) notch region in the *ex situ* experiments; (c) extended volume to include all the 0˚ ply split lengths.

The reason of choosing a wider region than the 'geometrical notch region' is due to the fact that the stress distribution (whether a model is implemented to simulate the behaviour described) is not only limited to the notch region (represented as geometrical notch), but on a broader area. Therefore, the choice to double the dimension to take into consideration could represent a reasonable region to include most of the stress distribution, and consequently quantify the fibre breaks. On this basis, when in this chapter the fibre breaks are compared between different loading conditions, referring to the '*notch region*' does not correspond with the geometrical notch, but with a double length (~3 mm), as shown in Figure 6.1(b). The distribution of the fibre breaks along the 0˚ ply splits has been evaluated taking into account the total length of the split associated with the different loading conditions (variation of load

and/or cycles), regardless of the total volume, and consequently regardless of the number of scans required to include the entire crack in the field of view. In this latter case multiple scans were concatenated to include all the 0˚ ply splits length for each loading conditions (e.g. Figure 6.1(c)), following the methodology described in the Chapter 3, Section 3.6.1.

6.3 Micromechanisms of fibre failure

The micromechanisms that lead to fibre fragmentation of a fibre located along the 0˚ ply split for the particle-toughened system have been investigated by *in situ* fatigue tests, already mentioned in Chapter 5, Figure 5.7, and discussed further in this section. The analysis conducted was aimed not only to count the total number of breaks added due to the additional number of cycles (100), but understand the micromechanisms and assess whether the increase of the number of breaks occurs in a location that already exhibits fibre break(s) or as new fibre breaks nucleation. The comparison of the two cyclic conditions (700 and 800) has shown 12 fibre breaks added during the 100 cycles, where the fibre breaks detected at 700 cycles were 74. The fibre length considered in these cases, strictly related to the voxel resolution chosen, was of ~1.5 mm starting from the middle-notch, which roughly corresponds with the geometrical dimension of the notch, Figure 6.1(a). The fibre breaks associated with the increment of 100 cycles are located all along the 0˚ ply splits and most of them appear as single breaks (10) with only two doublets (two adjacent fractured fibre). Figure 6.2 illustrates the micromechanisms of failure associated with a single fibre break along the 0˚ ply split. In correspondence of 700 cycles the fibre is debonded from the matrix due to the propagation of the split, Figure 6.2(a). The traction associated with the fibre bridging causes the local bending of the fibre. The fact that the fibre is debonded from the surrounded matrix does not allow load to be transferred from fibre to matrix along the debonded surface. Therefore, the next cycle increment caused the fibre failure in the middle of the bridging section, as shown in Figure 6.2(b). Depending on the direction of the shear, and on how the fibre bridges the damage, two different types of fibre breaks micromechanisms have been detected, shown in Figure 6.2 and in Figure 6.3.

The direction of the shear, shown in Figure 6.2(a), highlights that the failure of the fibre is due to bending and shear (bending/shear) in this case. In the same coupon fibre failure due to a tensile effect has been detected, an example is reported in Figure 6.3. In this latter case, the shear direction is the same reported in Figure 6.2, but the fibre orientation respect to the damage propagation is opposite of that shown in Figure 6.2.

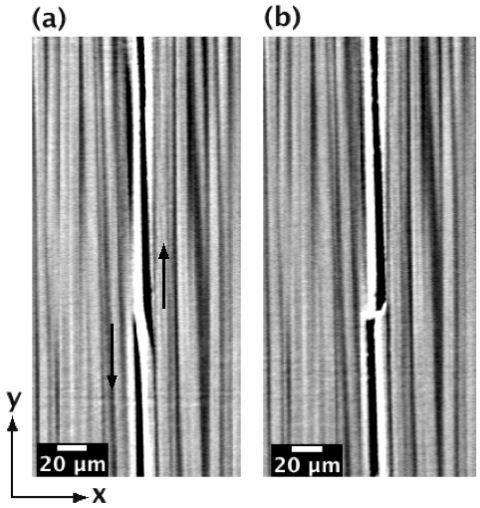

Figure 6. 2 - 0˚ ply split development along fibre interfaces at 50% UTS and 700 cycles (a), fibre breaks along 45˚ fracture plane at 800 cycles (b).

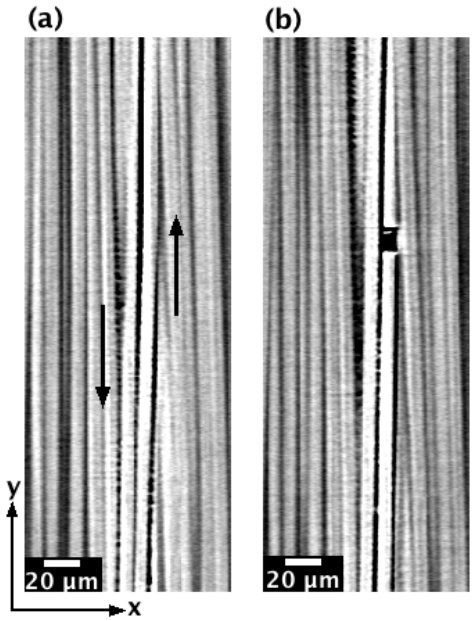

Figure 6. 3 - 0˚ ply split development along fibre interfaces at 50% UTS and 700 cycles (a), fibre breaks at 800 cycles (b).

The fibre is misaligned respect to the loading direction, and similarly to the case described in Figure 6.2, the 0˚ ply split propagation causes the fibre debonding from the matrix, Figure 6.3(a). The additional cycling determines the failure of the fibre, which according with the shear direction represented is due to a tensile event, Figure 6.3(b).

The mechanism identified to cause fibre failure along the split path is due to the presence of fibre bridges between the two flanks of the 0˚ ply split. In both cases, Figure 6.2 and 6.3, the fibre failure is associated with a wake process rather than a near-tip process. The comparison between Figure 6.2 and 6.3 shows that the fibre breaks due to bending/shear occur along a plane at 45˚ respect to the loading direction, while the fibre breaks due to a tensile event exhibits a fracture plane perpendicular to the loading direction. In addition, the comparison evidences differences in terms of distance between the fractured surfaces of the fibre for these two cases (bending/shear failure and tensile failure). In particular, the fractured surfaces of the fibre due to a bending/shear event (Figure 6.2(b)) are close each other, whereas these associated with the tensile failure (Figure 6.3(b)) exhibits a certain displacement, as the fibre is pulled. Considering that the damage is mode II dominated, this difference is directly related with the stress acting on the fibre, which resulted being in compression in the bending/shear failure and in tension in the tensile failure.

The analysis conducted has shown that the new fibre breaks detected along the 0˚ ply splits occur in 'new locations' and not in correspondence of pre-existent fibre breaks. The number of fibre failed in tension and in bending/shear along the 0˚ ply split is the same (37) at 700 cycles, while the additional fibre breaks obtained at 800 cycles are due mostly to bending/shear event (11) than tension (1). It should be noted that no fibre breaks in the bulk material (away from the crack) were observed in the particle-toughened system for the *in situ* conditions considered (i.e. 50% UTS, 700-800 cycles).

6.4 Fibre failure investigation at low load

This section focuses on the evaluation of fibre failure for a peak load of 30% UTS, at a high cycle count (10^6). Due to the fact that the applied load is relatively low the case of

a low number of cycles (10^3) was not directly included in the analysis because this latter condition showed only a few fibre breaks along the 0˚ ply split (11 along a single split) and no fibre break in the bulk composite. The fatigue case investigated (30% UTS and 10^6 cycles) has the aim to assess the effect of the high number of cycles on the fibre failure initiation. Results showed fibre fractures are only located along the 0˚ ply split propagation paths, as singlets and doublets (two adjacent fibre breaks), shown in Figure 6.4, and no fibre breaks were detected in the bulk composite. The shear direction associated with the 0˚ ply split in Figure 6.4 shows that the two fibre breaks are associated with a bending/shear event whereas the single fibre break closer to the notch is due to a tensile failure.

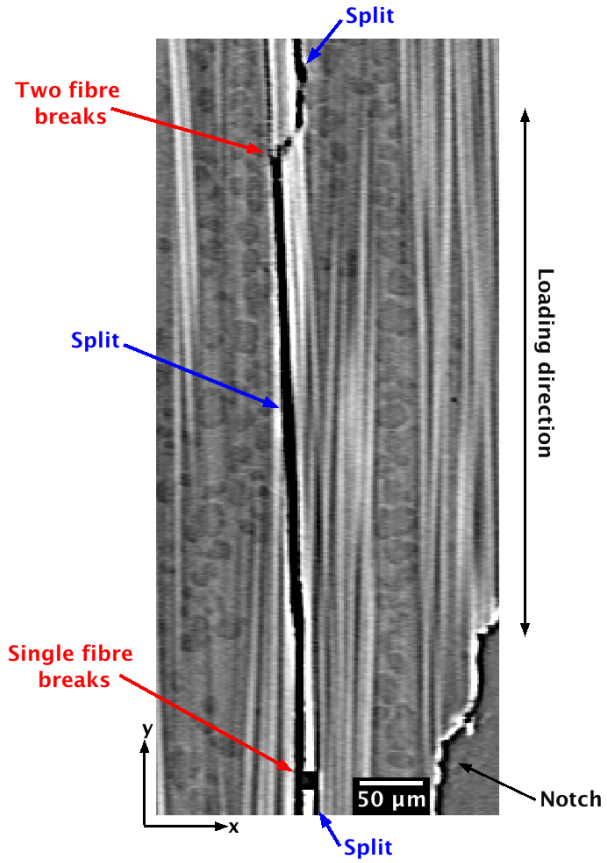

Figure 6. 4 – Fibres failure along the 0˚ ply split path for the peak of 30% UTS and 10^6 cycles.

The fibre breaks along the 0˚ ply splits apparently correspond with fibre bridging, even if it needs to be recognised that during *ex situ* tests is not possible to exactly determine whether the fibre breaks process is associated with a wake or near-tip process, or in

other words whether the mechanism of fibre breaks is the same of this one identified by the use of *in situ* tests. The total number of fibre failed detected along the 0˚ ply splits was 57.

The distribution of fibre break along the 0˚ ply split (fibre breaks density) has been evaluated dividing the total length of the split into intervals of 500 μm and counting the total number of fibre breaks within each interval. Therefore, the fibre breaks density was defined as the number of fibre breaks per (crack) unit length. Values reported represent the averages based on three counts.

Figure 6.5 shows the results obtained for the case of low load (30% UTS) and high number of cycles (10^6), where the split length detected was ~3 mm. The results highlight that the fibre break density increases with the distance away from the tip of the split towards to the notch, with no fibre breaks detected in the 1 mm nearest the split tip. The fibre breaks density rises to an almost constant value in the region 1 mm nearest to the split root at the notch. This is consistent with the fact that the fibre breaks detected also in the *ex situ* tests are also associated with bridging phenomenon along the wake of the crack.

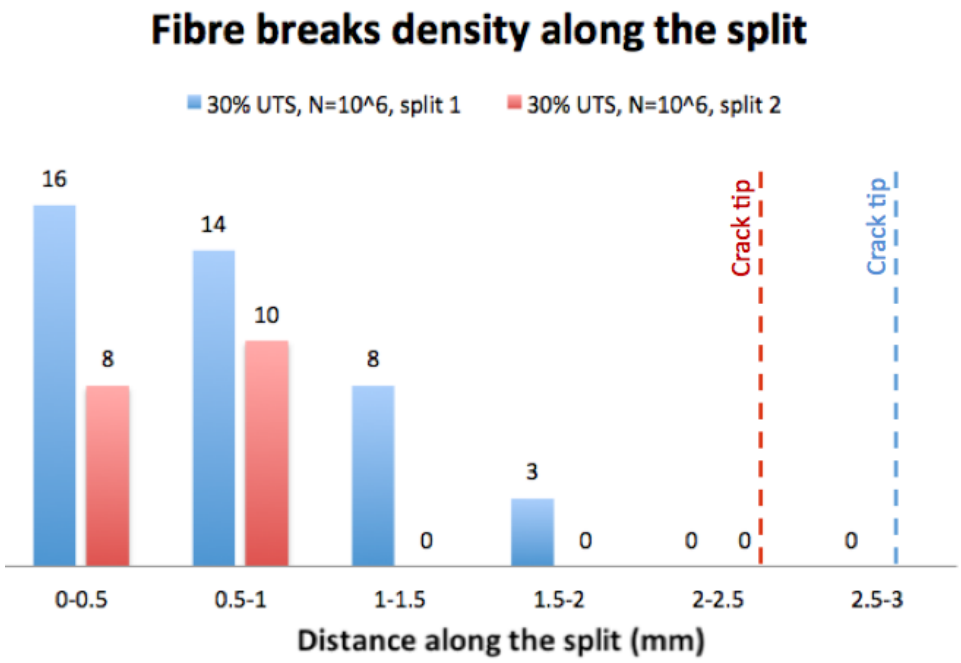

Figure 6. 5 – Fibre breaks density along the 0˚ ply splits for the peak load of 30% UTS and 10^6 cycles.

Figure 6.5 shows that the fibre breaks density along the '*split 1*' is slightly higher compared to that detected along '*split 2*'. Further analyses, conducted to investigate the different fibre breaks density within the same coupon, have shown that the similar crack length (Figure 6.5) also corresponds with a similar crack opening displacement for the two 0˚ ply splits considered. However, along the split with a lower fibre breaks density, different places (18) with fibre debonded from the matrix and bent were observed, almost all of them (17) located in the first half of the 0˚ ply split length, Figure 6.6.

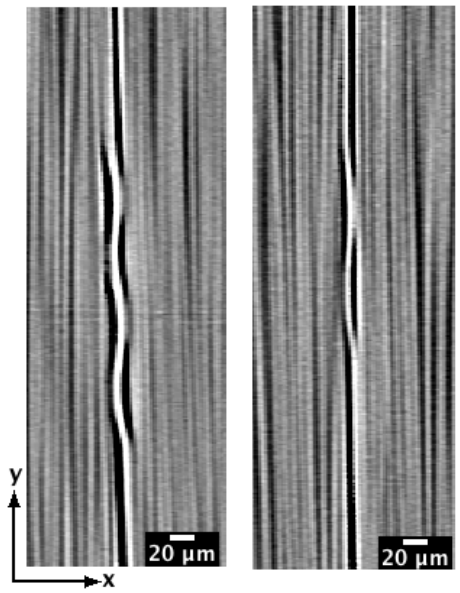

Figure 6. 6 – Fibre debonded and bent along the 0˚ ply split for a peak load of 30% UTS and 10^6 cycles.

In situ experiments have proved that this condition detected and reported in Figure 6.6, may represent the stage preceding the fibre breaks event, when fibres are debonded from the matrix due to the presence of the split (Figure 6.2 and 6.3). Therefore, the lower number of fibre breaks detected along the '*split 2',* Figure 6.5, is consistent with the behaviour detected along the '*split 1',* Figure 6.6, and additional cycles may determine the failure of the debonded and bent fibres.

No fibre breaks have been detected in the bulk composite, away from the notch or split surfaces (within the 0˚ plies). In keeping with a simple brittle behaviour, this suggests that the number of cycles alone is not responsible for creating fibre failure in the bulk composite, but this is mainly associated with the level of load, as explained in the following paragraphs.

6.5 Fibre failure investigation at intermediate load

The total number of fibre breaks detected in the notch region of the coupon tested at 50% UTS with 10^3 cycles was 148, of which 141 were located along the splits (average length of the 0˚ ply split of 2.5 mm).

6.5.1 Fibre failure along the 0˚ ply split

The application of a higher peak load does not necessarily correspond to a longer crack, since the number of cycles applied need to be considered at the same time. To understand if the increase in fibre breaks along the split path was genuinely associated with the increase of load and not other factors (*e.g.* the crack length), two cases with similar crack length, but different peak load were considered, and the fibre failure density along the splits measured. In particular, the case of low load (30% UTS) and high number of cycles (10^6) with the case of intermediate load (50% UTS) and low number of cycles (10^3) were compared, as shown in Figure 6.7.

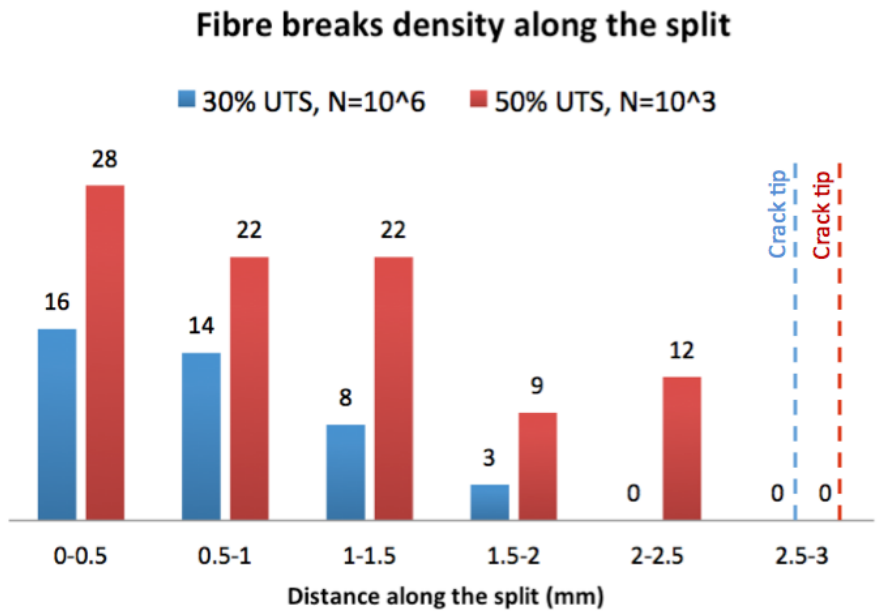

Figure 6. 7 – Fibre breaks density along the 0˚ ply split for the cases of: 30% UTS and 10^6 cycles, and 50% UTS with 10^3 cycles, taking into account splits with similar length.

The crack length detected (0˚ ply split) was similar, on the order of 3 mm for both cases. Figure 6.7 shows:

- The number of fibre breaks along the split path increases with the distance from the split tip for both cases. Therefore, the root of the crack exhibits the highest number of fibre failure along the split (fibre failure density).
- No fibre breaks have been detected in the interval (within 0.5 mm) behind the crack tip for both cases. This clearly indicates that fibre fracture is not caused by the local high stresses that would be expected near the crack tip as it encounters fibres.
- No fibre breaks were observed ahead of the crack tip.
- The comparison of the two load conditions (30% UTS with 10^6 cycles and 50% UTS at 10^3 cycles) shows that the crack length does not have a primary influence on the fibre failure density distribution along the split path, whereas the load level plays a significant role, resulting in higher values of fibre breaks for increasing peak loads at equivalent locations back from the split tip. This could be related to the fact that higher peak loads imply higher crack opening and crack shear displacement, and consequently fibres that bridge the two flanks of the split have more probability to fail at higher stress level. Details on COD and CSD plots are provided in Chapter 7.

Further analyses were conducted to confirm whether the crack length affects fibre breaks behaviour along the split, or in other words, to evaluate if a longer crack corresponds with a higher number of fibre breaks. Therefore, this case considers a longer crack associated with a low load (30% UTS and $N=10^6$) and a smaller crack corresponding to a higher load (50% UTS and $N=10^3$). Results are shown in Figure 6.8. The length of the split for the low load was of ~2.7 mm, while for the intermediate load a crack length of ~2 mm was detected. Nevertheless the smaller crack length for the intermediate load, the fibre breaks density is higher compared with that observed along the longer split associated with the low load. This confirms that, even if 50% UTS and a number of cycles of 10^3 does not represent a severe loading condition, the increase of load is the main factor that induces fibre failure along the split.

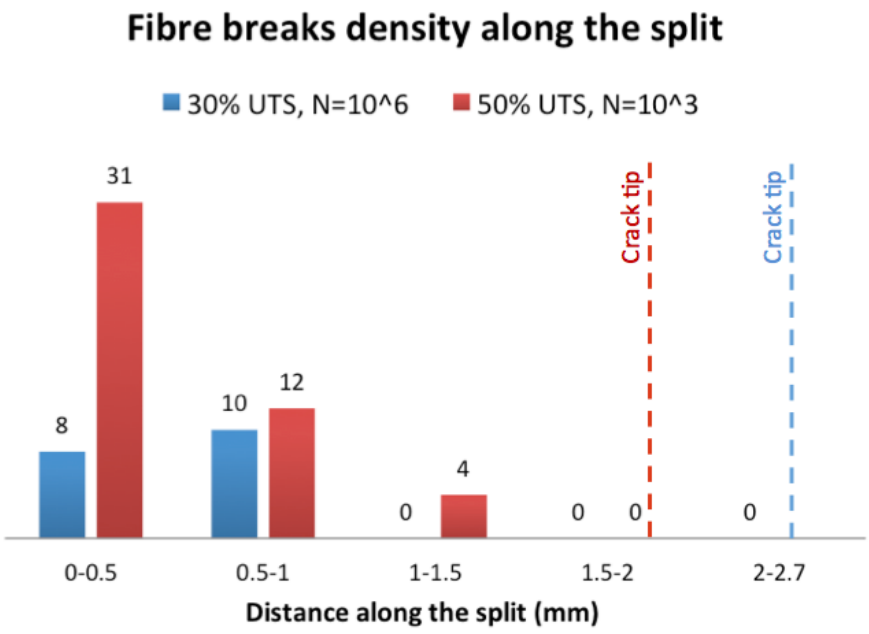

Figure 6. 8 – Fibre breaks density along the 0˚ ply split for the loading conditions of 30% UTS and 10^6 cycles, and 50% UTS with 10^3 cycles, taking into account splits with different lengths.

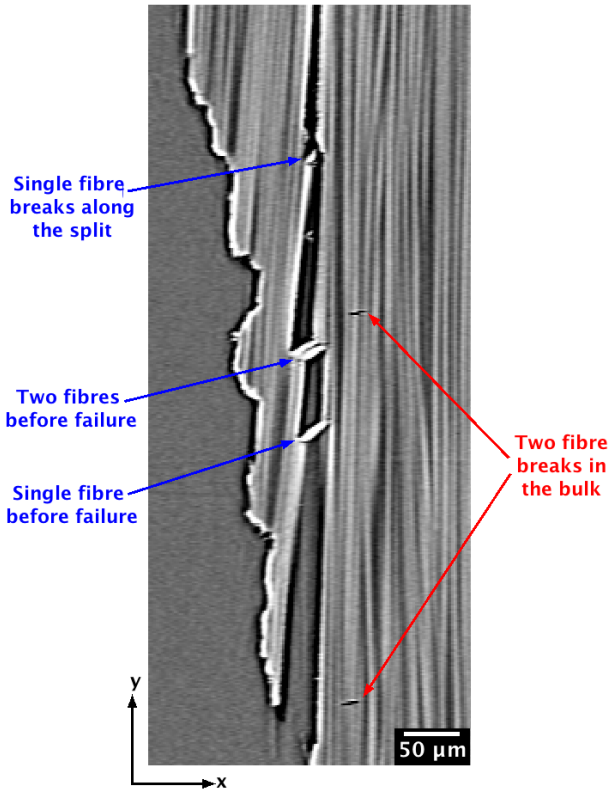

Figure 6. 9 – Fibre breaks along the split propagation and in the bulk composite for a peak load of 50% UTS and 10^3 cycles.

The specimen tested at the intermediate load exhibits fibre breaks in the bulk composite, even at low number of cycles, Figure 6.9 shows a cross section detected for 10^3 cycles, where the fibres follow the direction of the load (0˚ plies). The fibre breaks in the bulk, highlighted in Figure 6.9, are close to the 0˚ ply split. Bending/shear event drives the two adjacent fibres and the single fibre along the split path, which resulted being kinked. The shear direction may explain why these fibres do not break, the bridging rotates in an opening direction, forcing the crack to open further in a mode I, while the crack propagation is mode II dominated. The fact that these fibres are not completely separated may have negligible effect on the transfer load across the crack, and it is likely to be linked to local effect, such as the marginal matrix bonding that holds the two sides of the kinked fibres together.

The increase in the number of cycles, maintaining the same peak load of 50% UTS, leads to a higher number of fibre breaks along the split and also in the bulk composite. The total number of breaks counted along the splits was 325 within the notch region, while 18 breaks were detected in the bulk composite.

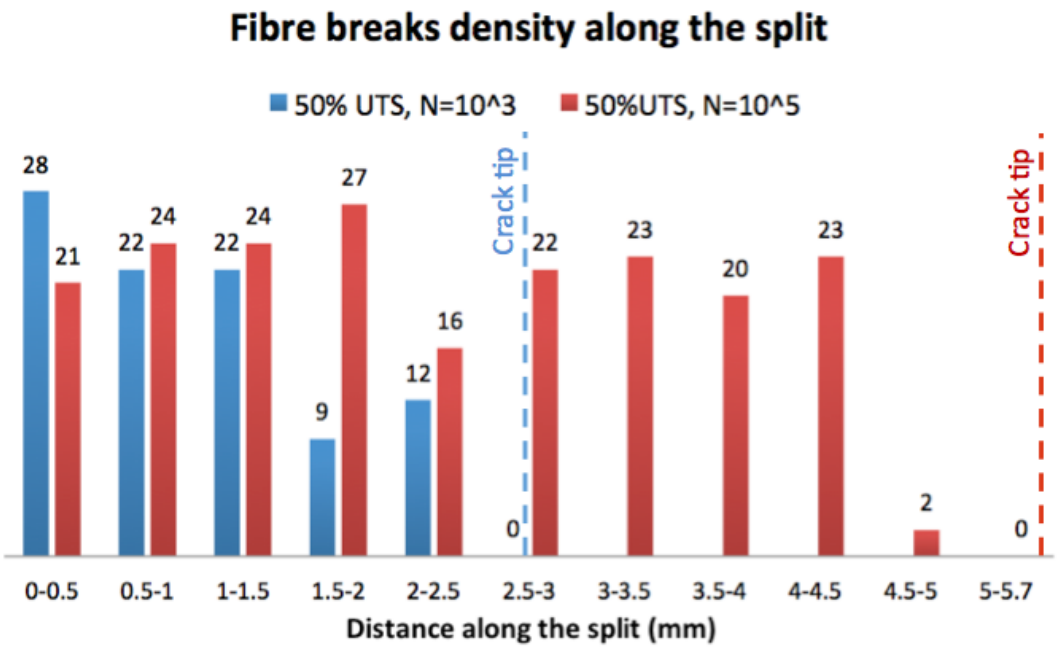

Figure 6. 10 - Fibre breaks density along the 0˚ ply split for 50% UTS and 10^3 cycles, and 50% UTS with 10^5 cycles.

The direct comparison at the intermediate load between the low number of cycles (10^3) and higher number of cycles (10^5) has shown a factor of two for the total number of fibre breaks (along the split and in the bulk composite). The fibre break density along the split for these two loading conditions (50% UTS with 10^3 and 10^5 cycles) is presented in Figure 6.10. As expected, while maintaining the same peak load, an increase of cycles results in an increase of crack length, with the length at 10^5 cycles being approximately double than that at 10^3 cycles.

The comparison of the two cycling conditions in Figure 6.10 highlights:

- The number of fibre breaks increases from the tip of the split towards to the root for the low number of cycles, whereas it exhibits a 'saturated behaviour' characterised by a constant number of fibre break density for the higher number of cycles. This latter case is characterised by a similar fibre failure density along almost all the split except for the interval immediately behind the crack tip (1.5 mm). This could be associated with: the local variation in the microstructure, the wake process mechanism of fibre failure, and higher values of crack shear displacement for higher number of cycles, sees Chapter 7 (Figure 7.14).
- The crack density converges to a similar saturation value at more than 1.5 mm behind the crack tip for both crack lengths.
- The breaks density detected in the first 1.5 mm of the split is similar for both cycling conditions. Therefore, the additional number of cycles does not contribute to develop more fibre fracture at the root of the split, but to create an increase of fibre breaks through all the crack length.
- No fibre breaks have been detected in the region immediately back (0.5 mm) from the crack tip, even for the case that showed a fibre fracture saturation along the crack length.

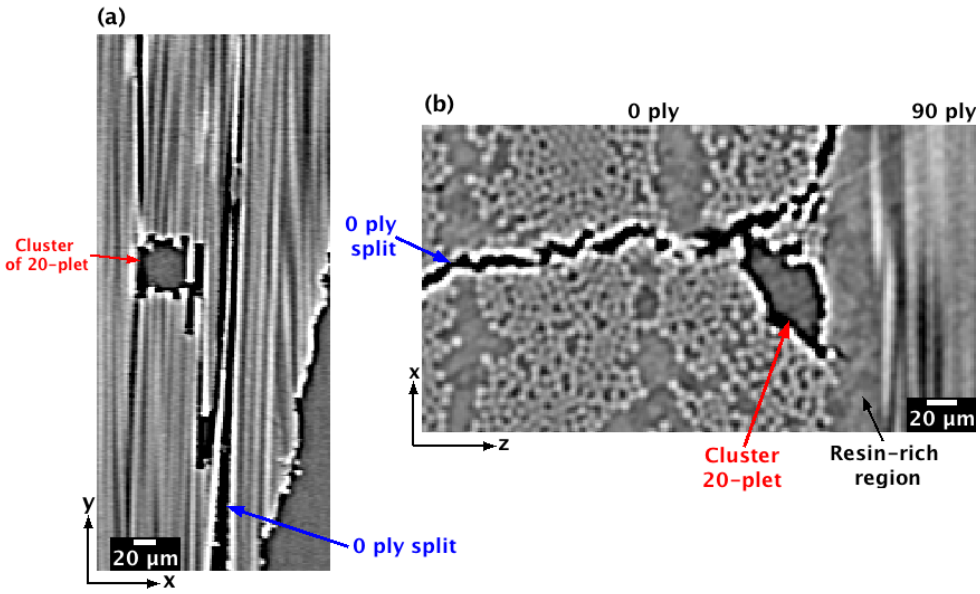

Figure 6. 11 – Cluster of 20 fibres breaks along the split for the case of 50% UTS and 10^5 cycles: (a) cross-section parallel and (b) perpendicular to the loading direction.

The increase of number of cycles from 10^3 to 10^5 causes more fibre-break cluster formation along the 0˚ ply split. The maximum number of adjacent fibre breaks along the split for the low number of cycles was 6, while 20 fibre breaks were observed for the higher number of cycles, where Figure 6.11(a) and 6.11(b) show the cross-section parallel and perpendicular to the loading direction respectively. Even if the 0˚ ply split taken into account in Figure 6.11 is only one, two parallel cracks along the loading direction are visible in Figure 6.11(a). This is due to the fact that the split in the region close to the interface, which exhibits delamination, is subjected to a 'bifurcation' (the main crack generates two separated branches). Consequently, two cracks propagate parallel along the loading direction for a ply thickness of ~50 µm and then interact with the delamination, Figure 6.11(b). The use of *ex situ* experiments does not allow to clarify whether the 20 fibre breaks, which are located in between the two branches of the split and delamination, are associated with the coalescence of damage or are due to a crack wake process, as observed in Figure 6.2 and 6.3. The location of the cluster observed at the low number of cycles (6 breaks) was at 1.8 mm from the tip of the crack with a length of ~3 mm, while the 20 breaks detected for the higher number of cycles is located close to the root of the crack, at ~5.5 mm from the crack tip for a crack length of ~6 mm.

6.5.2 Fibre failure in the bulk composite

Overall, only a few fibre breaks (7) were detected in the bulk composite in the specimen tested at 50% UTS and for the low number of cycles (10^3): two doublets (represented in Figure 6.9) and three singlets within the 0˚ plies distributed in a stochastic manner. The total number of fibre breaks observed in the bulk composite for 10^5 cycles (at 50% UTS) was 18 within the notch region, mostly of them as singlets (14), as shown in Figure 6.12(b), and a few as doublets (2), where multiple breaks appear as co-planar, Figure 6.12 (a).

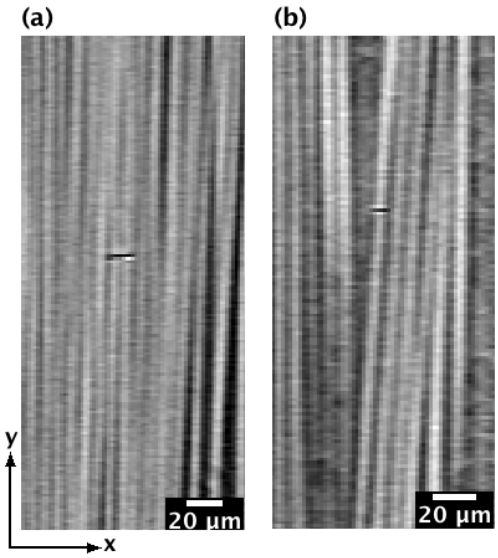

Figure 6. 12 – Fibre breaks detected at 50%UTS and 10^5 cycles: (a) a co-planar doublet, (b) a singlet corresponding to a misaligned fibre.

The distribution of fibre breaks in the bulk (0˚ plies) with respect to the position of the 0˚ ply splits is shown in Figure 6.13. As expected, fibre breaks in the bulk are located within the region bounded by the 0˚ ply splits and the delamination, where the stress is high due to the fact that the load-bearing cross-section is reduced by the presence of splits and delamination, which contribute to separate the 0˚ plies from the interface and the 90˚ plies (by delamination). This causes a reduction of the area of fibres in the 0˚ plies that have bearing capability (due to the 0˚ ply splits), as shown in the cross-section perpendicular to the loading direction in Figure 6.14; also clear visible from the 3D rendering of the damage modes, presented in Figure 4.4.

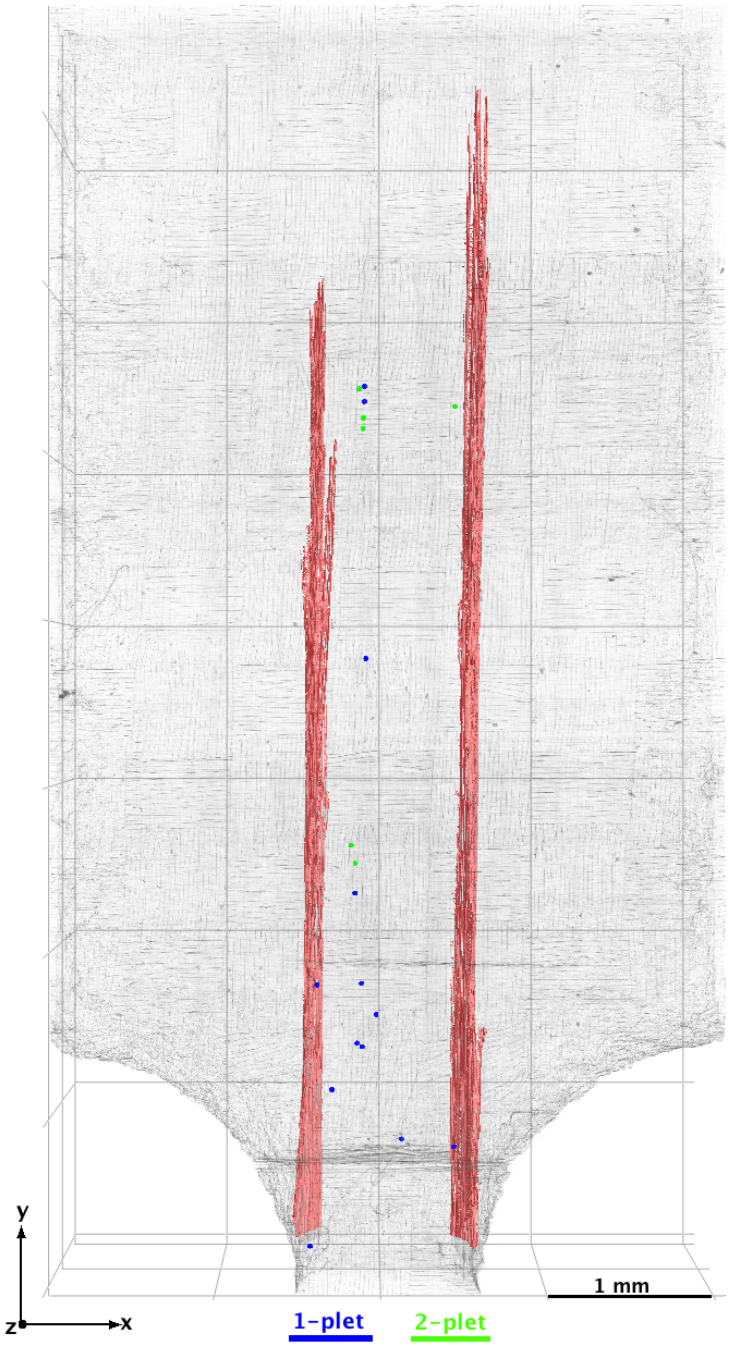

Figure 6. 13 – Fibre failure distribution in the bulk composite for the 50% UTS and 10^5 cycles.

In the region of interest delimited by the 0˚ ply splits and delamination, a small number of fibre breaks appear to be co-located with the larger cracks; and the majority appear to be distributed in a more stochastic manner, Figure 6.13. The number of fibre breaks in the bulk composite mentioned previously (18) is associated only with the 'notch region' to allow a direct comparison with the other cases taken into account (same volume and same location). However, Figure 6.13 shows the

distribution of all the fibre breaks observed in the bulk, including the volume defined by the total length of the 0˚ ply splits. For further details see the Appendix B.1.

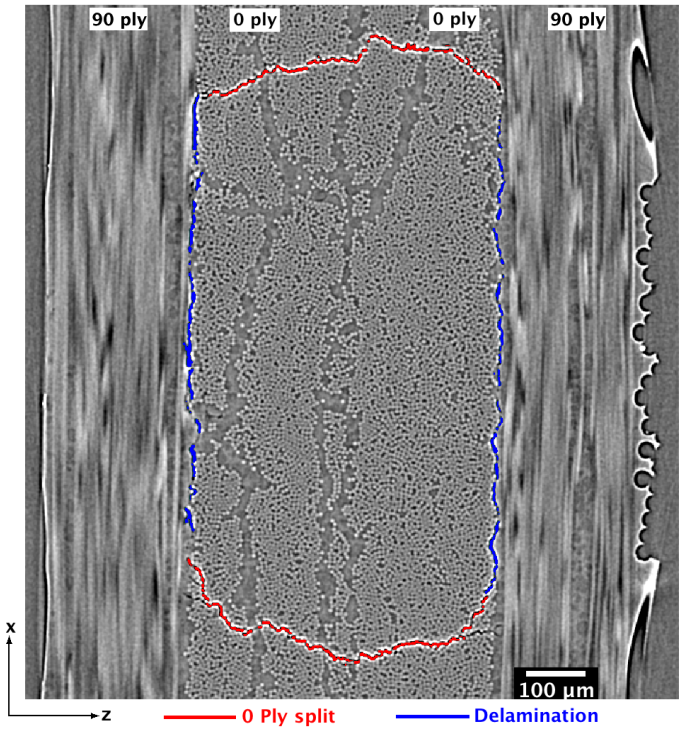

Figure 6. 14 - Cross-section perpendicular to the loading direction. The volume, where fibre breaks in the bulk composite are located, is delimited by 0˚ ply splits (in red) and delamination (in blue). The peak load associated with this case was of 50% UTS and the number of cycles of 10^5.

The presence of transverse ply cracks, two located in a symmetric position in the notch region (dark grey line in Figure 6.13 perpendicular to the loading direction), does not appear to have a major effect on fibre breaks locations. It is interesting to note from Figure 6.13 that not just the notch region, but also the volume between the 0˚ ply splits tips has fibre breaks in the bulk. However, most of the fibre breaks are singlets (represented in blue in Figure 6.13) and are located in the notch region, as defined in the Section 6.2. In order to have a visualization of the fibre breaks with respect to the thickness of the 0˚ plies, an additional perspective view is shown in the Appendix B.1. The conclusion that all the fibre breaks detected in the bulk composite are located in the volume delimited by splits, Figure 6.13 and 6.14, is consistent with the absence of fibre breaks in the region ahead of the split tips. This supports the assertion that fibre breaks away from the notch root are added progressively with cycling, i.e. with the increase in split length and delamination.

6.6 Fibre failure investigation at high load

The material behaviour described in this section is associated with a peak load of 70% UTS and a number of cycles of 10^3. A further increment in the number of cycles at this peak load was not considered due to the fact that the split length at 10^3 cycles was already on the order of 9 mm, and the next decade of cycling would have required more than four concatenated volumes (used in this context) to include all the damage in the field of view. At 10^3 cycles, the total number of fibre breaks detected in the notch region volume was 363, appreciably higher than the number of breaks observed at intermediate load (50% UTS) at 10^3 cycles (148). Particularly interesting is the fact that of these 363 fibre breaks, 70 are located in the bulk composite. The fibre break density along the 0˚ ply split length was measured following the procedure used for the previous cases described, and it is shown in Figure 6.15.

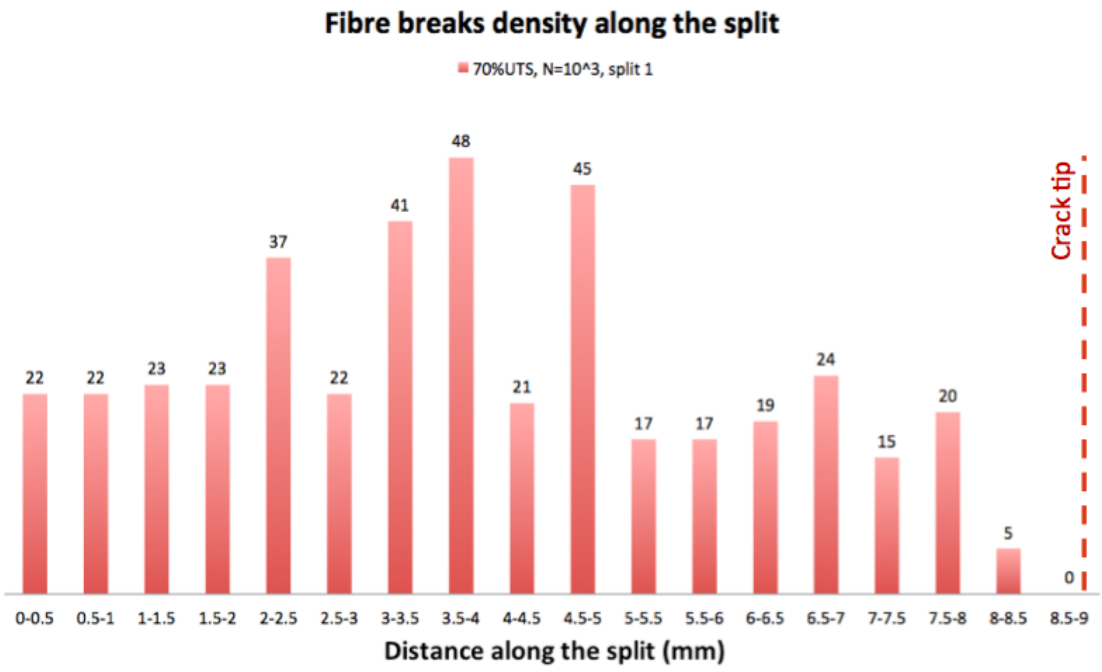

Figure 6. 15 - Fibre breaks density along a 0˚ ply split for the peak load of 70% UTS and 10^3 cycles.

The level of breaks reported is similar (~20/500µm) for each 500 µm interval considered along the split length, although significant variability is evident (up to double), particularly at the intermediate crack length positions. Further analyses

conducted on the intervals that exhibit the high values of fibre breaks density (>30) have correlated these peaks with the presence of multiple breaks (more than two) along the 0˚ ply split, as reported in the Table 6.1.

Table 6. 1 - Adjacent fibre breaks along the 0˚ ply split length.

Distance along the split [mm]	3-plet	4-plet	5-plet	6-plet	12-plet
2 - 2.5	-	1	-	-	-
3 – 3.5	2	-	-	-	-
3.5 - 4	-	1	1	-	-
4 – 4.5	-	-	-	1	1

A direct comparison with the case at intermediate load and 10^5 cycles, which also exhibits fibre break density saturation behaviour along the 0˚ ply split, is displayed in Figure 6.16. These two loading conditions are characterised by the same trend (from the root to the crack tip), but primarily by a comparable number of fibre breaks for each interval considered with the exception of the peaks in the break density at the higher load.

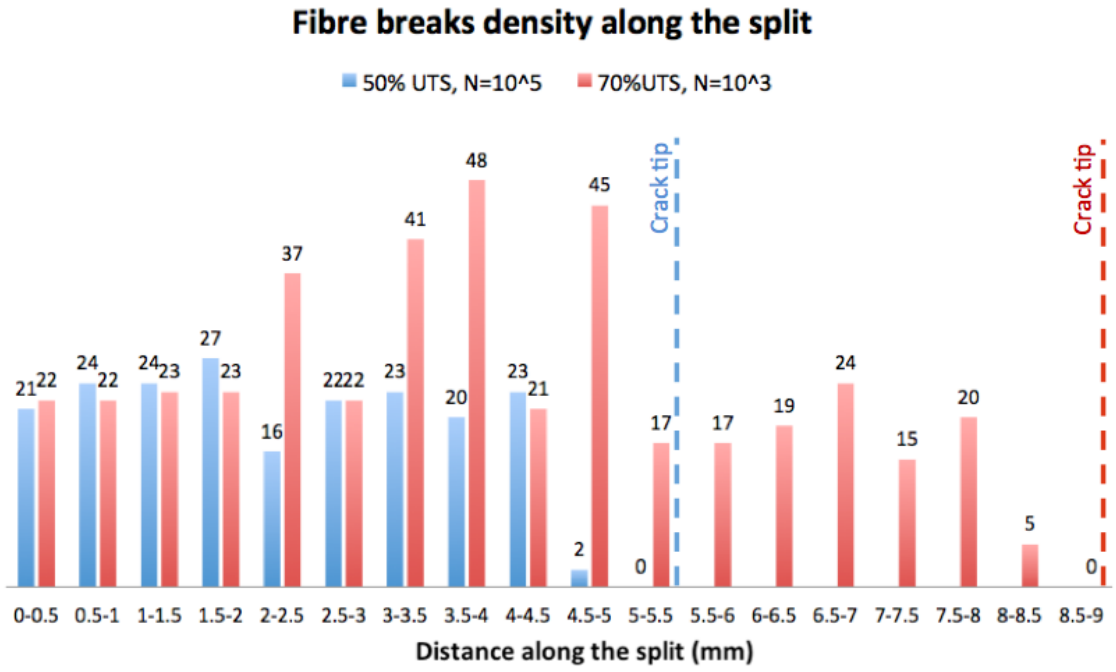

Figure 6. 16 - Fibre breaks density along the 0˚ ply split for (a) 50% UTS and 10^5 cycles, and (b) 70% UTS and 10^3 cycles.

The fact that at high peak load (>50% UTS) and/or number of cycles, the level of fibre breaks density is similar regardless the crack length is consistent with the fibre breaks dependency on the fibre distribution and with the wake process mechanism identified. The total number of fibre breaks detected in the bulk composite (within the notch region) for the high peak load at 10^3 cycles is appreciably higher than that detected at 50% UTS and 10^5 cycles (70 vs 18).

Table 6. 2 – Fibre breaks in the bulk composite for different loading conditions.

%UTS	N (Cycles)	1-plet	2-plet	3-plet	4-plet	5-plet
50	**10^3**	3	2	-	-	-
50	**10^5**	14	2	-	-	-
70	**10^3**	30	7	3	3	1

In addition, the maximum number of adjacent breaks in a cluster for the high load was a 5-plet, while the intermediate load resulted in only singlets and doublets. Table 6.2 reports a summary of the fibre breaks observed in the bulk composite within the notch region for the different loading conditions considered, showing clearly a tendency for cluster formation at the higher load. A three-dimensional map with the distribution of fibre breaks in the bulk is provided in Figure 6.17, which reports the notch region (in dark grey volume) concatenated with an additional volume (in light grey volume). The remaining volume, located up to 6 mm from the middle of the notch, was not included in Figure 6.17 to allow for easier visualisation. However, the analysis conducted has shown only two single fibre breaks in the bulk located in this distant region, with the majority of the breaks lying in the volume presented in Figure 6.17. The comparison between Figure 6.17 and Figure 6.13 highlights an interesting aspect regarding the accumulation of fibre breaks. While the intermediate load results in an apparently scattered distribution (Figure 6.13), the high load exhibits a fibre breaks accumulation mainly in two regions: (i) the notch region located in the first millimetre from the middle of the notch, and (ii) an intermediate region, located at 2-4 mm from the middle of the notch. Further analysis has been conducted to investigate the two locations characterised by a higher fibre breaks density in the bulk. The region

immediately between the notches is delimited by the 0˚ ply splits and by the presence of fully opened transverse ply cracks.

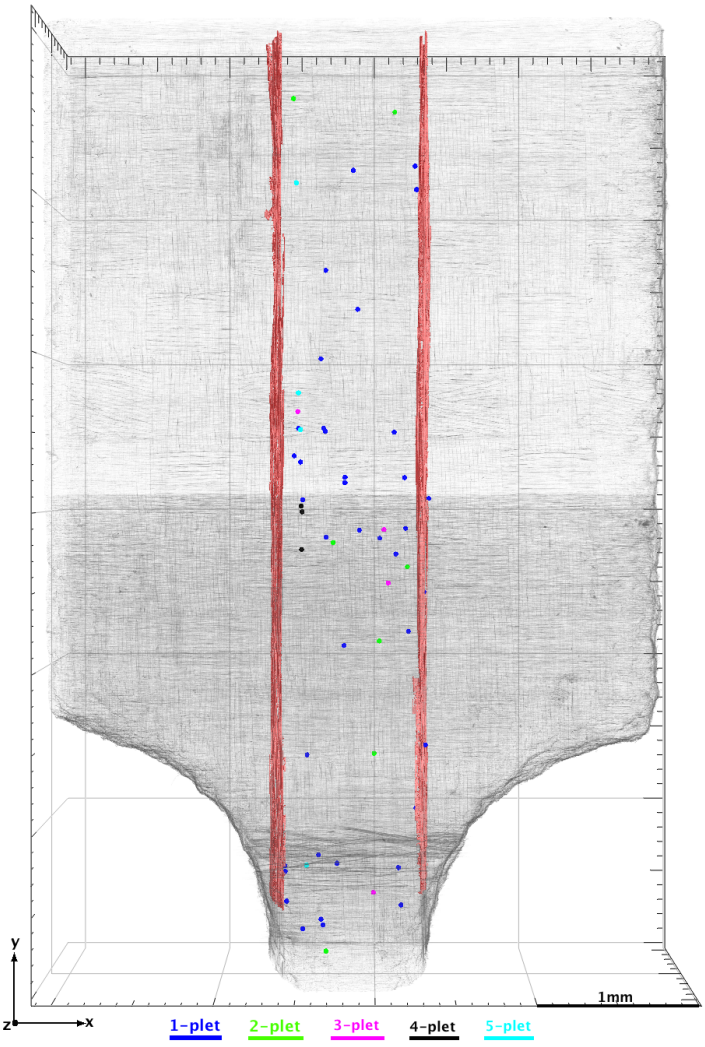

Figure 6. 17 - Fibre failure distribution in the bulk composite for the 70% UTS and 10^3 cycles.

The intermediate region is characterised by a reduction in cross-sectional area due to 0˚ ply splits and delamination, as also shown in Figure 6.14. Both damage modes (0˚ ply splits and delamination) isolated the 0˚ plies region from the middle of the notch up to the top of the volume presented in Figure 6.17. Therefore, it is likely that the observed distribution of fibre breaks could be also associated to a stochastic process. Clusters of breaks detected in the bulk are co-planar and the 4-plet and 5-plet, which represent the highest number of adjacent fibre detected, are close to the ply interface, as is visible from the perspective view provided in Appendix B.2.

6.7 Comparison with quasi-static case

The evaluation of fibre breaks in the quasi-static case [8] has been taken into account for a case of 80% UTS to assess whether the fibre breaks detected in the fatigue cases are influenced by the cycling process and not by the initial quasi-static (first cycle) load alone. This in some way is already indicated by the fact that for the same peak load, an increase of the number of cycles corresponds with higher number of fibre breaks, as observed at 50% UTS levels (Figure 6.10). However, comparison with the quasi-static case may further give a confirmation, and possible insights regarding the underlying processes. The total number of fibre breaks detected in the quasi-static tensile case was 124 with 14 breaks in the bulk composite. The volume considered was identical to that used to count the fibre breaks in the fatigue case, in terms of dimensions and location, 3 mm away from the centre line of the notch.

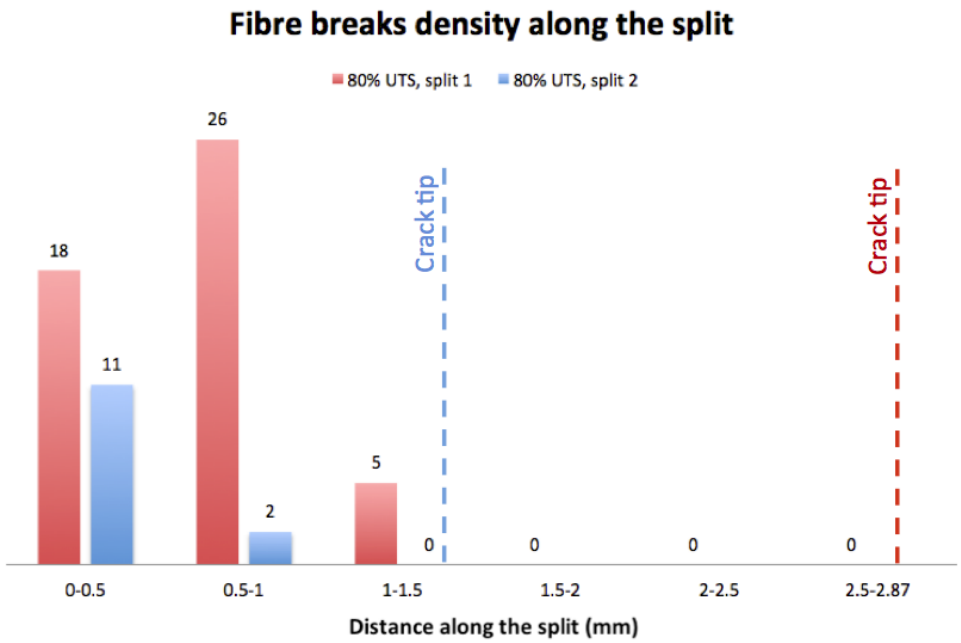

Figure 6. 18 – Fibre breaks density along 0˚ ply splits located on the same notch side for the tensile load of 80% UTS.

The fibre failure break density along the 0˚ ply split was calculated following the same procedure as used for the fatigue cases, and the results are reported in Figure 6.18. The density of fibre breaks increases from the tip of the 0˚ ply split towards the root,

showing higher values at the root for the longer split. In addition, this latter does not exhibit any fibre breaks for the 1.5 mm nearest the crack tip, which represents half of the crack length. The comparison of fatigue cases with the quasi-static case at 80% UTS has shown similarities and differences:

- The fibre breaks density along the 0˚ ply split shows a similar trend between the quasi-static case (Figure 6.18), the fatigue case at low peak load (Figure 6.5) and the intermediate peak load with low number cycles (Figure 6.7 and 6.8). However, when higher peak loads and/or number of cycles were considered (Figure 6.10, 6.16) the fibre breaks density exhibits a different trend, with a saturation of fibre breaks along the split for the fatigue cases. Therefore, considering an equivalent peak load for the quasi-static case (80% UTS), a different fibre breaks behaviour along the 0˚ ply split respect to that observed at high peak load for fatigue case (70% UTS) is detected.
- Both loading conditions (quasi-static and fatigue) do not exhibit fibre breaks in the immediate region back to the crack tip, suggesting that fibre failure along the 0˚ ply split is a wake process rather than a near tip process for both loading conditions. However, one of the quasi-static plot (Figure 6.18) does not present any fibre breaks for half of the crack length back from the split tip (1.5 mm); while for the majority of the fatigue cases considered this is valid only in the last 0.5 mm behind the crack tip. The only exception among fatigue cases is represented by low the peak load (30% UTS) as it is possible to see from Figure 6.5, which do not show fibre breaks 1 mm back from the crack tip.
- The level of fibre breaks in the wake (~20/25) is in the same order between quasi-static (Figure 6.18) and fatigue cases (Figure 6.10, 6.16). This could be consistent with the number of bridges forming being a function of the fibre distribution pattern.

The distribution of the fibre breaks in the bulk composite for the quasi-static case at 80% UTS is shown in Figure 6.19. Even though the maximum peak load considered is higher than the fatigue cases, the number of fibre breaks is lower. This is consistent with the fact that observed fibre breaks for the fatigue cases are associated with the cycling process and not with the initial quasi-static load. The type of fibre breaks in quasi-static loading are limited to singlets and doublets, in equal proportion; while the fatigue

cases showed a higher number of single fibre breaks respect to the number of multiple breaks. The majority of fibre breaks in the quasi-static case are located close to the 0˚ ply split and to the ply interface, see Appendix B.3.

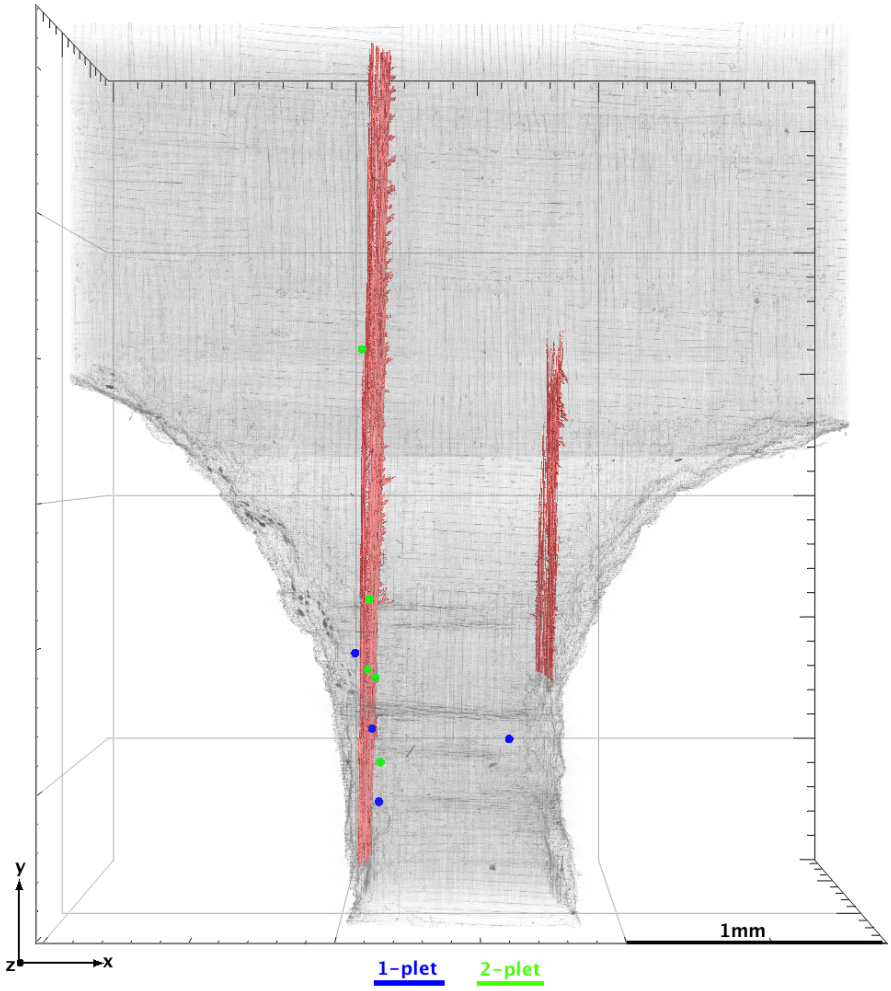

Figure 6. 19 - Fibre failure distribution in the bulk composite at a quasi-static load of 80% UTS.

The mechanisms that lead to fibre failure in the bulk for the quasi-static case therefore appear somewhat different (for this load level) than those identified for fatigue loading, attributable to the fact that no delamination is present in the quasi-static, which consequently does not result in isolation of the 0˚ plies, as shown for the fatigue cases.

6.8 Summary on fibre failure under fatigue

This section contains a summary of the fibre breaks detected for the different loading conditions considered, as shown in Table 6.3. The notch region is represented by a length of ~3 mm from the middle-notch along one side, while the total volume is referred to the volume defined by the length of the 0˚ ply splits.

Table 6. 3 – Summary of fibre breaks detected under fatigue loading.

		Breaks along 0˚ ply split		**Breaks in the bulk composite**	
%UTS	**N (Cycles)**	Notch region	Total volume	Notch region	Total volume
30	**10^6**	57	57	-	-
50	**10^3**	148	148	7	7
50	**10^5**	325	542	18	33
70	**10^3**	363	700	70	107

Damage quantification in terms of crack opening and crack shear displacement, presented in Chapter 7, have provided additional information to the analysis of fibre failure along the 0˚ ply splits. According with the results obtained, a schematic representation is reported in Figure 6.20, which links the crack opening and crack shear displacement with the fibre breaks density detected along the 0˚ ply splits. The schematic representation in Figure 6.20 does not refer to any single/specific case, but has the aim to summarise the overall trend detected. The two loading conditions reported, highlighted with a different colour (red and blue), are both associated with a steady-state growth (COD does not depend on the crack length). The correspondent CSD is drawn with the same colour to facilitate the identification. CODs and CSDs graphs are plotted as function of the 0˚ ply split length, starting from the root of the 0˚ ply split (zero) up to the crack tip. The plot of the COD at the root, reported as dashed lines, highlights the possibility to have a decreasing or constant trend, further details on this aspect are described in Chapter 7.

Figure 6.20 includes two main cases: the increase of peak load for a fixed number of cycles and the increase of number of cycles for a fixed peak load.

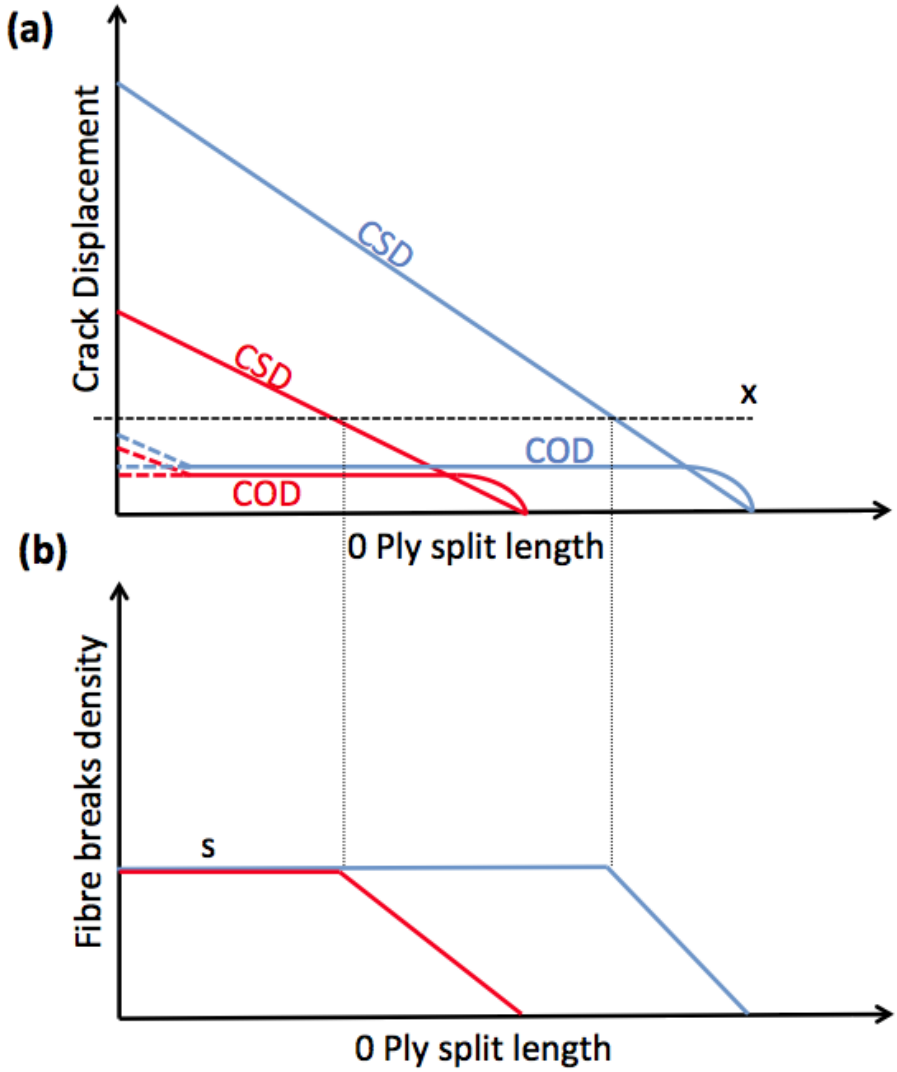

Figure 6. 20 – Schematic of the crack opening and crack shear displacement associated with an increase of peak load or an increase of number of cycles (a), and of the corresponding fibre breaks density along the 0˚ ply split (b).

The first case is represented by the increase of the peak load (see Chapter 7, Figure 7.7 and 7.10), which results mainly in an increase of crack shear displacement (damage propagation is mode II dominated). The schematic provided in Figure 6.20(a) shows similar crack opening displacement when peak load higher than 50% UTS are applied, in this context the blue line is the representation of a higher peak load. The crack shear displacement increases with the increase of the load and of the crack length, moving

from the red line to the blue line. For a fixed crack shear displacement '*x*' the trend of the fibre breaks density obtained is provided in Figure 6.20(b) for the two cases considered. The fibre breaks density plot, shown in Figure 6.20(b), shows a change of slope in correspondence of the intersection between the fixed crack shear displacement 'x' and the CSD curve. This latter point represents the end of the fibre breaks saturation and the beginning of a decreasing trend towards the crack tip. The level of fibre breaks saturation identified in the graph in Figure 6.20(b) with '*s*' is presumably dependent on the microstructure (*i.e.* fibre distribution).

The application of relatively low peak loads (<50% UTS), such as the case of 30% UTS, determines lower CSD compared with 50% UTS. This is consistent with the decreasing behaviour of fibre breaks density detected along all the 0˚ ply split from the root towards to the tip, instead than having a saturation (constant) trend and then a decreasing behaviour. According with the schematisation reported in Figure 6.20(a), in this case there is no intersection between the fixed crack shear displacement 'x' and the CSD for low peak loads (<50% UTS), because the CSD curve is below the fixed value 'x'. Therefore, the fibre breaks density shows a decreasing behaviour form the root towards to the tip of the crack, which corresponds with the last part of the plot reported in Figure 6.20(b).

The second case considered is represented by the increase of number of cycles (blue line) for a fixed peak load (>50% UTS). The increase of number of cycles showed an increase of crack length (moving from red line to the blue line), but the COD values are comparable for a fixed peak load. However, the CSD associated with the increase of number of cycles (blue line) is higher than the lower cycles (red line). This is consistent with the experimental observations where the increase of number of cycles leads to exhibits a similar COD and an increase of CSD with the increase of number of cycles (see Chapter 7, Figure 7.12 and 7.14).

A similar behaviour of that observed for a fixed number of cycles and an increase of peak load has been detected when the peak load is fixed and the number of cycles increases, Figure 6.20(a). Therefore, the considerations done for the previous case (fixed number of cycles and increasing peak load) in terms of fibre breaks density are also valid in this context (fixed peak load and increasing number of cycles), as shown in Figure 6.20 (b).

6.9 Conclusions

The use of synchrotron radiation computed tomography revealed novel insights on fibre breaks under fatigue loading that was not possible to achieve by the use of traditional techniques, such as electron microscope or other non-destructive methods. *In situ* and *ex situ* fatigue experiments have been used in this study to investigate fibre failure micromechanisms and to quantify fibre breaks.

- The scenario of loading conditions investigated has shown fibre breaks along the 0˚ ply split paths and in the bulk composite. Even if fibre breaks along the splits were observed also at low load (30% UTS), the breaks in the bulk composite were detected only in correspondence of peak loads higher than 50% UTS.
- The micromechanism of fibre failure along the 0˚ ply split path is represented by fibre bridging the flanks of the split during the damage propagation. The fibres involved can fail due to bending/shear or tensile events, and the process identified is a wake-process rather than a near-tip process. This is consistent with the fact that the fibre breaks density along the split length increases from the tip towards the root of the crack, and the region ahead and immediately behind the crack tip does not show fibre failure.
- A level of saturation of the fibre breaks density has been detected for peak loads higher than 50% UTS. This might be related with the microstructure (probability to have bridging fibre along the 0˚ ply split path). Similarly to the increase of peak load, the increase of cycles for load levels higher than 50% UTS exhibits fibre breaks density saturation in the region behind the crack tip.
- The number of fibre breaks observed in the bulk composite is directly connected with the peak load and the number of cycles; increasing when higher peak load are applied (such as 70% UTS) for a fixed number of cycles, and when the cycles increase for a fixed peak load (>50% UTS). Particular interesting is the fact that the high peak load considered (70% UTS) is characterised by the formation of cluster (multiple breaks) up to 5, while the intermediate load (50% UTS) shows clusters with only two fibre breaks.

- The fibres breaks in the bulk are located not exclusively in the notch region, but in the all volume defined by the presence of the 0˚ ply splits and delamination. Therefore, based on this the analysis of fibre breaks needs to be conducted on a broader volume than the geometrical notch region.
- The comparison with an equivalent quasi-static case (80% UTS) has shown significantly lower number of fibre breaks (along the splits and in the bulk) respect to the fatigue case with a similar peak load (70 UTS and 10^3 cycles). No fibre breaks have been detected in the region back from the crack tip also for the quasi-static case (along a longer length compared with the fatigue cases). The level of fibre break density at the root of the split is similar to the fatigue cases, even without any saturation behaviour observed at this load.

6.10 References

[1] B.S. Blassiau, A. Thionnet, and A.R. Bunsell, "Damage accumulation processes and life prediction in unidirectional composites," *Proceedings of Royal Society A*, vol. 463, pp. 1135-1152, 2007.

[2] Rosen B.W., "Tensile failure of fibrous composites," *AIAA Journal* , vol. 2, pp. 1985-1991, 1964.

[3] C. Zweben and B.W. Rosen, "A statistical theory of material strength with application to composite materials," *Journal of the Mechanics and Physics of Solids*, vol. 18, pp. 189-206, 1970.

[4] I.J. Beyerlein and S.L. Phoenix, "Statistics for the strength and size effects of microcomposites with four carbon fibre in epoxy resin," *Composites Science and Technology*, vol. 56, pp. 75-92, 1996.

[5] S. Mahesh, S.L. Phoenix, and I.J. Beyerlein, "Strength distribution and size effect for 2D and 3D composites with Weibull fibers in an elastic matrix," *International Journal of Fracture*, vol. 115, pp. 41-85, 2002.

[6] Y. Zhou, M.A. Baseer, H. Mahfuz, and S. Jeelani, "Statistical analysis on the fatigue strength distribution of T700 carbon fiber," *Composites Science and Technology*, vol. 66, pp. 2100-2106, 2006.

[7] A.E. Scott, M. Mavrogordato, P. Wright, I. Sinclair, and S.M. Spearing, "In situ fibre fracture measurement in carbon-epoxy laminates using high resolution computed

tomography," *Composites Science and Technologies*, vol. 71, pp. 1471-1477, 2011.

[8] P. Wright and M.N. Mavrogordato, Private Communications, 2009, Data from European Synchrotron Radiation Facility.

Appendix B

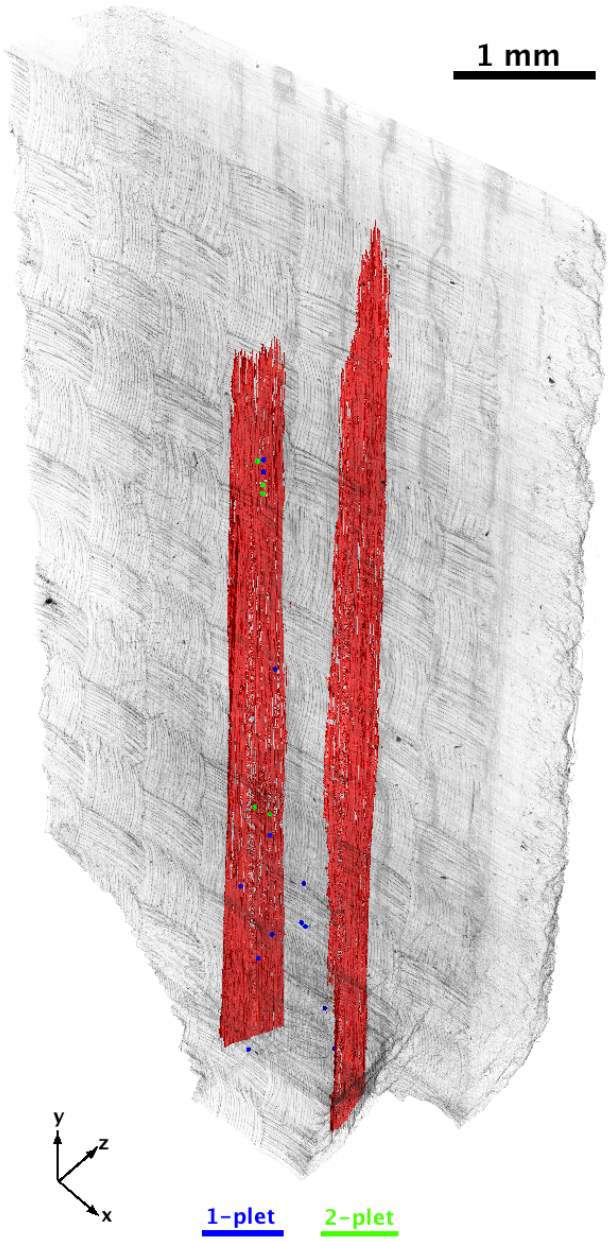

Figure B. 1 - Fibre failure distribution in the bulk composite for the 50% UTS and 10^5 cycles considering the entire damaged volume.

Table B. 1 – Fibre breaks detected in the bulk composite for a peak load of 50% UTS and 10^5 cycles.

%UTS	N (Cycles)	1-plet	2-plet	3-plet	4-plet	5-plet
50	**10^5**	21	6	-	-	-

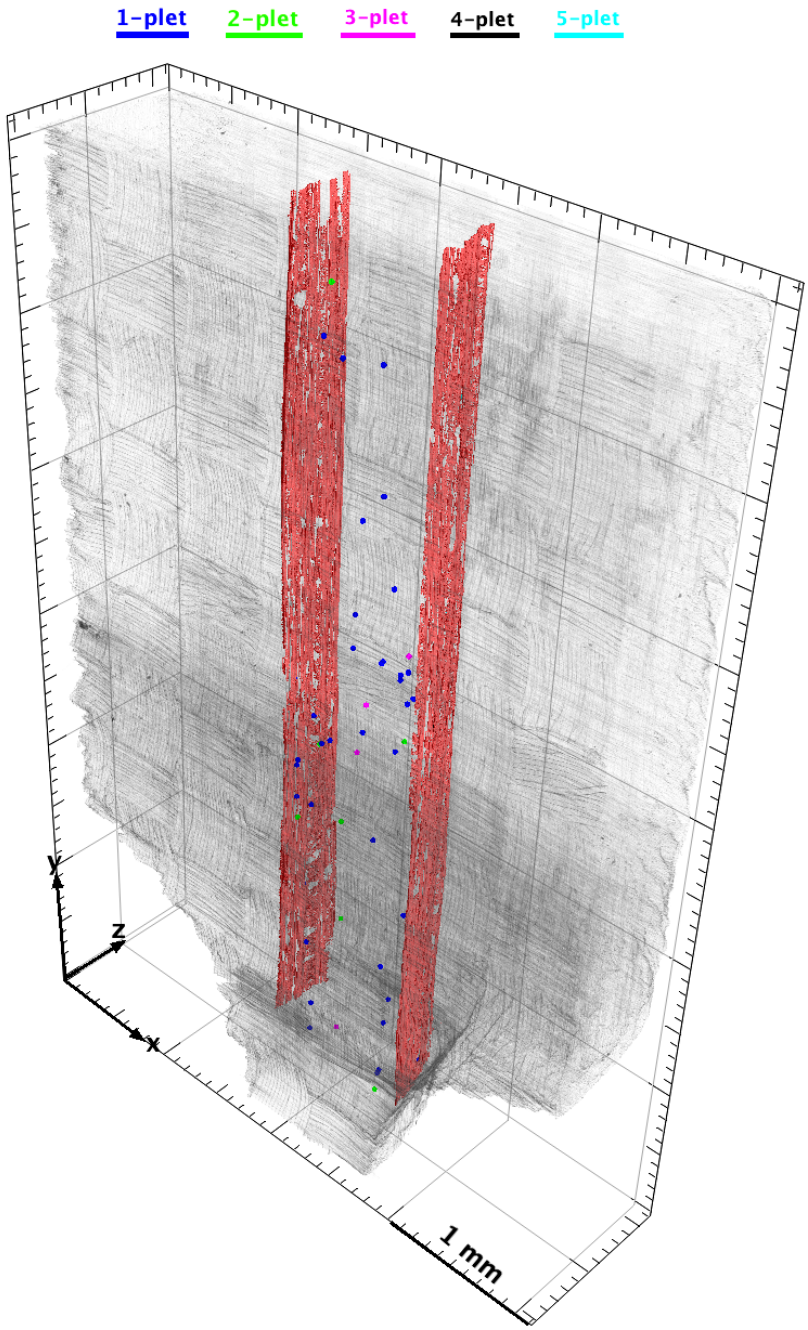

Figure B. 2 - Fibre failure distribution in the bulk composite for the 70% UTS and 10^3 cycles considering the entire damaged volume.

Table B. 2 - Fibre breaks detected in the bulk composite for a peak load of 70% UTS and 10^3 cycles.

%UTS	N (Cycles)	1-plet	2-plet	3-plet	4-plet	5-plet
70	**10^3**	45	9	4	3	4

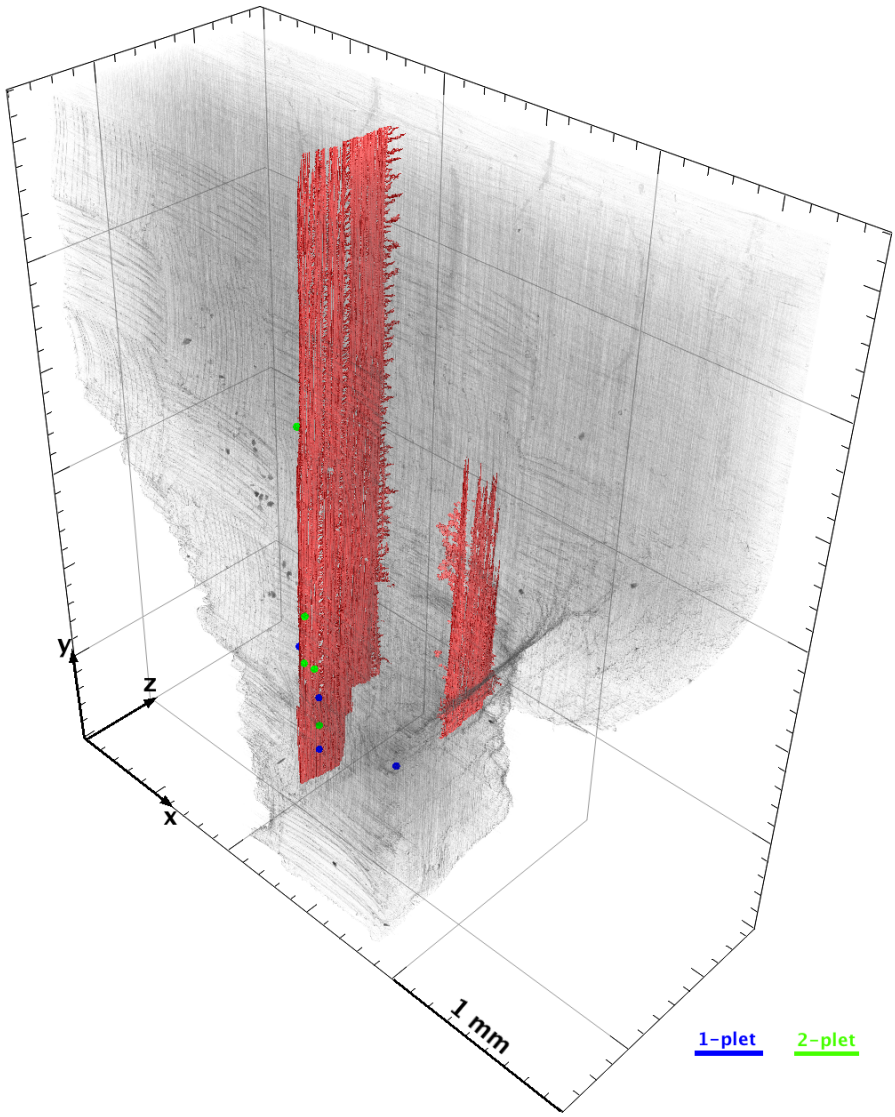

Figure B. 3 - Fibre failure distribution in the bulk composite for the tensile load of 80% UTS considering the entire damaged volume.

Table B. 3 - Fibre breaks detected in the bulk composite for a quasi-static load of 80% UTS.

%UTS	1-plet	2-plet	3-plet	4-plet	5-plet
80	4	5	-	-	-

Chapter 7

The effect of load cycling on material degradation

This chapter provides a quantification of the effect of fatigue loading on the particle-toughened (M21/T700) material degradation. The influence of peak load, number of cycles, crack length, local ply structure, and damage interaction modes on the crack opening and crack shear displacement (COD and CSD) is assessed and discussed. Results obtained for the fatigue cases have been compared with quasi-static behaviour reported in the literature, highlighting similarities and differences.

The analysis was conducted using ex situ *experiments that are characterised by the same voxel resolution (1.6 µm), the same geometry and the same scan location. All the measurements presented (COD and CSD) are referred to the full length of the 0˚ ply splits. In particular for each specific case multiple concatenated volumes were used (when required) to include all the damage modes in the field of view.*

The COD and CSD quantification provided represents valuable experimental results to calibrate and validate future modelling on fatigue. Understanding the micromechanisms that lead to a specific behaviour and relating these to the results is of fundamental importance. This is the main aim of this chapter, along with contrast and comparison to observations from the literature.

7.1 Preliminary considerations

Following the methodology explained in Chapter 3, the line plots of the crack opening displacements based on the corresponding COD maps have been calculated. As described in Section 3.6.3 the implemented code allows the determination of the COD along and across 0˚ ply splits, although in this section the focus is mainly on the COD along the 0˚ ply split. Therefore, the 0˚ ply split widths have been divided into five intervals, and for each interval the average COD values along the position of the crack were estimated, Figure 7.1. Similarly, when the average COD values across the 0˚ ply splits are estimated, the split was divided in multiple intervals along its length. Due to the fact that the visualisation of all five line plots together (Figure 7.1) for each specific case considered (intervals 1-5) could result in a confusing presentation, especially when two loading conditions are compared to each other; a representative line plot is reported for each case by averaging the COD in the region of interest taken into account.

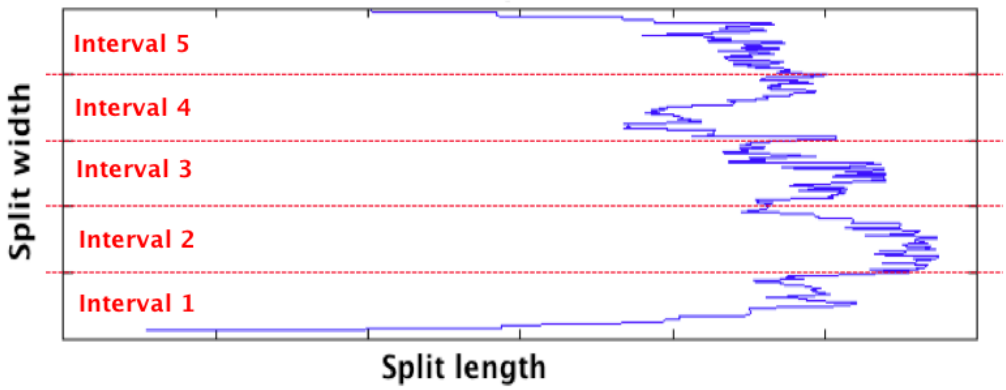

Figure 7. 1 – Schematic of the intervals along the 0˚ ply split width to assess the average COD lines along the crack.

The CODs related to the intervals corresponding to the ply interfaces (intervals one and five in the schematic in Figure 7.1) could be affected by the presence of the interface itself, which contains resin rich regions that have the effect of constraining the crack, as also explained in the Chapter 4 and Chapter 5. Alternatively, another region of the 0˚ plies that strongly affected the split propagation is represented by the

characteristic resin rich region that connects the two central 0˚ plies for the layups used here (i.e. roughly located in the middle of the coupon thickness, interval 3 in Figure 7.1). As described in Chapter 4 and 5, this region shows the formation of echelon cracks, with consequently high apparent local COD values.

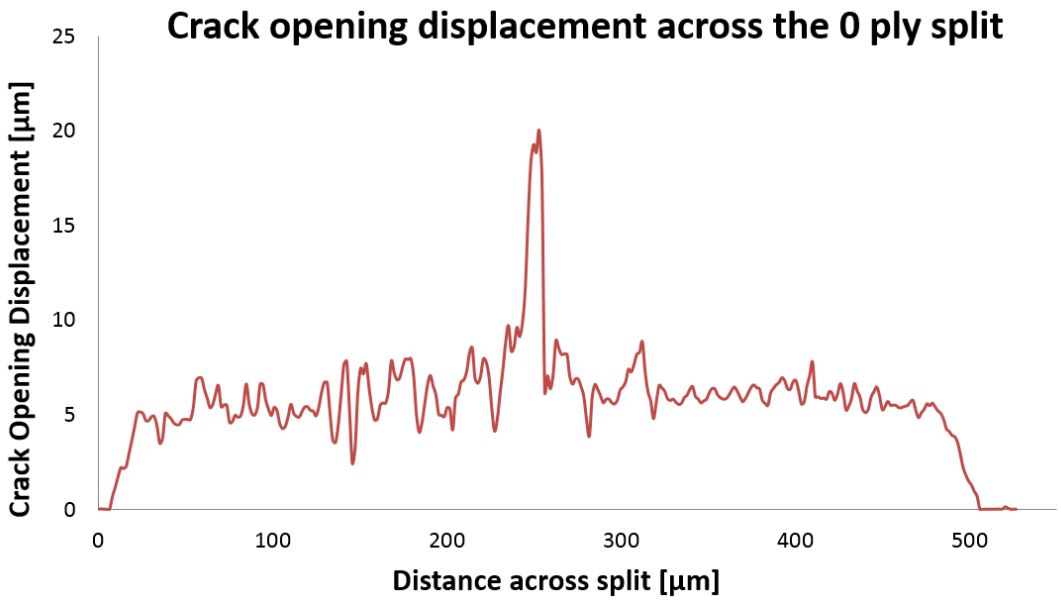

Figure 7. 2 – Crack opening displacement across the 0˚ ply split for the peak load of 50% UTS and 10^3 cycles.

One of the potential consequences in terms of crack opening displacement when one of these intervals (intervals 1-5 in Figure 7.1) is taken into account is to have behaviour dependent on the local ply structure. Figure 7.2 illustrates an example: the average COD across a representative 0˚ ply split is shown for a specific position (interval) along the crack length. As is clearly visible, the COD plot exhibits smaller values near the interfaces (right and left hand side of the graph), due to the effect of the ply constrain, while shows higher and more uniform values across the interior of the 0˚ plies. The peak in the middle of the COD line plot (Figure 7.2) is probably related to the presence of echelon cracks. Therefore, due to the aforementioned reasons, the 0˚ ply split width was divided into five intervals to achieve representative average values of COD, but the line plots of COD used are not referred to the intervals close to the interfaces and to the interval in the middle of the 0˚ plies, which might be have influence of the presence of more extensive resin rich regions.

7.2 Influence of the ply structure

Section 7.1 provided some considerations that were applied to different loading cases to facilitate reasonable comparisons of crack opening behaviour, at least in terms of overall crack behaviour. However, it was essentially assumed the 0˚ plies were symmetric, due to the fact the layup is symmetric. This is valid in first approximation, but not strictly true because the local ply structure plays a role in the initiation and propagation of the damage.

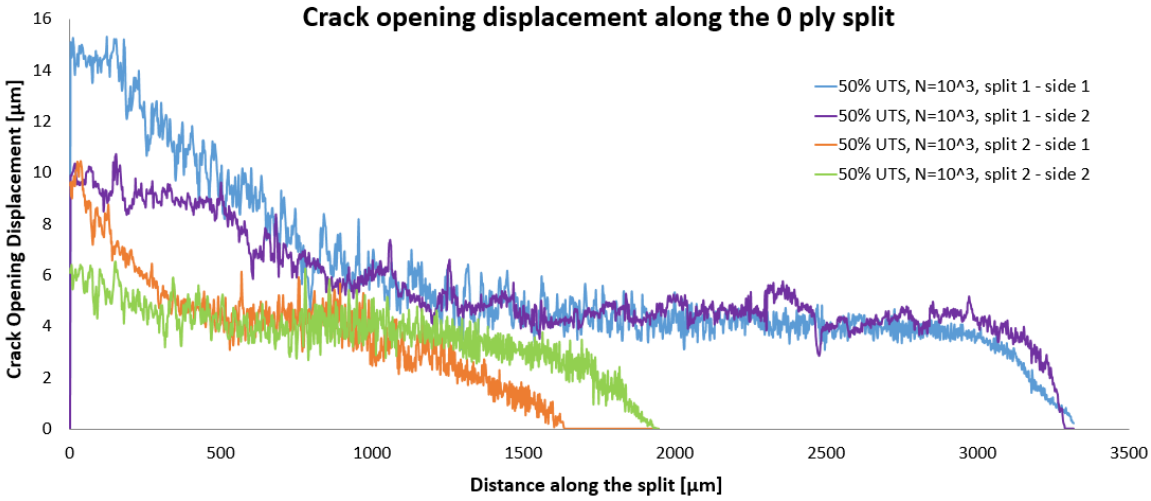

Figure 7. 3 – Crack opening displacement along the 0˚ ply splits detected in the same coupon. Peak load applied 50% UTS and 10^3 cycles.

To assess the influence of the local ply structure on the measured COD line plots, the trend associated with the symmetric regions (interval 2 and 4 in Figure 7.1) for the 0˚ ply splits at 50% UTS and 10^3 cycles were evaluated, Figure 7.3. Both 0˚ ply splits reported in Figure 7.3 are in the same coupon: the '*side 1*' is referred to the interval 2 of Figure 7.1; while the *'side 2'* to the interval 4. The COD line plots detected for each of the 0˚ ply splits show similar behaviour along the crack length, and overall they also exhibit quite similar average COD values, except at the root of the splits (distance ~0) where a distinct difference between the two sides is visible (order of ~4 µm in this case). Therefore, the use of the average COD line plots associated with the intervals 2 or 4 in the schematic presented in Figure 7.1, is a reliable basis to compare different loading conditions. However, the comparison between cracks detected in the same

coupon (Figure 7.3) displays the same maximum difference of ~4 µm at the root between the two sides of the 0˚ ply split, i.e. independent of the associated crack length. In addition, there is a direct correspondence between the higher average values of COD related with the 'side 1' for both cases. One potential cause of different behaviour on the two sides of the 0˚ ply splits is the possibility of damage interaction, such as the presence of delamination at the ply interfaces, and/or the presence of transverse ply cracks. The observation of the two interfaces in this case did not highlight substantial differences. However, it was identifiable that the side characterised by higher average COD at the crack root (side 1 in Figure 7.3) coincides with a reduced local thickness of the coupon due to waterjet cutting, in correspondence of the middle notch region, as shown in Figure 7.4. Even if the thickness of the specimen is relatively small (1 mm) and the difference in thickness between the two external surfaces is minimal, this could be associated with the difference of COD detected.

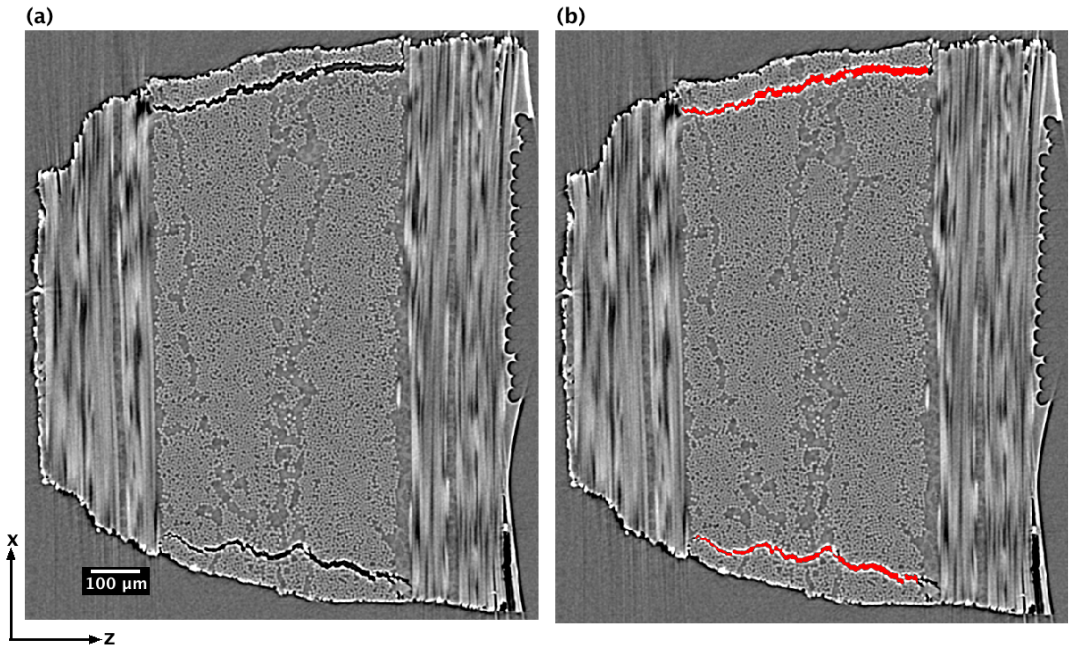

Figure 7. 4 – Cross-sections perpendicular to the loading direction for a peak load of 50%UTS and 10^3 cycles.

This is further confirmed by:

- Different coupons observed have shown a difference of COD between the two sides, consistent with the representation provided in Figure 7.4.
- The difference occurs only at the root of the 0˚ ply splits, where the thickness of the coupon is not perfectly uniform, as shown in Figure 7.3. However, with the increase of the distance from the notch, the COD does not show any substantial difference between the two sides, (*i.e.* see Figure 7.3).

Therefore, the difference in the average COD lines at the root (first ~500 μm) of the crack between the two sides of the 0˚ ply splits detected for a few loading conditions apparently does not seem related with the ply structure or with the presence of other damage modes, but mainly with the non-uniformity of the thickness due to the cutting process. The identified effect when detected can be overcome in two ways:

- Considering the crack opening when the thickness of the coupon is uniform (i.e. beyond 500 μm from the notch/root). In this way, it should be taken into account that the length of the crack is slightly longer than that one considered, even if this does not have substantial influence on the quantification.
- Considering an average value between the two range of values detected on the two sides at the root of the 0˚ ply split.

Overall, the assumption made regarding the symmetric behaviour of the 0˚ ply splits in the present data is substantially justified and does not compromise the interpretation of the results here.

7.3 Effect of the peak load

The loading cases analysed in this section have the same number of cycles (10^3) but different peak loads: 30% UTS, 50% UTS and 70% UTS. The assessment of the influence of the peak load on the crack opening and shear displacement is provided.

7.3.1 Effect of peak load on COD

Higher peak load results in a longer crack and in higher average COD along the entire crack length, from the root to the tip of the 0˚ ply split, as shown in Figure 7.5, where the COD average values for 30% and 50% UTS are represented for a fixed number of cycles of 10^3. When the peak load increases, is expected that the level of stress associated with higher loads can result in a more opening of the 0˚ ply split.

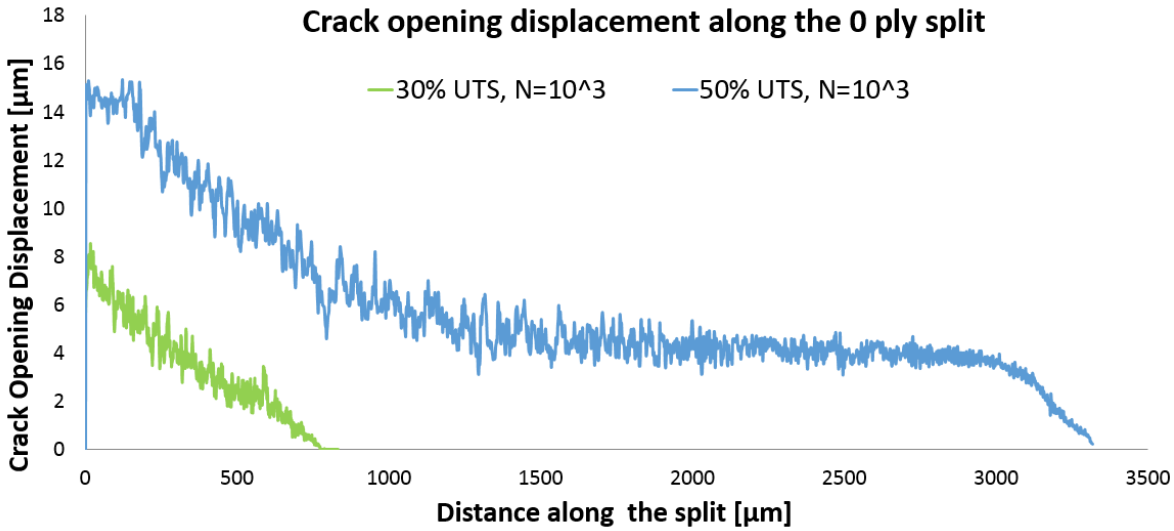

Figure 7. 5 - Crack opening displacement along the 0˚ ply split for the peak load of 30 and 50% UTS at 10^3 cycles.

The overall behaviour of COD from the root of the crack towards the tip for these two loading conditions shows some differences: the low load (30% UTS) is characterised by a monotonic decreasing trend, while the intermediate load (50% UTS) exhibits more complex functionality along its length. The reason may of course be associated with the crack length, directly dependent from the load level, where short crack are dominated by the notch stress field (as the case of 30% UTS and 10^3 cycles) while the longer crack (50% UTS and 10^3 cycles) shows a steady state growth, with the average COD line plot characterised by three main regions:

- The first region corresponds with the root of the 0˚ ply split (from 0 to ~1200 µm), which lies within the notch stress field, and as already described, has the same trend of the low load, even if characterised by higher values.

- The second region represents the majority of the crack length (from ~1200 µm to ~3000 µm) and is defined by a constant average COD value (in the order of 5 µm). This behaviour is typical in the case of steady-state growth, where the COD does not vary with the length of the crack due to constraint of the ply thickness (~500 µm) [1,2].
- The third region is the region immediately behind the crack tip (from ~3000 to ~3300 µm). The gradient of the COD line approaching the tip is similar to that one of the lower load, comparing the same distance back from the crack tip in the two cases.

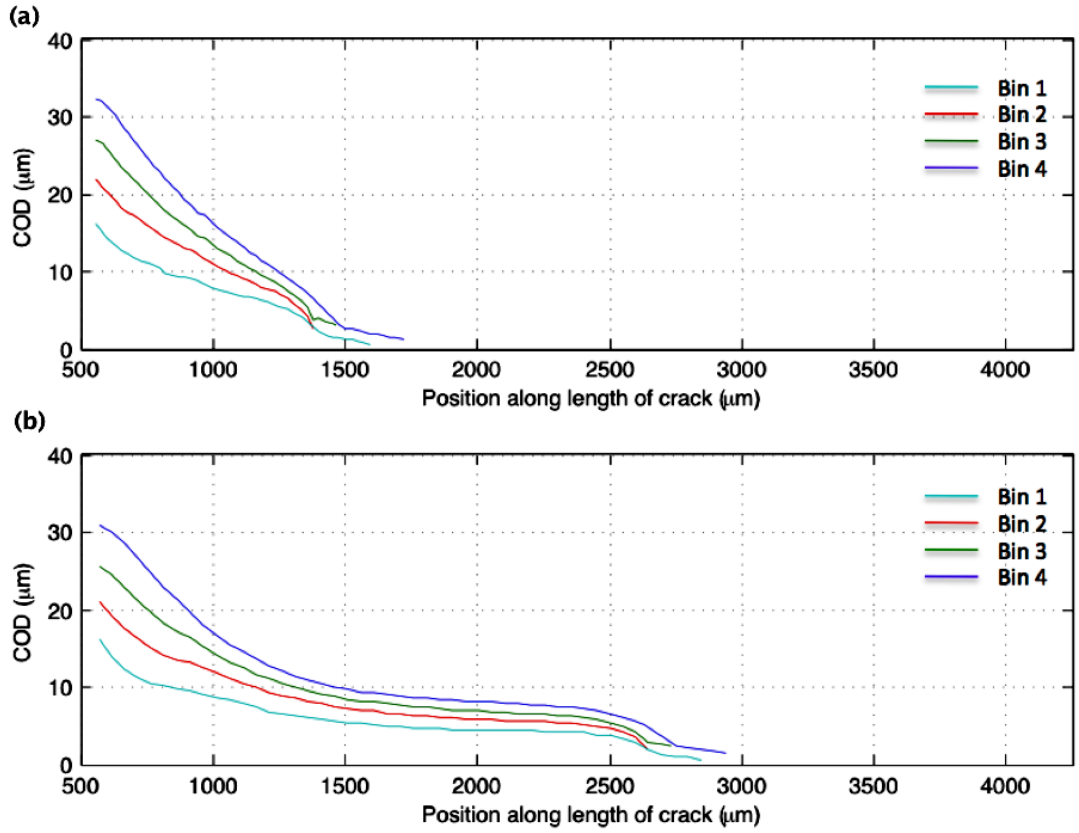

Figure 7. 6 – Crack opening displacement along the 0˚ ply split for a quasi-static load with a peak of: (a) 65% UTS, (b) 80% UTS [1].

A direct comparison with the results obtained by Wright [1] for a model of an incremental quasi-static load, Figure 7.6, has shown good agreement with the trend reported in Figure 7.5 for the fatigue case. Figure 7.6 shows previous results achieved for 65% and 80% UTS static load, where due to the symmetry of the crack, half of the

0˚ ply split (respect to the ply thickness) has been taken into account [1]. Therefore, the average COD lines represented in Figure 7.6 are referred to the intervals starting from the ply interface (bin 1) and moving through the middle of the ply (bin 4). Further details of the model [1] are provided in the Appendix C.

The short crack associated with the 65% UTS shows similar behaviour of the fatigue case in Figure 7.5 associated with 30% UTS and 10^3 cycles (i.e. monotonic decrease in COD approaching the tip), while the longer crack at 80% UTS exhibits the same steady-state region detected for the fatigue case at a similar crack length to 50% UTS with 10^3 cycle fatigue data.

A further increase of peak load (70% UTS) with the same number of cycles may in the first instance be expected to exhibit similar behaviour to that shown in Figure 7.5 for the intermediate load (50% UTS). However, results showed an apparently different trend, as shown in Figure 7.7, particularly at the root of the split. The overall behaviour along the 0˚ ply split decreases from the root towards the tip of the split, but the high peak load evidences a more uniform average COD along the crack length (on the order of 4-6 µm).

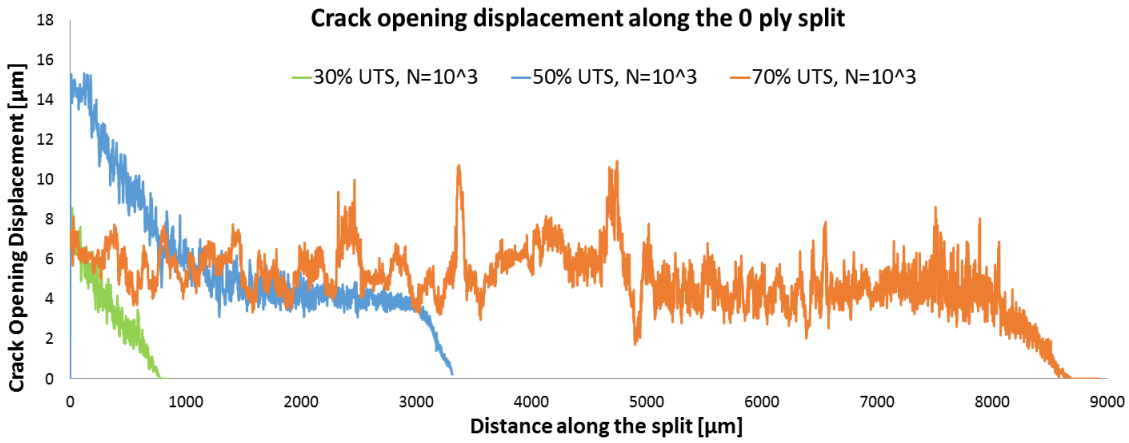

Figure 7. 7 – Crack opening displacement along the 0˚ ply split for the peak load of 30-50-70% UTS at 10^3 cycles.

This behaviour is consistent with the steady state crack growth also detected for the peak load of 50% UTS, but the COD measured at the root of the crack is lower for 70% UTS case than at 50% UTS, whilst the average COD values detected in the intermediate region of the crack (plateau value) are similar to the 50% UTS case. In the first instance,

the COD values shown in the region back from the crack tip for these two different load cases (50% and 70% UTS) may be primarily associated with ply level residual stresses.

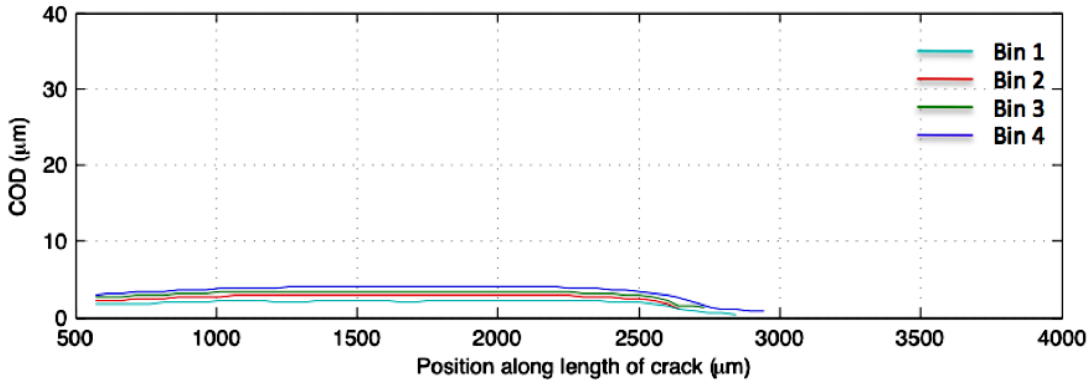

Figure 7. 8 – COD plot of the thermal contribution for a quasi-static case with 80% UTS load [1].

Previous results obtained by Wright [1] for a quasi-static model showed that for a crack length of ~3 mm the thermal contribution to opening is uniform along the 0˚ ply split and increases slightly through the ply thickness (from Bin 1 to Bin 4), Figure 7.8. The influence of the thermal effect (Figure 7.8) on the combined value of the COD, provided in Figure 7.6(b), shows a significant contribution of the residual stress, especially in the plateau region [1]. Considering the intermediate position in Figure 7.8 (bin 2), as it has been done for the fatigue cases, the contribution due to the residual stress in the plateau region is ~3 µm over a total COD of ~5 µm, Figure 7.6(b), which represents the 60% of the average value measured [1]. Whether the fatigue cases shown in Figure 7.7, exhibit a consistent behaviour with the quasi-static case, the contribution of residual stress in terms of percentage respect to the total COD at 50% UTS could be higher than the 70% UTS case. This could be a likely reason that defines a similar COD in the intermediate region of the crack length (plateau) between intermediate (50% UTS) and high (70% UTS) peak load for a fixed number of cycles. The different COD behaviour detected at the root of the 0˚ ply split for the 70% UTS, which shows lower values than the case of 50% UTS, may be also attributed to changes in constraint at the high stress level, where there is simultaneously the presence of extensive delamination at the interfaces and 0˚ ply splits that decouple the plies (90

and 0) with consequently relaxing of the residual stress. In addition, the stress concentration at the notch decreases with the increase of the split crack length [3]; removing the influence of the notch stress/strain field and providing a more uniform stress in the 0˚ plies.

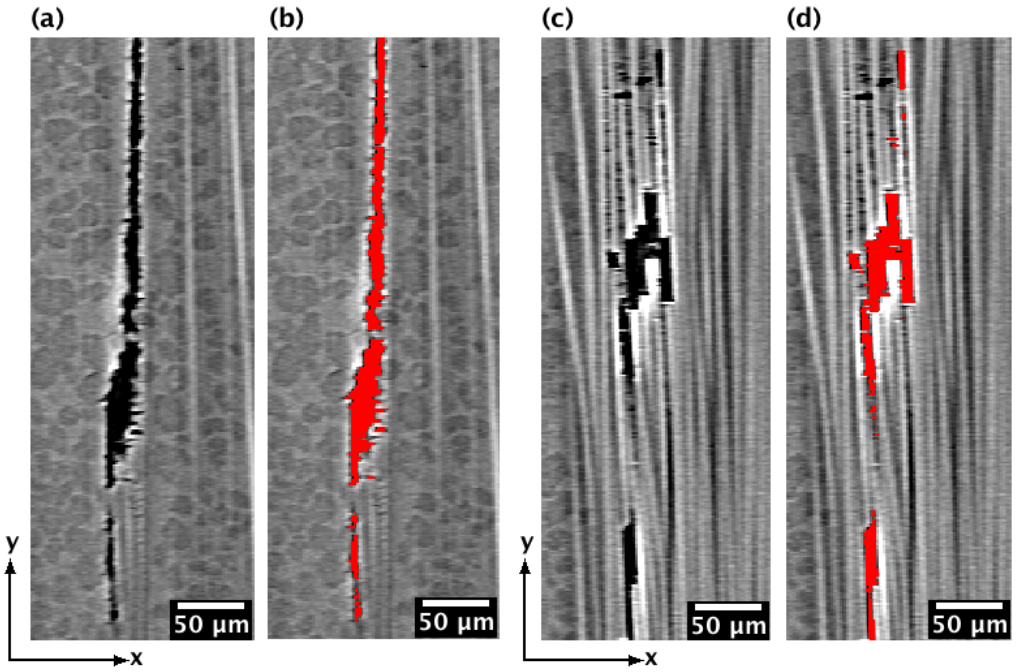

Figure 7. 9 – Cross-sections parallel to the loading direction for 70% UTS and 10^3 cycles. Local effects on the COD of (a) echelons propagation, (c) multiple fibre breaks along the 0˚ ply split, and respectively segmentation (b, d).

The local peak of high COD values, observed in Figure 7.7 for the load of 70% UTS at 2.5 mm, 3.4 mm and 4.8 mm along the crack length are correlated with the presence of echelons that appear connected with the main crack, Figure 7.9 (a) and 7.9(b), and with the presence of multiple fibre breaks along the 0˚ ply split, Figure 7.9(c) and 7.9(d).

7.3.2 Effect of peak load on CSD

The crack shear displacement (CSD) was estimated for the fatigue cases of 50% and 70% UTS at 10^3 cycles, following the methodology reported in the Chapter 3, Section 3.6.4. The values obtained are shown in Figure 7.10, where the point values correspond with the experimental results, while the line is a linear fitting. Due to the reliance of the

current method on fibre breaks detected along the 0˚ ply split, the case of 30% UTS and 10^3 cycles was not reported in Figure 7.10 because the number of fibre breaks observed along the 0˚ ply split was relatively low. However, single experimental observations of the CSD related to 30% UTS and 10^3 cycles are located below the plot obtained for 50% UTS and 10^3 cycles, consistent with the trend in Figure 7.10.

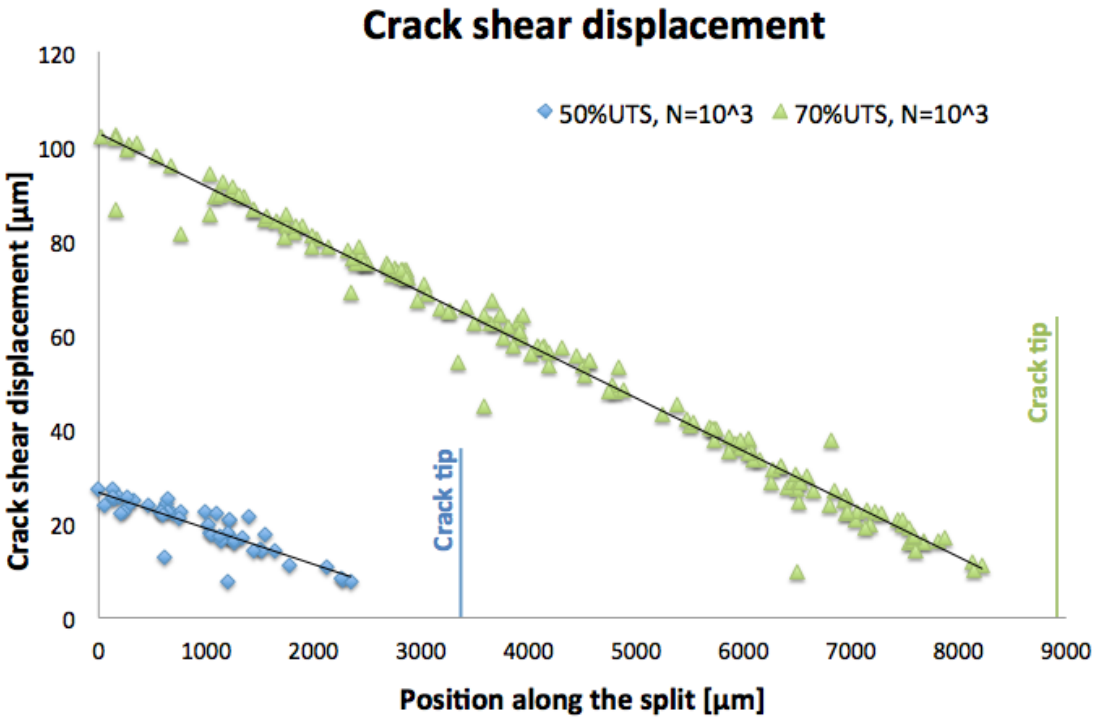

Figure 7. 10 – Crack shear displacement along the 0˚ ply split for 50 and 70% UTS at 10^3 cycles.

The shear displacements decrease linearly from the root towards the tip of the split for both loading conditions, Figure 7.10. The CSDs can only be obtained to within ~0.5 mm of the crack tip, as they are dependent on the presence of fibre breaks along the 0 ply split, which are not present in the region immediately behind the crack tip (as described in Chapter 6). This explains the absence of experimental CSDs data in Figure 7.10 in the region behind the crack tip. The linear trendlines in CSD, Figure 7.10, are consistent with the models provided by Wright for the quasi-static case [1], see Figure 7.11. Further details of the quasi-static model [1] used in this comparison are provided in the Appendix C. The comparison of the CSD for the two fatigue cases in Figure 7.10 reveals that CSD for the 70% UTS is ~three times higher than that measured at 50% UTS, consistent with both considerably longer crack length and load in the former case.

The fatigue results agreed with the increase of CSD also found for the quasi-static model when an incremental load is applied [1], which also corresponds with an increase of crack length and also of CSD, Figure 7.11.

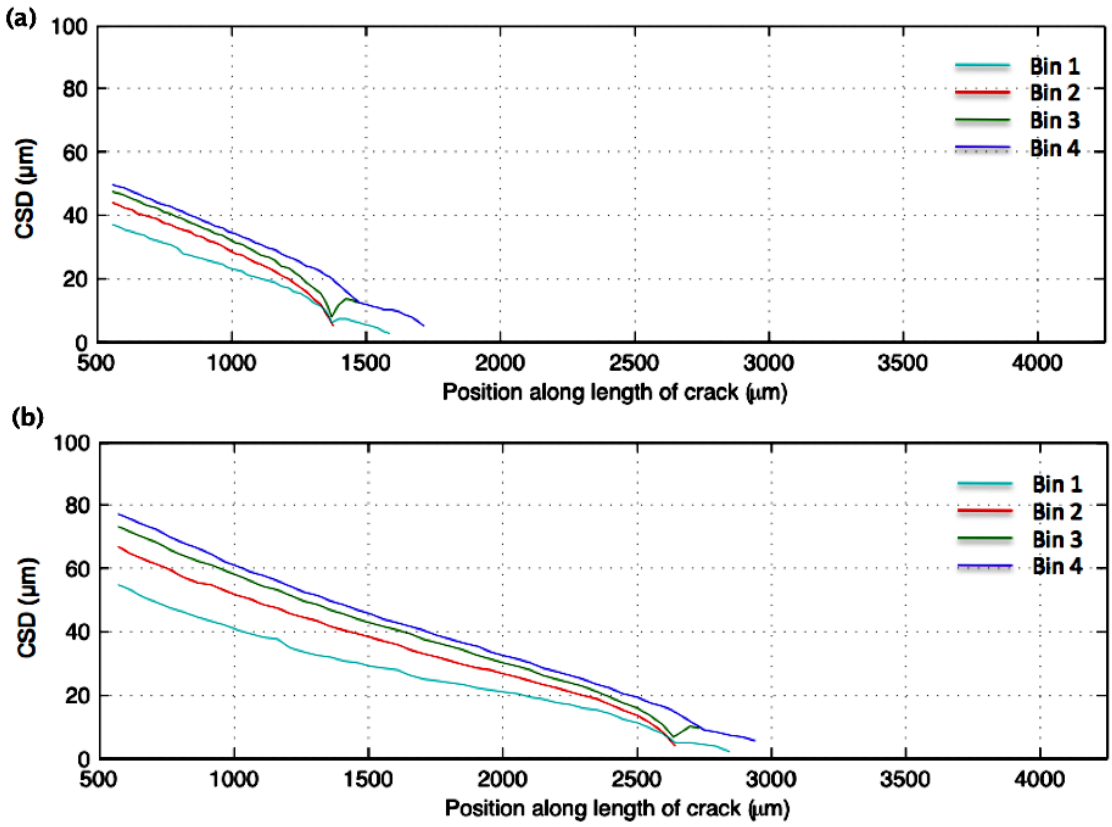

Figure 7. 11 - Crack shear displacement along the 0˚ ply split for a quasi-static load with a peak of: (a) 65% UTS, (b) 80% UTS [1].

7.4 Effect of the number of cycles

The effect of the number of load cycles has been assessed using two cases with the same peak load (50% UTS) and different cycling increments: 10^3 and 10^5. Results were reported in terms of crack opening and crack shear displacements, shown in Figure 7.12 and Figure 7.14. The increase in number of cycles does not create a more open crack, Figure 7.12, and the average COD values between the two cycling increments overlap. The higher number of cycles involves an increase of crack length, with the

COD line plot following the plateau at ~4 µm, also characteristic at 10^3 cycles, consistent with steady state crack behaviour and residual stress effects.

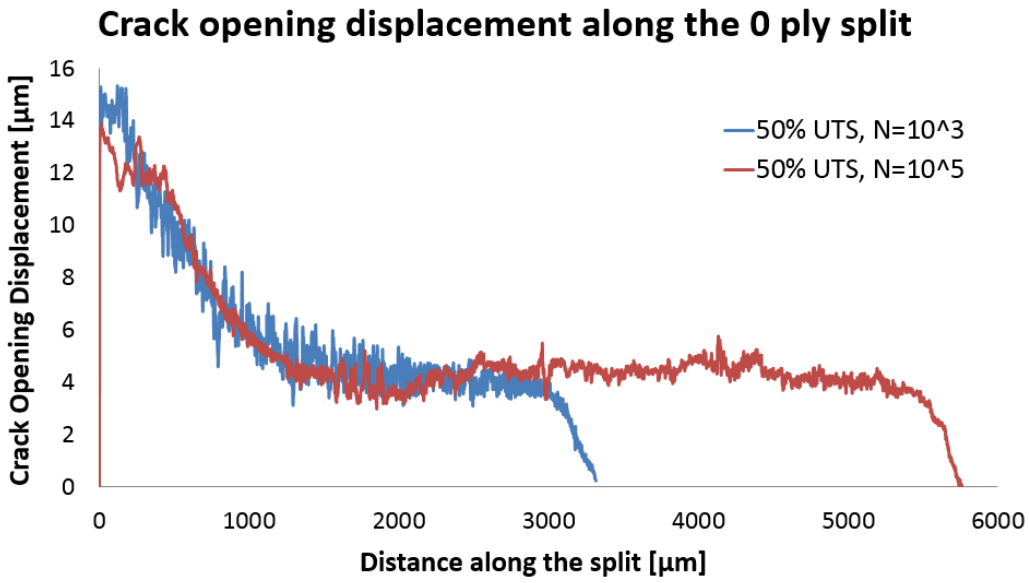

Figure 7. 12 - Crack opening displacement along the 0˚ ply split for the peak load of 50% UTS at 10^3 and 10^5 cycles.

The behaviour in the region close to the crack tip (within ~300 µm) appears to be very similar for both cycling conditions, with the slope decreasing COD being comparable. As such steady-state conditions for near-tip crack tractions/bridging is also inferred, consistent with crack wake fibre break behaviour reported in Chapter 6. Consideration of bridging ligament effects on near-tip COD needs assessment (quantification of bridging ligaments) to confirm. However, recent cohesive zone modelling results published by Yang and co-workers [4] showed how the presence of near-tip tractions can generate a distinctly narrow/sharp crack tip opening for similar 0˚ ply split loading, see Figure 7.13. Experimental data (SRCT) is also shown in Figure 7.13, where a degree of crack wake bridging is known to occur. The crack tip location is at ~2.7 mm [4].

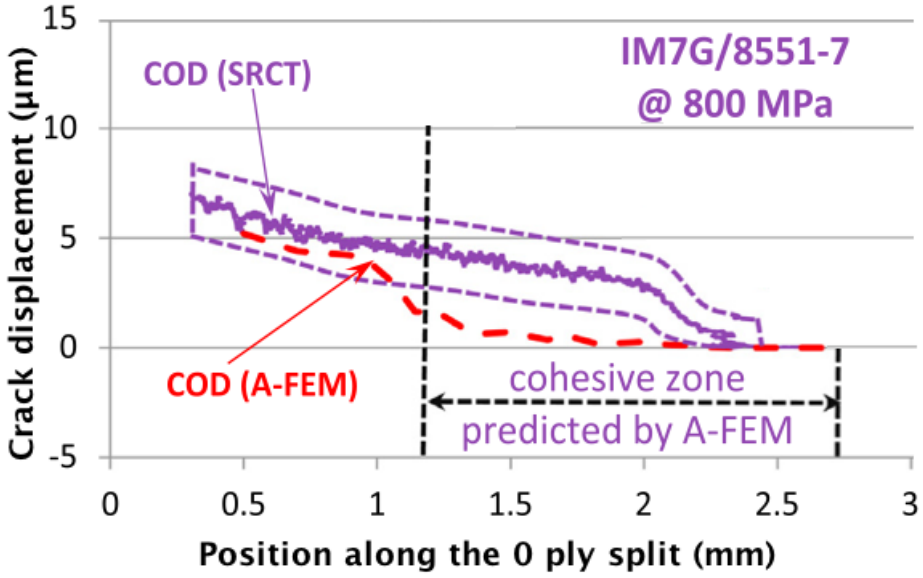

Figure 7. 13 – Crack opening displacement plot of a quasi-static 0˚ ply split in cross-ply CFRP (8551-7/IM7) obtained by augmented-finite element model by Yang et al. [4].

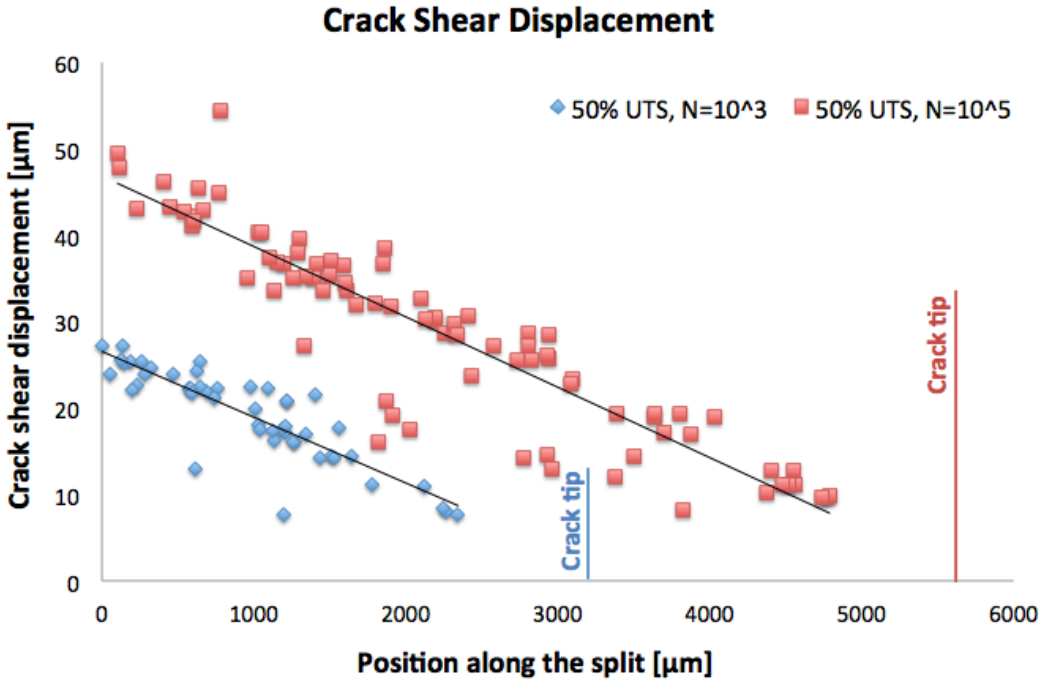

Figure 7. 14 – Crack shear displacement along the 0˚ ply split for the peak load of 50% UTS at 10^3 and 10^5 cycles.

The crack shear displacement between the fatigue cases at 50% UTS with 10^3 and 10^5 cycles has been evaluated and shown in Figure 7.14. The trendlines confirm a linear decreasing from the root towards the crack tip, as also found for the comparison of different peak loads represented in Figure 7.10. In addition, the correlation between the crack length and the CSD values in Figure 7.14, where a doubling of the crack length is roughly characterised by doubling the CSD, is consistent with the CSD plot in Figure 7.10. The ideal extension of the trendlines displays CSD values of zero at the crack tip and ahead of the crack tip; still consistent with the results found by the quasi-static model [1], see Figure 7.11.

7.5 Influence of damage modes interaction

This section has the aim to investigate the influence of other damage modes, such as the presence of delamination and transverse ply cracks, on the crack opening displacement values. The effect of delamination on the COD has been discussed in Chapter 4 (Section 4.5), where it was concluded that delamination did not affect the COD for the cases considered, because the delamination area was limited to a small percentage of the 0˚ ply split length, and did not connect 0˚ ply splits on the opposite sides of the notch. However, different loading conditions could exhibit a different behaviour. The objective of this section is to identify potential implications of delamination and/or transverse ply cracks on the current COD measurements.

The presence of transverse ply cracks could influence the crack opening. Particularly, when transverse ply crack is fully open, may have an effect on the 0˚ plies, which result being locally less constrained, with potentially local effect on the COD. This was observed in correspondence of the notch region when severe loading conditions were applied, such as 50% UTS with 10^5 cycles, and 70% UTS with 10^3 cycles. However, it should be notice that the effect of the transverse ply cracks is localised to the notch region and for a length equals to the transverse ply crack opening. Consequently, the influence of the transverse ply cracks, when detected as fully open, is only limited to a small region along the 0˚ ply crack (depending on the transverse ply crack opening).

However, when average values of the crack opening displacement are provided, the influence of the transverse ply cracks on these is found to be negligible.

The delamination appears quite early in the process of 'damage progression' under fatigue loading and, even along only one interface, could lead to the decohesion on one face of the 0˚ plies, relaxing the constraint on that side of the crack. The influence of delamination on the COD is accentuated when both interfaces show delamination at the same length along the 0˚ ply splits. This could cause the connection between the two opposite splits and the 'separation' of the 90˚ plies, as shown in the cross-section in Figure 6.14.

In this study three different situations have been investigated to evaluate the effect of delamination on COD:

1. A sequence of cycling, such as the case reported in Figure 7.12, could provide a reliable comparison. For a fixed peak load (50% UTS in this case), the increase in the number of cycles (10^3 vs. 10^5) results in an increase of delamination area. In particular, the low number of cycles showed a very small area of delamination, only at one interface, while the higher number of cycles shows delamination on both interfaces. Whether delamination affects the total COD, the average values of the case at the higher number of cycles (highly delaminated) should be characterised by different COD values. However, Figure 7.12 shows similar average COD for the two cases considered. This is consistent with the fact that in this context (steady-state crack growth) the residual stress play an important role in determining the total COD, and the presence of delamination associated with the higher number of cycles does not influence this behaviour.
2. Based on the consideration that the delamination could influence the crack opening, two intervals along the 0˚ ply split have been considered in terms of COD: (i) with delamination on both interfaces; (ii) without delamination. Referring to Figure 7.12, the case of 50% UTS with 10^5 cycles, the interval characterised by delamination is located along the crack length from ~1.5 mm to 2.5 mm, while the region with no delamination is represented by 2.5 mm onwards along the split. The COD line plot in Figure 7.12 does not show a change in COD behavior for these two intervals along the split, consistent with

the role of residual stress on the COD, regardless the presence of local delamination at the interfaces.

3. The most severe condition considered is represented from the 70% UTS peak load with 10^3 cycles, which is characterized by extensive delamination area on both interfaces, along almost all the 0˚ ply splits length. This condition, associated with decoupling of plies due to the simultaneous presence of delamination and 0˚ ply splits, starting from the notch up to all the splits length, may have some influence on the COD determination. As mentioned in the Section 7.3.1, the presence of high-delaminated area at the interfaces can release residual stress, leading to a 'flat' COD plot starting from the root of the split, as shown in Figure 7.7. In addition, the change in near-root opening at 70% UTS could be also due to loss of stress concentration with the significantly increase of the crack length. In this case the presence of delamination affects the average value of COD, even if it is difficult to understand clearly in which way.

Based on the present results, establishing whether other damage modes, particularly delamination, may or may not affect the final COD is not trivial, and it is not strictly dependent with the presence/absence of the damage mode, but other factors could be simultaneously have implication, such as the role covered by the residual stress, and the stress concentration associated with the crack length.

7.6 Effect of high number of cycles

High numbers of cycles up to 10^6 were performed applying a relatively low peak load of 30% UTS. Some of the results related with this loading condition were already presented in this chapter. This section has the objective of investigating the effect of the high number of cycles on damage propagation, highlighting the differences observed when compared with a lower number of cycles. The two 0˚ ply splits detected have a length on the order of 2 and 3 mm. Therefore, even if the number of cycles is relatively high, the low peak load causes relatively small cracks. The three-

dimensional segmentation show that the morphology of the split (Figure 7.15) for half of the crack length exhibits clear differences with respect to the typical 3D crack shape obtained for the same material system, *i.e.* the case of 50% UTS and 800 cycles, as shown in Figure 5.12(a). The crack front profile in Figure 7.15 (right hand side) appears more uniform across the 0˚ ply split width, and tunnelling of the tip producing no damage in the resin rich regions for a length in the order of 100 µm back to the tip, versus the much more '*jagged*' shape detected for the other fatigue cases (*i.e.* Figure 5.12(a) or Figure 4.9(b) with a similar crack length).

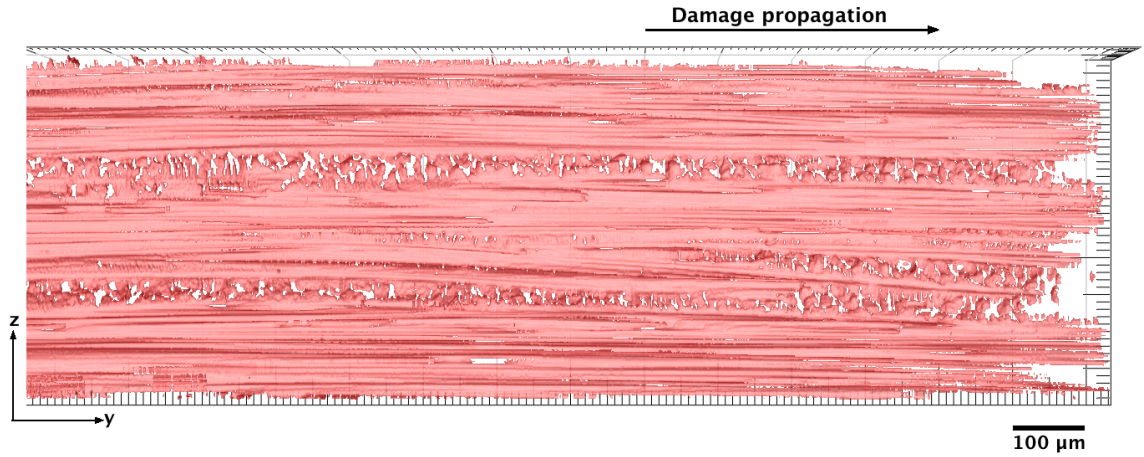

Figure 7. 15 – 3D rendering of the 0˚ ply split tip for 30% UTS and 10^6 cycles. The crack length shown corresponds to half of the total length, and the split tip is at the right hand side.

The crack front profiles for these aforementioned cases (30% UTS with 10^6 cycles, and 50% UTS at 800 cycles) are illustrated in Figure 7.16, where it is clear that the 0˚ ply split for high number of cycles is characterised by a more 'flat' front profile (Figure 7.16(a)), with a value of crack front variation (measured as root mean square, RMS) significantly lower than the case of 50% UTS with 800 cycles (Figure 7.16(b) associated with the 0˚ ply split in Figure 5.12(a)). To assess whether this difference in crack morphology is connected to the high number of cycles or to the low peak load, the crack profile of the 0˚ ply split obtained for 30% UTS and 10^3 has been also evaluated. Results showed a jagged crack front profile for the case of 30% UTS and 10^3 cycles. Therefore, the more uniform crack front profile is consistent with the high cycle numbers rather than with the low peak load.

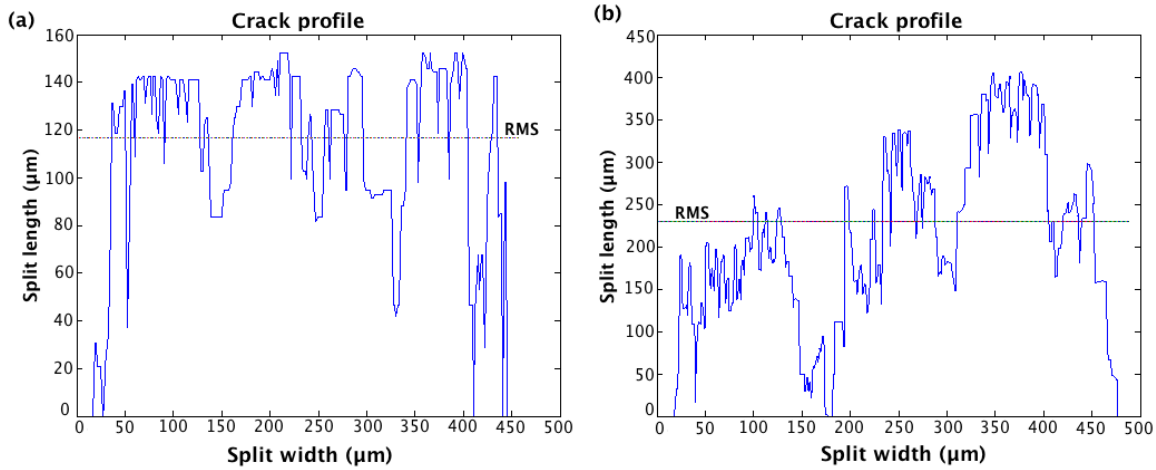

Figure 7. 16 – Crack front profile with an estimation of the variation, provides as root mean square, for: (a) 30% UTS and 10^6 cycles, (b) 50% UTS and 800 cycles.

When the aforementioned transition between a non-uniform to a more uniform crack growth occurs and whether higher peak loads behave similarly at a certain point of the cycling process is unknown at this stage. This could be particularly interesting to assess in future work, because it may provide further information on the role of toughening system and specifically of toughening particles at high number of cycles. It is interesting to note that the bridging ligaments extend for a much longer distance back from the crack tip (~2.2 mm over a total crack length of 2.7 mm) for the case of 30% UTS and 10^6 cycles compared to the other fatigue loading conditions.

7.7 Conclusions

Synchrotron radiation computed tomography experimental data has been employed to quantify crack opening and crack shear displacements for different loading conditions, varying the peak load and the number of cycles. The influence of peak load, number of cycles, cracks length, damage interaction modes, on the crack opening and crack shear displacement has been assessed. Results obtained were compared with previous numerical study conducted on the same material system for static loading/cracking. The comparison has shown similar behaviour in term of overall COD trends, depending on the crack length considered. Specifically, CODs at short crack lengths are consistent

with stress concentration around the notch field, showing a monotonic decrease of the average COD from the root of 0˚ ply splits towards to the tip fatigue cases; consistent with the observations in the literature for a quasi-static load. Longer crack are characterised by steady-state opening, with a plateau value of COD for the majority of split. Therefore, the crack length does not affect the COD values in the steady-state growth. The COD behaviour detected at the root of the 0˚ ply split for the fatigue case of 70% UTS showed smaller average values than the other fatigue cases with lower peak loads. The reason may be related with the presence of extensive delamination area at the interfaces (with consequently decouple of 90˚ and 0˚ plies) that could relax residual stress, and with the decrease of the stress concentration associated with a longer crack. Both effects may be have substantial influence on the notch stress/strain field and consequently on the COD values. The crack shear displacement (CSD) assessed along the 0˚ ply split, has shown a linear decreasing trend from the root towards to the tip of the crack. The absence of fibre breaks in the region immediately behind the split tip did not allow estimating the CSD for all the crack length. However, the ideal extension of the linear fitting of the experimental values of CSD has shown a null value in correspondence of the crack tip and ahead of this. Results obtained represent an insight to the physical micromechanisms associated with the fatigue loading, and may provide valuable information for modelling.

7.8 References

[1] P. M. Wright, "Investigation of damage in laminated carbon fibre composites using high resolution computed tomography," University of Southampton, Ph.D Thesis 2011.

[2] V.C. Li E. Yang, "Numerical study on steady-state cracking of composites," *Composites Science and Technology*, vol. 67, pp. 151-156, 2007.

[3] S.M. Spearing and P.W.R. Beaumont, "Fatigue damage mechanics of composite materials. Part III: prediction of post-fatigue strength," *Composites Science and Technology*, vol. 44, pp. 299-307, 1992.

[4] Q.D. Yang et al., "On crack initiation in notched, cross-plied polymer matrix composites," *Journal of Mechanics and Physics of Solids*, vol. 78, pp. 314-332, 2015.

[5] P. Wright, A. Moffat, I. Sinclair, and S.M. Spearing, "High resolution tomographic imaging and modelling of notch tip damage in a laminate composite," *Composites Science and Technology*, vol. 70, pp. 1444-1452, 2010.

Appendix C

This section provides details on the numerical model developed by Wright [1,5] for a quasi-static case and used in this chapter to compare the COD and CSD behaviour obtained in fatigue. The material system used was a particle-toughened carbon epoxy (M21/T700) with a cross-ply layup and double-notch geometry. Details of the geometry are shown in Figure C.1. *In situ* synchrotron radiation experiments were conducted applying an incremental tensile load, and the damage growth was monitored for different load steps (from 30% UTS to 90% UTS). Experimental results obtained by the analysis of SRCT data were used to calibrate and validate a finite element model to predict the crack opening and shear displacement. The model is based on the use of duplicated nodes to include the pre-existing split [5] and on the application of the virtual crack closure technique to determine the strain energy release rate driving the crack growth at the tip of the split [1].

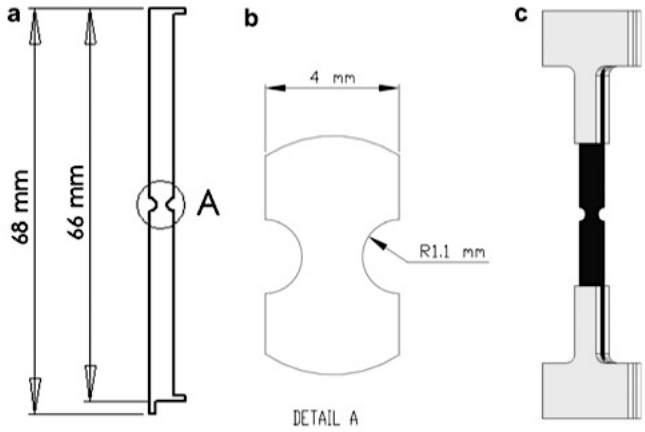

Figure C. 1 –Geometry and dimensions of the coupons used in the *in situ* quasi-static experiments [5].

Results obtained from Wright model [1] and presented in this chapter, Figure 7.6, 7.8 and 7.11, are referred to the model that include the non-uniform crack profile growth due to the variation on the microstructure (called by the author as 'pinned model'). The inflections reported in correspondence of the crack tip for the COD and CSD in Figure 7.6 and 7.11 might be associated with the artificial way to create the tip or with

mesh inefficiency, and are not present in the model that does not take into account the pinning behaviour.

Chapter 8

Conclusions and future work

8.1 Conclusions

Synchrotron Radiation Computed Tomography combined with *in situ* loading has been demonstrated as an effective technique for investigating the micromechanisms of fatigue in composite materials with both toughened and untoughened matrices. Several novel observations have been obtained for the micromechanisms of fatigue crack growth.

- Broadly similar micromechanisms of damage initiation have been identified in fatigue and quasi-static loading in a particle-toughened carbon fibre-epoxy composite system. Cracks nucleate in the matrix/fibre-matrix interface region within volumes of high local fibre-volume fraction within the 0˚ plies. This initial stage is not characterized by the propagation of a single dominant crack, but multiple microcracks separated by bridging ligaments. As such, the micromechanisms of damage initiation are similar to those of damage propagation; both characterised by multiple microcracks disconnected by the presence of bridging ligaments rather than a single dominant crack (tip).
- Novel observations have been obtained for the micromechanisms of fatigue damage growth. Results showed that damage propagation is closely related to the local microstructure. Toughened systems exhibit different damage

behaviour in resin-rich regions and fibre-packed zones, which appear to exaggerate non-uniform crack growth. Zones of retarded crack growth correspond to resin-rich regions, which contain bridging ligaments. This was most pronounced in the particle-toughened system, and less so in the intrinsically toughened system. There is evidence that the load cycling contributes to progressive failure of bridging ligaments in the crack wake, especially in the toughened particle system. The untoughened system showed more uniform damage propagation across the crack front, due to the more uniform microstructure. Consequently, fracture occurs by the propagation of a well-defined crack front, whereas in the toughened systems there is extensive micro cracking ahead of the crack tip and crack bridging processes behind the crack tip. However, the overall crack growth rates are similar between the toughened and untoughened systems.

- It seems likely that in the particle-toughened system the key mechanism of fatigue in intralaminar loading is the degradation of bridging ligaments introduced by particles in the fatigue crack wake; resulting in higher, more uniform crack opening displacements and less-jagged crack fronts compared to the quasi-static loading for similar crack lengths considered. Therefore, the particle-toughening strategy has less impact in fatigue than in quasi-static loading due to the degradation of bridging ligaments associated with the cycling process.
- The current study has shown that fatigue induces fibre breaks along the 0˚ ply split paths and in the bulk composite (within the 0˚ ply and not close to other damage modes). The micromechanism of fibre failure along the 0˚ ply split has been identified as being due to the presence of fibre bridging across the split subjected to fibre/matrix debonding, with the action of axial stress (along the loading direction) due to the shear, and a bending action associated with opening of the crack. This micromechanism confirms also the fact that the fibre break density decreases from the root of the 0˚ ply split towards the tip and no fibre breaks have been detected ahead of the crack tip. However, the nature of fibre failure in the bulk composite is still not well understood.

- Fatigue induces progressive fibre breaks in the bulk composite along the loading direction, not exclusively in the notch region, but in the entire volume delimited by the presence of delamination and 0˚ ply splits, suggesting that the analysis of fibre failure needs to be conducted on a larger volume than the notch region.
- A direct comparison with previous results from quasi-static loading showed that the number of fibre breaks associated with the fatigue cases is consistently higher than the number of fibre breaks detected under quasi-static load.
- Fatigue damage quantification conducted for different loading conditions enabled the evaluation of the influence of peak load, number of cycles, crack length, local microstructure, and damage interaction modes on the crack opening and crack shear displacement. The behaviour detected in terms of crack opening displacement was found to be divided into two regimes, defined by crack length: (i) short cracks (within the notch region), demonstrated displacements affected by the notch stress/strain field, showing a decreasing crack opening displacement trend from the root of the crack towards the tip; (ii) longer cracks exhibited a steady-state growth, characterised by a constant value of crack opening displacement, independent of position, in the region back from the crack tip, and for the majority of the crack length.
- The effect of residual stress on the steady state splits represents a significant contribution to the overall crack opening displacement, resulting in similar opening even for different applied loading conditions.
- The fact that the crack opening displacement increases in the region immediately behind the crack tip for a few hundred micrometers, and then maintains a uniform value defined by the steady-state behaviour, could be significant in defining the limited region where the bridging ligaments may play a role in the process of damage resistance. This is due to the cycling process that tends to link the microcracks along the crack wake, creating a more continuous 0˚ ply split.
- The application of high loads, above 70% UTS, results in extensive delamination and 0˚ ply splits that have substantial influence on the notch stress-strain field, releasing the residual stress, with direct consequences on the crack opening

displacement values. In this context the interaction of different damage modes could make a significant contribution to the crack opening displacement, especially at the root of the crack within the notch region.

- The crack shear displacement showed a linear decreasing trend along the 0˚ ply splits with average values directly connected with the peak load.
- The comparison of results obtained in terms of crack opening and crack shear displacement for the fatigue loading with models in literature for equivalent quasi-static cases indicates a correspondence between the behaviour detected for short cracks (within the notch region) and also for steady-state cracks.

The use of synchrotron radiation computed tomography coupled with *in situ* tests is confirmed being a valuable tool in the study of micromechanisms in composite giving the opportunity to obtain the results presented in this report, impossible to obtain previously by the use of other techniques. The observations and the experimental quantification conducted during this research could represent a potential for exploitation by modellers.

8.2 Future work

The current research highlighted different potential ways for further investigation in terms of experiments, imaging analysis processes, and modelling.

- The focus of this study was on the coupon lengthscale, characterised by specimens on the order of a few millimeters (4 mm width, 1 mm thick and with a notch cross-section of ~1 mm). The use of small coupons is dictated mainly by the use of synchrotron computed tomography, which allows small field of view where high resolutions are required. The “size effect” is a well know phenomenon in composites, and may result in different behaviours where different lengthscale are considered. Performing multiscale assessments on fatigue loading would be an interesting aspect to evaluate similarities and differences with respect to the coupon level behaviour detected in this study.

Due to the trade-off between the voxel resolution and field of view achievable, the main limitation of using synchrotron computed tomography is represented by the need for small specimens, which could represent an additional issue when bigger coupons are considered. On the other hand, the use of a lower voxel resolution with a consequently increase of field of view does not represent the optimum due to the fact that the diameters of carbon fibres are small (~6 µm) in diameter and toughening particles are of a similar size. Based on the results obtained from this research a good compromise could be represented by a voxel resolution slightly higher than 1 µm (i.e. 1.2-1.5 µm), which allows a field of view on the order of 3-3.5mm. Considering a laminate thickness similar to that used for the current study (1mm), the other dimensions of the coupons could be scaled. To overcome the limitations associated with the field of view, a feasible approach could be to perform scans at a lower voxel resolution to obtain the overall information on the damage extension, and at the same time use localised multiple scans to investigate the micromechanisms of damage initiation and propagation. The size effect analysis could assess various aspects; such as the micromechanisms of damage propagation to compare with the non-uniform crack profile detected in the small coupons, the role of toughening particles and toughening bridging behaviour, the fibre failure investigation, the correlation between the crack lengths, crack opening and crack shear displacement with the geometry and so forth. In other words, the multiscale study could provide important information whether a small coupon could be representative even of a higher length scale, and how the information obtained on small scale could be used on a bigger scale.

- Fibre failure detected under fatigue loading is one interesting aspect that deserves further study to have a better understanding of the micromechanisms associated with fibre breaks in the bulk composite. The results obtained in this work have shown a significant number of fragmented fibres in the bulk composite for the high peak load considered (70% UTS). The use of this level of load with *in situ* fatigue tests could represent the optimum to evaluate the micromechanisms of fibre failure in the bulk composite considering multiple

steps of incremental cycles. This study could also provide information on cluster formation in fatigue, assessing the presence of the subsequent growth of fibre breaks in the same place or whether cluster formation is a more stochastic process, as also suggested from a previous study conducted for quasi-static loading.

- The use of ultrafast tomography coupled with *in situ* fatigue tests could give fundamental information at the stage final stage of fatigue life, evaluating whether failure is associated with a dominant mechanisms (i.e. cluster formation as in the case of tensile loading or due mainly to delamination) or multiple damage modes interacting simultaneously to determine the final failure.
- Assessing fibre failure for different loading conditions (peak loads and number of cycles) for the untoughened and intrinsically toughened systems, as was performed in Chapter 6 for the particle-toughened system. The comparison with the results obtained for the fatigue cases in the toughened-particle system could add important information in relation to the material properties (*i.e.* fibre/matrix adhesion).
- The role of bridging ligaments and their effectiveness under fatigue loading seems limited to the region immediately back from the crack tip of the 0˚ ply split. However, the quantification of bridging ligaments for different load levels and number of cycles is further required to confirm this.
- The aim of composite toughened systems, as the case of the particle-toughened and the intrinsically toughened system, is to increase the damage resistance with respect to an equivalent untoughened system. It could be interesting to evaluate the behaviour of the particle-toughened system whether subjected to low temperature, such as -40/-50 ˚C, which are typically representative of the operative conditions for aerospace applications, with the aim to assess the role of thermoplastic particles at lower temperature.
- The quantification of damage in the form of crack opening and crack shear displacements, and potentially strain fields, provides an insight as to the physical micromechanisms associated with the fatigue loading, and can provide valuable information for modelling. Therefore, the experimental data obtained

in this research could be used to calibrate and validate numerical models. The use of a model can add fundamental information that is not possible to achieve by the use of experimental data exclusively, such as the role of the residual stress on the crack opening, the influence of damage mode interaction at high peak load, the tendency of cluster formation due to fatigue loading, the apparent behaviour to accommodate more fibre breaks in fatigue than in quasi-static case before final failure, and the effect that fibre failure may have on strength reduction.

- Imaging processing generally required a long time due to the fact that the methodologies used are not automatized. However, the creation of automatic processes for crack segmentation is not trivial, especially when multiple volumes are concatenated each other or when the crack itself is characterised by a range of greyscale values. Future work could focus on potential solutions to decrease the time for segmentation by the optimization/standardization of an automatic process. This would make it possible to process more volumes in a shorter time, and consequently investigate wider spectra of conditions.